Devices for Biological Systems: On-Chip Horizontal Gene Transfer and 3D-Printed Microfluidic Applications

BY

MARTIN D. BRENNAN
B.S., University of Illinois at Chicago, 2011

THESIS

Submitted as partial fulfillment of the requirements
for the degree of Doctor of Philosophy in Bioengineering
in the Graduate College of the
University of Illinois at Chicago, 2017

Chicago, Illinois

Defense Committee:

Dr. David T. Eddington, Chair and Adviser
Dr. Salman Khetani, Dept. of Bioengineering
Dr. Donald A. Morrison, Dept. Biological Sciences
Dr. Vivek Sharma, Dept. Chemical Engineering
Dr. Jie Xu, Dept. Mechanical & Industrial Engineering

I dedicate my dissertation work to my family, especially my parents Tim and Cindy, for being my first teachers who taught me to believe in hard work. Their endless love and encouragement are the greatest gift I've ever had.

I also dedicate this dissertation to my wife Wangfei, who has been there with me the whole time.

Acknowledgements

Contribution of Authors

Chapter 1 includes a previously published review article (Martin D Brennan, Megan L Rexius-Hall, Laura Jane Elgass, and David T Ed- dington. Oxygen control with microfluidics. Lab Chip, 14(22):4305–4318, 2014. ISSN 1473-0197.) of which I was the first author and final editor. My Co-workers Megan Rexius-Hall, and Laura Jane Elgass also contributed to the writing of introductory sections and the literature review. Dr. David Eddington played and advisory role.

Chapters 1-4 contain sections from my previously published research article (Martin D Brennan, Megan L Rexius-Hall, and David T Eddington. A 3D-Printed Oxygen Control Insert for a 24-Well Plate. Plos One, 10(9):e0137631, 2015. ISSN 1932-6203.) of which I was the first author and major driver of the work. Megan Rexius-Hall aided in cell experiments and generated figure 3. Dr. David Eddington played and advisory role.

Chapters 1-4 also contain sections from my previously published research article (Martin Brennan, Fahad Bokhari, and David Eddington. Open Design 3D-Printable Adjustable Micropipette that meets ISO Standard for Accuracy. bioRxiv, 2017.) of which I was the first author and major driver of the work. Fahad Bokhari, the second author, aided in CAD modeling and data collection for this work. Dr. David Eddington played and advisory role.

Contents

List of Figures

List of Tables

Abbreviations

ABS	**A**crylonitrile-**B**utadiene-**S**tyrene
ATP	**A**denosine **Tri**phosphate
B2M	**B**eta-**2**-**m**icroglobulin
BSA	**B**ovine **S**erum **A**lbumin
CAD	**C**omputer-**A**ided **D**esign
CAT	**Ca**sein **T**ryptone Medium
CDM	**C**hemically **D**efined **M**edium
CFU	**C**olony **F**orming **U**nits
CSP	**C**ompetence-**s**timulating **P**eptide
dsDNA	**D**ouble **S**trand **DNA**
ECM	**E**xtra**c**ellular **M**atrix
FDM	**F**used **D**eposition **M**odeling
FLIM	**F**luorescence **L**ifetime **I**maging **M**icroscopy
FTIR	**F**ourier **T**ransform **I**nfrared **S**pectroscopy
GFP	**G**reen **F**luorescent **P**rotein
HbS	**S**ickle-cell **H**emoglo**b**in
HGT	**H**orizontal **G**ene **T**ransfer
HIF	**H**ypoxia **I**nducible **F**actor
HRE	**H**ypoxia **R**esponse **E**lement
LB	**L**ysogeny **B**roth
LDPE	**L**ow **D**ensity **P**oly**e**thylene
OD	**O**ptical **D**ensity
PBT	**P**oly**b**utylene **T**erephthalate
PC	**P**oly**c**arbonate
PCR	**P**olymerase **C**hain **R**eaction

PDMS	**P**oly**dim**ethyl**s**iloxane
PLA	**P**olylactic **A**cid
PMMA	**P**oly**m**ethyl**m**eth**a**crylate
PTFE	**P**oly**t**etra**f**luoro**e**thylene
PS	**P**oly**s**tyrene
PtOEPK	**Pt**(II) **O**cta**e**thyl**p**orphine **K**etone
RCF	**R**elative **C**entrifugal **F**orce
RFP	**R**ed **F**luorescent **P**rotein
RTDP	**R**uthenium **T**ris(2,2'-**dip**yridyl) Dichloridehexahydrate
STL	**ST**ereo**L**ithography
THF	**T**etra**h**ydro**f**uran
THY	**T**odd-**H**ewitt Broth with 2% **Y**east Extract
VEGFA	**V**ascular **E**ndothelial **G**rowth **F**actor **A**

Summary

This thesis covers the development of three devices for investigating biological systems: A 3D-printed oxygen control insert for a 24-well plate, an open source 3D-printable micropipette, and a droplet device to investigate genetic transfer between pairs of *S. pneumoniae*.

Microfluidic platforms have been developed to provide more physiologically relevant oxygen environments for cell studies. Typically, building these platforms involves manual fabrication of microfluidic chips, a process that is time consuming, has a high failure rate and produces limited geometries. Recently 3D printing has emerged as a method for directly printing complete microfluidic devices, although printing materials have been limited to oxygen-impermeable materials. We demonstrate the addition of gas permeable polydimethylsiloxane membranes to a 3D-printed microfluidic devices as a means to enable oxygen control cell culture studies in a standard multiwell plate.

Scientific communities are drawn to the open source model as an increasingly utilitarian way to produce and share work. Initially used to develop freely available software, the open source model has been applied to hardware including scientific tools. Increasing convenience of 3D printing has fueled the proliferation of open labware projects aiming to develop and share designs for scientific tools that can be produced in-house as cheap alternatives to commercial products. We present our design of a micropipette that is assembled from 3D-printable parts and some hardware that meets ISO 8655 standards for accuracy and precision.

In genetic transformation (GT), cells take up and incorporate DNA from the environment. GT allows rapid alterations of the genome resulting in persistent infections as polyclonal biofilms share drug resistant genes and overcome immune response. In vitro procedures, GT is studied in suspensions of billions of cells and can be used to assay transfer of traits between strains, but does not reproduce the rapid and extensive of transfer observed in vivo. A flow focusing droplet generating device is demonstrated to encapsulate *S. pneumoniae* in droplets which allows imaging of encapsulated cells.

Chapter 1

Introduction and Background

(Previously published as Martin D Brennan, Megan L Rexius-Hall, Laura Jane Elgass, and David T Ed- dington. Oxygen control with microfluidics. Lab Chip, 14(22):4305–4318, 2014. ISSN 1473-0197., Martin D Brennan, Megan L Rexius-Hall, and David T Eddington. A 3D-Printed Oxygen Control Insert for a 24-Well Plate. Plos One, 10(9):e0137631, 2015. ISSN 1932-6203., Martin Brennan, Fahad Bokhari, and David Eddington. Open Design 3D-Printable Adjustable Micropipette that meets ISO Standard for Accuracy. bioRxiv, 2017. Permissions statements are included in Appendix D.)

1.1 Oxygen Microfluidic Control and 3D Insert

1.1.1 Normoxia and Hypoxia in Cells and Tissues

Oxygen makes up approximately 21% of the atmospheric air that enters the lung, yet most tissues of the body experience significantly less. Normoxia is the range of oxygen levels that tissues experience in a healthy system. Within the body oxygen levels vary depending on the specific tissue. Oxygen levels in lung alveoli are ∼13%, yet different regions of the brain, for example, can range from 7% to less than 1% (a list of reported oxygen levels can be found in Table 1.1). Despite the fact that normoxia for most tissues is far below 21%, culture studies are typically done at atmospheric levels, which is in effect hyperoxic[10].

TABLE 1.1: The physiologic oxygen levels vary for different human tissues. The indicated normoxic levels are all below atmospheric (21%) oxygen. Values compiled from refs. 7–9.

Tissue	Physiologic Oxygen (%)
Lung alveoli	13
Liver	10–13
Arterial blood	10–13
Venous blood	5
Bone marrow	0.5-7
Brain	0.5–7
Cartilage	1

Oxygen control in cell studies is often overlooked by researchers, but important for mimicking conditions experienced by cells in vivo. For example, tumors are generally hypoxic as cancer cells rapidly outgrow their vasculature creating a poorly perfused, hypoxic inner region[11]. Studying cancer cells under controlled hypoxic conditions is important in understanding the pathophysiology because research has shown hypoxia may enhance aggressive phenotypes, tumor progression, metastasis, and resistance to therapy[12–14]. Hypoxia is known to alter the transcription of many genes which are under the activity of the HIF (hypoxia inducible factor) family of transcriptional factors[15–17]. To better study the role of oxygen levels in cancer gene expression, a gas controlled culture system is required. Tissue oxygenation is a constant balancing act between oxygen availability and oxygen consumption. Small changes in oxygen levels trigger homeostasis responses in cells and tissues. Research has found that hypoxia induces extensive alterations in gene expression. The hypoxia inducible factor (HIF) family of transcription factors have been shown to activate as oxygen levels fall and the work to regulate gene expression that promotes glycolysis, angiogenesis.

1.1.2 Diffusion, Solubility, and Transport of Oxygen in Microfluidic Devices

Because microfluidic systems are characterized by low Reynolds numbers, no turbulent flow is present to enhance mixing within a microfluidic system, and so simple diffusion adequately describes the transport of diffusive species within a microchannel. Simple—or Fickian—diffusion is described by

$$J = -D(\frac{\partial C}{\partial x}) \tag{1.1}$$

where J is the diffusive flux, D is the coefficient of diffusion for a chemical species in a given medium, and C is the concentration of the chemical species. The relationship

$$x^2 = 2Dt \tag{1.2}$$

describes the mean-square displacement of a particle in relation to time lapsed in the system. Because time depends on the square of displacement, diffusion on the microscale is much faster than diffusion on the macroscale. In order to illustrate the effect of scale on diffusion time, consider two observers in a room with a jar of sulfur. Observer one is positioned 10 micrometers away from the jar, while observer two is positioned one million times farther away at 10 meters from the jar. At $t = 0$, the jar is opened and at t_1 the sulfur molecules (and odor) reach observer one at 10 micrometers. At t_2 the sulfur molecules reach observer two at 10 meters. Considering only Fickian diffusion as a method of transport and making use of equation (1.2), it would take 10^{12} times longer for the molecules to reach observer two at 10 meters as it would to reach observer one at 10 micrometers. Using a realistic diffusion coefficient of 0.16 $\text{cm}^2\text{sec}^{-1}$ for sulphur in air, observer one would smell the sulphur in 30 nanoseconds while observer two would be spared for 8 hours and 40 minutes. Of course in reality, an observer on the macroscale would be able to smell the sulfur rather quickly, but that is due to the presence of turbulent flow and thermal gradients which facilitate transport in the air. While relying on diffusion for an experiment at the macroscale would be an either costly or impossible time commitment, diffusion can be a readily leveraged mode of transport at the microscale and within microfluidic devices.

PDMS (polydimethylsiloxane) is a commonly used polymer in microfluidics due to its many desirable qualities, including but not limited to optical clarity, biocompatibility, and its ability to be molded down to sub-micron resolution. For this discussion, though, of interest is its high permeability to gas, as it is the most permeable of the elastomeric polymers [18]. Microfluidic experiments for oxygen control frequently involve gas diffusion from a channel through a thin PDMS layer (or membrane) into another area of the device—perhaps another channel or a reservoir.

From Fick's Law, one can determine that, at steady-state and when either side of the membrane is exposed to gas, the permeability P of a polymer membrane to a gas can

be described by

$$P = J(\frac{dx}{dp}) \tag{1.3}$$

where dx is the membrane thickness and dp is the difference in pressure experienced by the two sides of the membrane. From this equation, it is simple to see that diffusive flux through a membrane will increase with greater pressure difference across the membrane and with decreased membrane thickness.

When considering a typical diffusion membrane in a device as an example, one side of the membrane has gas flowing from a pressurize tank and the other side has ambient air, the diffusive flux experienced by either side is dependent on the net flux of a diffusive species into or out of the membrane. It is important to note that this is really a dynamic process as the gas entering or exiting the membrane can be offset somewhat by sorption to or desorption from the membrane of the same chemical species. At equilibrium, this should result in a constant net flux into and out of the membrane, and the flux through any single step (gas channel to membrane, through the membrane, and membrane to reservoir) is considered the same as the flux through the membrane, and may be defined as

$$J = k_1 \frac{D}{D(k_1 + k_2) + k_1 k_2 dx}(c_1 - c_2) \tag{1.4}$$

where D is the diffusivity of the gas through the membrane, k_1 and k_2 are the desorption rate constants at each interface of the membrane, and c_1 and c_2 describe the concentrations of the gas in the polymer, according to

$$c = pS \tag{1.5}$$

where p is the gas pressure on either side of the membrane and S is the solubility of the gas in the polymer. However, when one side of a membrane is exposed to a liquid, this relationship is no longer accurate because gas flux, J, is reduced, and the desorption rate constant of the side of the membrane exposed to liquid, k_2, is different than the rate constant of the side of the membrane exposed to gas, and can now be described by

$$k_2 = \frac{Dk_1}{D + k_1 \triangle x + \rho_w k_1 D} \tag{1.6}$$

where ρ_w is the wet mass transfer resistance.

In addition to changes in the behavior of sorption and desorption from polymeric membranes depending on the surrounding medium, it is also important to note the differences in the way gas—specifically oxygen for the purposes of this paper—behaves in PDMS versus water. For an excellent in depth analysis, Kim *et al.* present a mathematical analysis of oxygen transport in microfluidic systems [19]. Under identical conditions, oxygen gas is 1.7 times more diffusive in PDMS than in water, and six times more soluble in PDMS than in water [20].

1.1.3 Measurement of Oxygen

To investigate the effects of oxygen on biological systems one first needs to find a suitable method for measuring it. Measuring oxygen in the cell environment is even more challenging if temporal and spatial requirements are strict. Stoichiometric methods such as the Winkler method [21] are too slow and require fixing of samples.

1.1.3.1 Clark-style Electrodes

Clark-style electrodes [22] typically use a platinum working electrode and silver chloride reference electrode with potassium chloride for the electrolyte. A voltage of about 800 mV, which is sufficient to reduce oxygen, is applied across the electrodes. Oxygen is reduced at the working electrode, thus producing electrons or current proportional to the amount of oxygen present. The electrodes and electrolyte are protected behind a gas-permeable layer of polytetrafluoroethylene (PTFE) to prevent adsorption of proteins or interfering ions from fouling the electrodes. Because Clark-style electrodes consume oxygen in order to detect it, stirring of the sample is usually required for fast response measurements. The electrode is also very sensitive to changes in sample temperature. Clark electrodes are unreliable for long-term measurements for a number of reasons which contribute to unstable readings: depletion of the electrolyte, the production of OH^- ions affecting the pH causing zero drift, and the anode becoming coated in AgCl. If used with biological samples, the protective, PTFE membrane will also lose permeability over time due to the adsorption of protein and other residues. Clark-style electrodes also suffer from low temporal and spatial resolution due to the time it takes for oxygen to diffuse across the PTFE membrane and to the electrodes. In addition, the relative size

of these probes ($\sim$3+ mm diameter probe) makes interfacing with microfluidic channels problematic.

1.1.3.2 Optical Oxygen Sensors

For microfluidic systems, optical oxygen sensors are the tool of choice. They have several advantages over Clark-style electrodes. They do not consume oxygen, so they can be used in low or no flow environments and do not suffer from fouling, making them stable for long-term studies. Where Clark electrodes require an electrical connection to each position to be measured and only provide a single, low spatial resolution measurement, optical sensors allow measurement over the entire area of the sensor and at any number of discrete points. These sensors take advantage of oxygen-indicating fluorophores that are quenched in the presence of oxygen. The degree of quenching is determined by the oxygen partial pressure. The relationship between intensity and oxygen partial pressure is described by the Stern–Volmer equation:

$$\frac{\tau_0}{\tau} = \frac{I_0}{I} = 1 + K_q\tau_0[\mathrm{O_2}] \tag{1.7}$$

where I_0 and τ_0 are the intensity and excited state lifetime in the absence of oxygen, τ is the excited state lifetime in the presence of oxygen, $[\mathrm{O_2}]$ is oxygen concentration, and Kq is the quenching constant. A Stern-Volmer calibration curve must be made for each sensor and application. When a sensor is calibrated, a corresponding Stern-Volmer curve is created by measuring the intensity at no fewer than two known oxygen partial pressures. The intensity data collected is fitted to the Stern-Volmer equation to elicit the corresponding oxygen partial pressure (Figure 1.1). Typically, a basic fluorescent microscopy setup is sufficient to monitor a fluorescent sensor-equipped device, although custom excitation/detector modules can also be created for portability, miniaturization, or placement in an incubator [23]. Fluorophores are sensitive to photobleaching, where the intensity becomes attenuated after long term constant excitation, but short periodic exposures are typically used to avoid photobleaching. In addition to simple intensity-based measurements, fluorescence lifetime imaging microscopy (FLIM) uses a modulated excitation source and detects the decay in intensity in either the time or frequency domain. This method can be used to reduce background luminescent artifacts, sensitivity

to ambient light sources, and variations in intensity due to the concentration of the dye
[24].
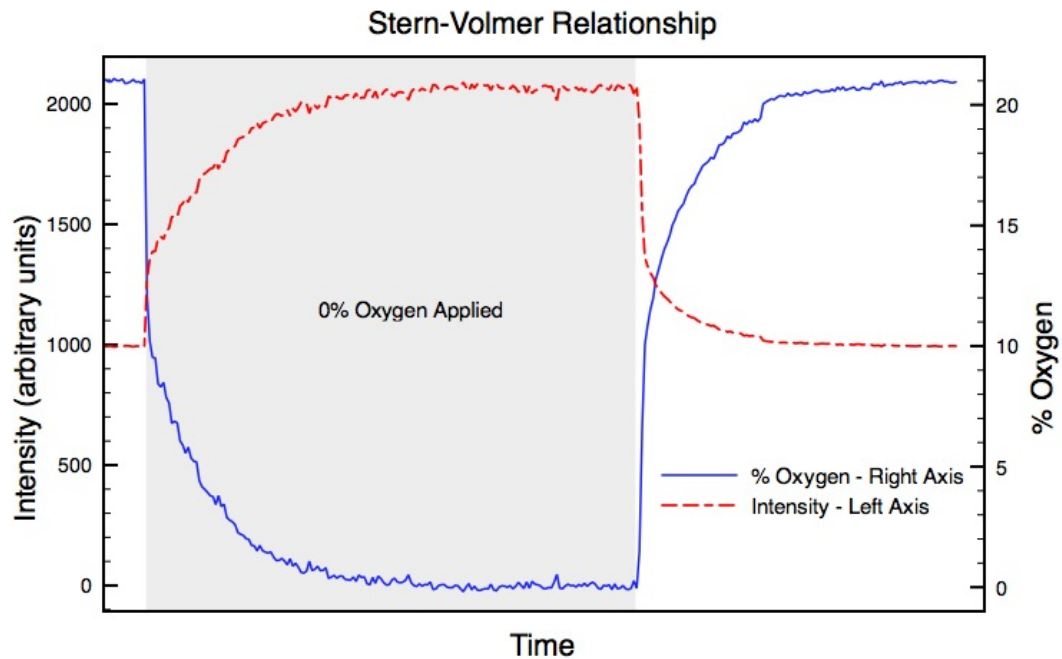
FIGURE 1.1: **Example calibration data.** This plot demonstrates the response in
luminescent intensity of a PtOEPK thin film due to application of a 0% oxygen en-
vironment (100% nitrogen). The sensor is first exposed to 21% oxygen atmospheric
mix (initial white region), then a 0% oxygen environment is applied by flowing 100%
nitrogen over the sensor (grey region). As oxygen is purged, the intensity of the sensor
increases due to decreased quenching (red dotted line). The 0% oxygen environment
is flushed out with a 21% oxygen mix resulting in a decrease in intensity to the initial
level (rightmost white region). The Stern-Volmer relationship is then used to calculate
and plot the corresponding oxygen percent (blue solid line).

There are two main types of oxygen indicating fluorophores: ruthenium-based and
metalloporphyrin-based. Oxygen-indicating fluorophore dyes such as these can be in-
corporated into sensors and probes to fit many applications. The simplest method may
be directly flowing a suspension of 1 mg/ml of ruthenium tris(2,2'-dipyridyl) dichloride
hexahydrate (RTDP) through the device channels. This allows measurement of oxygen
tension throughout the entire fluidic network. Although ruthenium based dyes are toxic,
this has been performed in live mammalian cultures with less than 10% mortality for 5
hours of exposure [25, 26].

To avoid adding toxic dye into culture media, the dyes can be permanently incorporated
into a polymeric matrix and embedded into channel walls or features. A thin film

platinum(II) octaethylporphyrin ketone (PtOEPK) sensor can be made by dissolving polystyrene (PS) in toluene (35% w/w toluene/PS), then adding 0.5 mg/ml of PtOEPK and mixing on a shaker for several hours. A small amount of this solution can be spin coated onto a glass slide. The toluene is then allowed to evaporate, leaving PtOEPK in a thin PS layer. This PS/PtOEPK sensor can be cut and installed in regions where oxygen tension measurements are to be taken [27, 28]. Oxygen indicating dyes can also be incorporated into a fiber-optic probe. The fluorophore is housed in an oxygen permeable construct at the tip of a fiber optic probe. With a proper optical setup, excitation and detection can now be performed through the fiber. Oxygen can be monitored by placing the fluorophore-doped tip in the sample or network. The advantage of fiber optic oxygen sensors is they can be moved within the sample during measurements and be reused. Park *et al.* developed fiber optic probes with submicron tips with the intention of monitoring intercellular and intracellular oxygen. The sensors were made by dipping the silica fibers into PtOEPK/PVC dissolved in tetrahydrofuran (THF) [29].

1.1.4 Methods for Global Oxygen Control and Measurement

To study cellular behavior in low concentrations of oxygen, hypoxic chambers, workstations, and perfusion chambers have been the most widely used tools to create hypoxic environments. Unfortunately, these tools offer a single choice of a hypoxic level at a time. The homogeneous oxygen levels provided also do not replicate oxygen gradients found in vivo which form from radial and axial diffusion of oxygen from the microvasculature and metabolic consumption of oxygen by surrounding cells. Ultimately, the single oxygen level macroenvironments in such culture systems do not establish oxygen gradients that are physiological.

1.1.4.1 Hypoxic Chambers

Hypoxic chambers remain as the tool of choice for imposing variable oxygen conditions because they are small enough to be housed inside a standard incubator, do not require specialized equipment for operation, and have the added advantage of being inexpensive (~$500) as compared to hypoxic workstations (~$50,000). Their price has made hypoxic chambers an attractive tool for labs interested in studying cells in low oxygen tension but not necessarily specializing in hypoxia. The hypoxic chamber consists of a vessel in

which to place cell culture plates and dishes that can then be purged with a gas mixture of interest, sealed, and placed in an incubator. However, hypoxic chambers are prone to leaks, are inherently low throughput, require considerable incubator space, cannot replicate anoxic conditions even when purged with nitrogen, equilibrate slowly (on the scale of several hours), and are not compatible with microscopic analysis. Additionally, the oxygen level within a hypoxic chamber is imprecise. The oxygen concentration is not stably the same concentration as the infused gas throughout the chamber as transport limitations create a discrepancy between the gas concentration within the infused headspace and the gas concentration at the bottom of the culture dish.

1.1.4.2 Hypoxic Workstations

The hypoxic workstation is a relatively large, sealed biosafety cabinet purged with a gas of interest, monitored with oxygen sensors, and equipped with its own incubator in one corner of the cabinet. Due to its cost, the hypoxic workstation is generally only found in labs specializing in hypoxia research. A workstation is attractive because, as compared to the hypoxic chamber, it is equipped with a small, gas-modulated bench top to perform conventional biological assays such as western blot and PCR (polymerase chain reaction) preparations. The workspace is useful because hypoxic factors, like the HIF family of transcription factors, degrade rapidly upon re-equilibrating with atmospheric oxygen. Therefore, performing such assays in a sealed, hypoxic environment is ideal to achieve the best results. Atmospheric equilibration is a concern when using hypoxic chambers, rather than hypoxic workstations, as they must be opened to retrieve cell culture contents or even to change media, forcing equilibration with ambient surroundings and an unintended intermittent hypoxia exposure which has been found to alter cell fate and function [30, 31].

Though the workstation offers a precisely controlled, homogeneous oxygen environment and space to perform biological assays, the setup is cumbersome. Small, delicate manipulations must be done from outside the cabinet while wearing bulky, integrated rubber gloves. Additionally, like the hypoxic chamber, the workstation cannot be easily coupled to live-cell microscopy unless a microscope is housed within the incubator. Overall, the hypoxic workstation is expensive and leaves too large of a footprint to be readily accessible to a wide population of researchers.

1.1.4.3 Perfusion Chambers

Another option is a commercially available perfusion chamber in which oxygen concentration is able to be modulated by alternating the flow of oxygenated and deoxygenated liquid that is mixed to defined ratios through the chamber. Like the hypoxic chambers and workstations, perfusion chambers lack spatial control. The effect of the added shear stress that comes along with the flow must also be considered with use of perfusion chambers. Shear stress is known to alter cell morphology and gene expression [32–34], so the consequences of non-negligible shear stress should not be underestimated.

Microfluidic platforms have been developed to overcome the inherent limits of these current methods, including lack of spatial control, slow equilibration, and unachievable or difficult coupling to live-cell microscopy. The various applications made possible by microfluidic systems are the topic of the following sections.

1.1.5 Microfluidic Methods for Oxygen Control

Many different methods for oxygen control have been applied to different biological systems, and serve purposes outside of solely controlling oxygen concentration, ranging from improving the quality of an experiment, to creating a more physiologically realistic environment in which to grow cells, to studying the mechanisms of different diseases. Several variations of microfluidic platforms have been used to generate the desired oxygen environment for these experiments, including devices that rely on diffusion from fluid, utilizing on-or-off-chip mixers and equilibration steps, leveraging cellular oxygen uptake to deplete the oxygen, and using chemical, electrolytic or photocatalytic reactions to produce oxygen directly on chip. Microfluidics platforms have been used to control the oxygen microenvironment and to measure the effect of oxygen concentration on biological materials in a variety of ways, including exposing biological specimens to various constant concentrations of oxygen, discrete regions of different oxygen concentrations, and oxygen gradients. Microfluidic systems for controlling oxygen at the microscale have been applied to address a variety of physiologically relevant questions, for examining the behavior of cells in different and tightly-controlled oxygen environments, and they have been applied to studying specific pathologies including cancer, stroke, and sickle cell disease.

1.1.5.1 Diffusion from a Source Fluid

Perhaps the most popular and straightforward method for oxygen control in microdevices is by diffusion from a source or control channel across a thin, gas-permeable PDMS membrane and into the cell culture region. The source fluid in the control channel rapidly diffuses to control the dissolved gas environment experienced by the cells.

Equilibrated Liquid.   Exposing cells and tissues to different oxygen levels can be accomplished by flowing a pre-equilibrated liquid through the device's control channels. In many cases, media is equilibrated with the appropriate gas before introducing it to cultures. For instance, a commonly used method to mimic the induction of hypoxia is to place cell cultures in medium that has been bubbled with nitrogen [35]. The equilibration of media with nitrogen is frequently done in addition to housing the cultures in a hypoxic chamber or gas-controlled incubator [36] to reach even lower levels of oxygen. In microfluidic systems, cell culture media is also frequently equilibrated with appropriate gas mixtures to control oxygen content. In these systems, constant perfusion of the equilibrated media is usually necessary to maintain the desired oxygen level. Without an ideal, closed system, the oxygen concentration of media will re-equilibrate with ambient surroundings (i.e. the atmosphere) over time.

One example is the work by Grist *et al.* where diffusion from liquids was used to establish oxygen gradients across a central channel. To create the on-chip oxygen gradient, off-chip gas bubbling flasks produced deoxygenated and oxygenated water, which was fed via oxygen-impermeable tubing into designated control water channels. A deoxygenated control water channel flanked one side of a media perfusion chamber containing cells, while an oxygenated water channel flanked the other side. Only a thin, PDMS membrane of $\sim$100 μm separated the control water channels from the cell chamber. The high gas permeability of PDMS and the difference in the oxygen level in the control water channels allowed for the spatial gradient generation in the cell chamber. The perfusion rate of the oxygenated or deoxygenated water (100 μL/min) was maintained by syringe pumps which withdrew media, creating negative pressure to pull the liquid through the device.[37].

Gas Perfusion. Flowing gas directly though the control channels eliminates the need for the pre-equilibration of liquid off-chip. Gas also has the advantage of having a lower viscosity than water, allowing for more rapid mixing. Additionally, flow is driven with large pressurized sources (gas tank), eliminating the need for syringe pumps. The convenience and simplicity of gas perfusion make it an easy choice for researchers wishing to accomplish more complicated experimental schemes discussed in detail below. The following devices demonstrate oxygen control in a variety of ways, including discrete control (obtaining multiple, uniform oxygen concentrations), spatial control (binary oxygen concentrations, and spatial gradients of oxygen concentrations), and temporal control (switching between oxygen concentrations at set time intervals or maintaining a constant oxygen concentration over time).

Leclerc *et al.* present an early demonstration of oxygen modulation in a microfluidic device. The system is a bioreactor composed of four microfluidic cell culturing regions stacked one on top of the other, with a media perfusion channel providing flow to the cell culture chamber. Inserted into the middle of the bioreactor (flanked above and below by two cell culturing regions) is what the authors call an "oxygen chamber," which is connected via channels to the environment outside of the bioreactor. This served as a way to allow gas from the outside environment to easily modulate the oxygen conditions within the culturing chamber. After culturing, this oxygen chamber design resulted in a 5-fold increase in cell growth compared to a 2-layer bioreactor and 8-fold increase compared to a 4-layer bioreactor without the oxygen chamber. Additionally, albumin production was monitored from cultured hepatocytes and only the cells grown in the 4-layer bioreactor with the oxygen chamber showed increased albumin production over a 12-day experiment [38]. Although the oxygen modulation is completely passive in this device, it represents a conceptual prototype for the more intricate control devices to follow.

A number of devices exist for exercising a discrete series of constant oxygen concentrations. These devices may be designed such that one device contains several isolated regions of discrete oxygen concentrations, or such that they maintain constant oxygen concentrations over a period of time. Vollmer *et al.* presented a system for dynamic delivery and sensing of oxygen in perusing medium when oxygen is delivered via a gas channel. PtOEPK oxygen sensors are placed in etched wells of a glass slide at the inlets

and outlets of a microfluidic network to monitor oxygen levels. A custom excitation/-collection module was created to house the device and monitor oxygen levels from the sensors. Again, oxygen diffuses from a gas channel across a PDMS membrane and into liquid channels. While this system is not applied to biological studies, it is an early example of the use of *in situ* PtOEPK sensors for oxygen characterization, and is a major advance in the development of microfluidic platforms for oxygen control of the microenvironment [28].

Polinkovsky *et al.* present two devices in which individual growth chambers within two microfluidic devices take on discrete values, ranging linearly between 0 and 100% oxygen concentration over nine chambers in one device, and exponentially from 0 to 21% oxygen concentration over nine channels in the second device. In these experiments, ruthenium dye was used to characterize the oxygen levels. For each device, the oxygen concentrations in the gas channels are achieved by flowing two gases through a three-step on-chip mixing channel network, culminating in nine separate channels of discrete concentration that flow over the growth chambers, which contain media. The growth chambers can be used to culture yeast, bacteria or mammalian cells, and for the purposes of this experiment, *E. coli* division rates as a function of oxygen concentration were determined [39]. This device is interesting and useful because it presents a way to use one device to deliver many oxygen concentrations, and this, in conjunction with multiple growth chambers, means that high-throughput oxygen-controlled experiments can be conducted.

Lam *et al.* present a microfluidic platform for culturing aerobic and anaerobic bacteria and mammalian cells. An on-chip mixer creates a series of discrete oxygen concentrations by mixing oxygen and nitrogen that range linearly from 0 to 42%, and cells were cultured in channels at these oxygen concentrations. Incorporated into the device is a valve multiplexer, which was used to replace media in each of the eight wells at regular intervals. A custom excitation module was designed using LEDs as the excitation source and paired with a custom infrared detection module. PtOEPK polystyrene sensors were embedded in wet-etched wells of a glass slide. The sensors were calibrated using water with different concentrations of oxygenated water and correlated with the Stern-Volmer analysis. Cell density and growth rates were studied with *E. Coli, A. Viscosus, F. Nucleatum*, and embryonic fibroblast cells [23]. This device couples oxygen and valve

control, and demonstrates that techniques necessary for cell culture (media replacement, in this case) can be incorporated into these experiments.

In addition to microfluidic culture chambers of custom microfluidic devices, Oppegard *et al.* developed a microfluidic insert for a standard 6-well plate, which can be used to modulate oxygen concentration in cell culture in lieu of a hypoxic chamber, and with better oxygen control than a hypoxic chamber. The device's oxygen concentration is characterized using a ruthenium coated substrate, and was further validated by monitoring HIF-1α expression in cells, to ensure that it agreed with expression levels from traditional methods. The device is an insert which nests into standard six-well plate, leaving a designated gap from the bottom of the plate. Gas is constantly perfused across the gas permeable membrane (PDMS), where it diffuses to oxygenate or deoxygenate the multiwell plate at the culture surface. The oxygen concentration within the device rapidly changes when the input gas is changed, and can maintain a steady oxygen concentration over five days [40]. The main innovation of this work was adapting microfluidic oxygen control to the 6-well plate which is a standard workhorse of biomedical research. In a follow up paper they expanded on this theme to develop an insert for Boyden chambers which also nest into a multiwell plate for cell migration studies. The ability to maintain an oxygen concentration in conjunction with the ability to adjust to a new oxygen concentration quickly when a new gas is flowed through the device makes it very useful for both constant oxygen concentration studies as well as intermittent hypoxia studies. Hypoxia studies were conducted using an invasive breast cancer cell line and it was found that intermittent hypoxia resulted in different migration than constant hypoxia [1].

Abaci *et al.* present a microbioreactor for consistent, long-term oxygen control of the microenvironment with live computer monitoring of oxygen concentration in the device. The format of the device is a top gas channel which is used to diffuse oxygen into a lower, closed culture channel via a PDMS membrane. Both channels are etched into polymethylmethacrylate (PMMA). Fluorescent sensors were used to monitor the device's dissolved oxygen level. The system is composed of sensor patches (flat $3mm$ discs), fiber-optic guides, and a 4-channel transmitter device which interfaces with a computer. Media was constantly perfused at a relatively slow flow rate of $0.02ml/h$. The temporal responses of the oxygen tension in the channel in static conditions in which the gas channel was supplied with discrete oxygen levels (21%, 5%, and 1%) was compared to
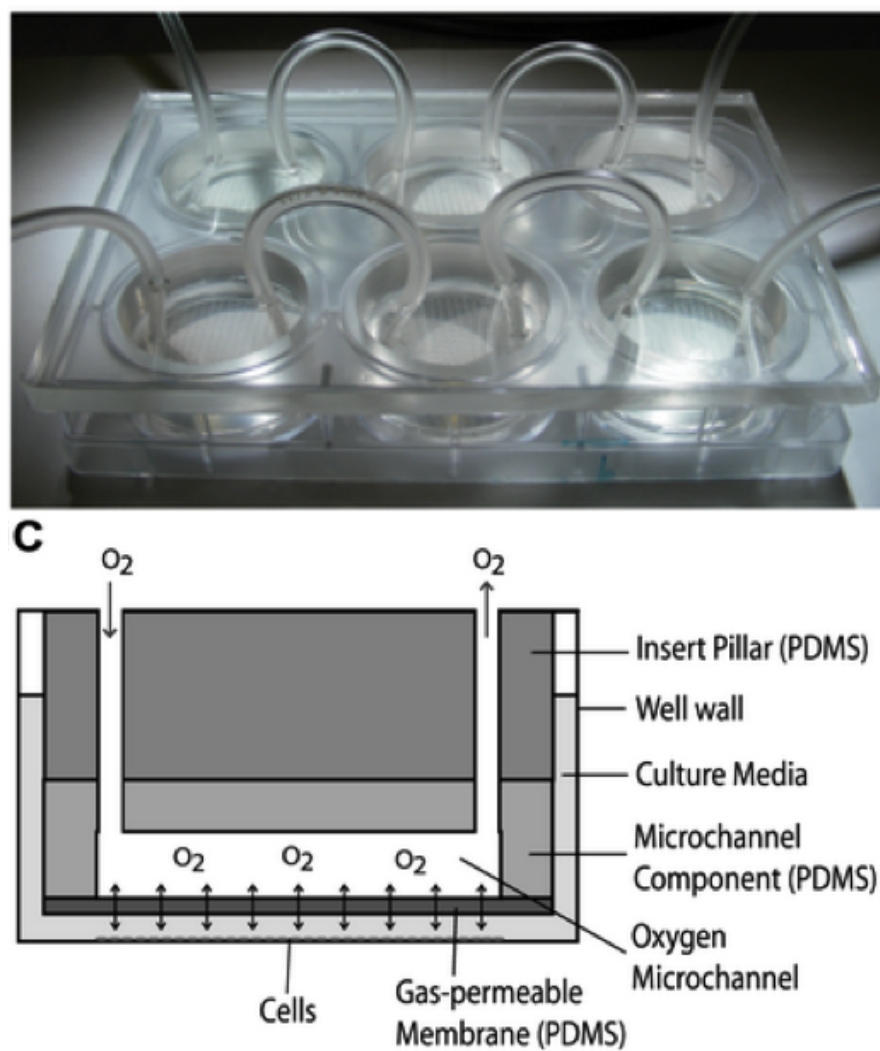
FIGURE 1.2: **An insert designed to control oxygen in a 6-well plate.** This device was cast completely from PDMS. Figures adapted from 1.

dynamic conditions which utilized the same discrete oxygen levels in the gas channel but also media perfusion in the culture channel at 0.5 ml/h were compared, and resulted in similar oxygen profiles. The shear stress introduced by perfusion was negligible compared to shear stress levels reported to affect cell behavior. To demonstrate the bioreactor's abilities, fibrosarcoma cells were cultured and cell viability, cell density and circularity tests were performed at 1% and 21% dissolved oxygen concentrations [41].

Another example of a microfluidic device used to study the behavior of cancer cells in hypoxic and normoxic environments is presented by Funamoto *et al.*, who designed a PDMS microfluidic device with an integrated 3D gel for cell culture flanked by media channels. Each media channel was separated from a gas channel by a 150 μm diffusion gap. Oxygen diffusion between the incubator environment and the PDMS device was

inhibited by a polycarbonate (PC) film bonded above the channels. The device was validated using a ruthenium-coated glass cover slip as an oxygen sensor. The device's utility was demonstrated by studying the migration of human breast cancer cells (MDA-MB-231) in hypoxia. Time-lapse live-cell 3D confocal imaging was acquired to determine the cancer cell migration within the gel extracellular matrix (ECM). Cells in the gel showed increased net displacement, total path length, and their ratio (persistence) increased under hypoxia as compared to normoxia. Despite demonstrating that the device design lends itself to establish a gradient across the gel, cells were not studied in a gradient. Increased migration corresponds with increased invasive behavior of breast cancer cells reported in other studies [42].

In another example, oxygen was used to control the polymerization of sickle-cell hemoglobin (HbS) blood as a model of a vaso-occlusive crisis in sickle cell disease. Again, gas diffuses from a gas channel, across a PDMS membrane, and into the blood perfusion network. Occlusive and relaxation events due to HbS polymerization and depolymerization, respectively, are measured as a function of oxygen concentration by monitoring blood flow velocity in their microfluidic device. The device is presented as a tool to study sickle cell disease and possible future clinically useful agents to block HbS polymerization. CO binding is used to demonstrate that HbS polymerization can be blocked even in cases of extreme deoxygenation [43]. This device represents the first model of the dynamic sickling process without influences of endothelial cells and a follow-up study will be discussed in a later section.

Lo *et al.* demonstrate a diffusion from gas device for a live mouse wound healing study. The device was designed for a live active mouse to wear the device as a topical oxygen therapy method. 100% oxygen was delivered to the device where it diffused across a 100 μm PDMS membrane placed in conformal contact with the wound. The study demonstrated improved collagen maturity in treated mice, although the oxygen therapy did not improve wound closure rates, or microvasculature development [44].

For some experiments, a binary oxygen concentration profile is useful to elicit a biological response as a result of exposure to two distinct oxygen regions. In the previously mentioned paper, Oppegard *et al.* show that an oxygen profile of a dual-condition microchannel can maintain a stable binary oxygen profile over fourteen days. Additionally, the author presents an interdigitated microfluidic channel network that generates a

cyclic oxygen profile [40]. Mauleon *et al.* modified an existing brain slice chamber with a PDMS membrane and microfluidic channel layer. This device allows different areas of a 350 μm thick brain slice to be exposed to different oxygen concentrations independently. Oxygen levels and calcium sensitive dyes were used to validate delivery of oxygen to discrete regions of brain slice anatomy [45, 46].

Other Methods for Oxygen Control in Microfluidic Devices Many other methods for oxygen control have been demonstrated that are beyond the scope of this thesis including the production of gradients[47, 48], the use of hydration layers to prevent evaporation of media[49, 50], using cellular consumption to deplete oxygen[26, 27, 51, 52], chemical generation and scavenging of oxygen[53–55], and photocatalytic cells[56] and electrolysis[29]. For continued reading see reviews [10] and [57].

1.1.6 3D-printing of Microfluidic Devices

3D printing of microfluidic devices enables rapid, one-step fabrication of complex designs infeasible to make with planar lithography and replica molding techniques[2, 58]. In addition, planar lithography is time consuming, requires specialized equipment and facilities, and has a high failure rate. It is not unusual for microfluidic labs to make ten microfluidic devices to guarantee one will work properly. On the other hand, 3D CAD printing allows for unambiguous specifications and nearly eliminates time and effort spent on fabrication which may be outsourced to a 3D printing company for around \$200/device[59]. 3D printing also allows integration of complex geometries not possible with planar lithography, such as hose barbs and luer fittings. Dissemination and distributed production is also vastly simplified due to easy sharing of the design as a CAD file. Due to these inherent advantages 3D printing has emerged as a method for directly printing complete microfluidic devices [59–63]. Many prototypical microfluidic device features have been recreated with 3D printing as a proof of concept for this new fabrication technique [59, 62] including modular re-configurable units[63–65]. 3D printed devices have been used for neuroengineering applications[66], inexpensive and high-throughput reactionware,[67–70], culturing and imaging arrays of seedlings[71], measuring dopamine and ATP levels in biological samples with an integrated electrode[72], or plate reader[61], and a bacteria separation flow assay[73, 74]. Other 3D-printed fluidic devices include pneumatic

valves[75] a custom nuclear magnetic resonance (NMR) cell[76], a rapid reconstitution package for lyophilized drugs[77] and flow plates for a water electrolysis system[78].

Printing is currently limited in choice of substrate compatible with the 3D printing process. Substrate options include many proprietary formulations which have been successfully used in a variety of applications. New techniques for using 3D-printed molds to produce devices[79–83] are also being developed, including fugitive ink methods[84–86]. To date, there are no widely available methods or materials to facilitate direct printing of gas-permeable materials, although this area is actively being explored[87]. Microfluidic cell culture devices are most commonly cast in PDMS as it is a convenient material for cell studies due to its biocompatibility, optical properties, and gas permeability, facilitating oxygen control of cell environments[10, 88].

Previously, our lab developed multiwell inserts for 6-well plates that controlled oxygen in a standard off-the shelf well plate [1, 40]. These devices were completely cast from PDMS and fabricated in a multiple bonding procedure. In addition, tubing was used to connect each pillar which became quite cumbersome when moving to a newer 24-well version. Utilizing 3D printing for the fabrication allowed further features to be incorporated, such as integrated distribution channels to eliminate the connection tubing between wells and hose barbs for better tubing connections, while eliminating fabrication time and failure rate. Although available 3D printable materials are gas-impermeable, the addition of a PDMS membrane following printing of the passive microfluidic network is a simple addition allowing gas transfer. In this case, having a gas-impermeable material for the bulk is advantageous as it reduces unwanted gas transfer from the bulk material prior to the gas exchange interface. The previous PDMS devices were Parylene coated along the convection channels to eliminate exchange of gas from the PDMS bulk, which again added to their complexity and is no longer needed. Convection and distribution of the gas is done in the impermeable material, eliminating dilution of the gas before reaching the diffusion layer.

1.2 3D Printing and Open Source Labware

1.2.1 3D Printing Methods

3D printing (also refereed to as additive manufacturing) is the process of producing three-dimensional CAD objects by building one layer at a time. Virtually any geometry can be designed and printed as a monolithic part without the production of any molds, machining or assembly. There are three primary 3D printing methods: powdered media fusion, fused deposition modeling (FDM), and stereolithography.
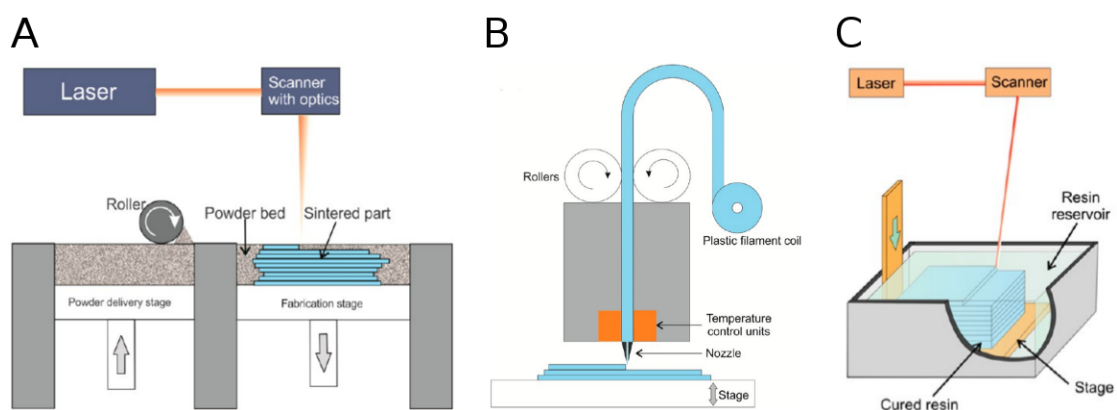
FIGURE 1.3: **Three primary printing methods.** (A) Powder media fusion. In this case, selective laser sintering is demonstrated. (B) Fused deposition modeling. (C) Stereolithography. Figures adapted from 2.

Powdered Media Fusion In powdered media fusion, a roller spreads a layer of powder on the build plate. The layer to be added is then defined by selectively fusing the pattern in the powder. The build stage then moves down a step and a new layer of power media is applied (Figure 1.3 A). Powder media fusion can be used to produce parts in a variety of material including plastics and metals and ceramics[2, 58]. One unique advantage of this method is that the unbound powder acts as a support for parts during the printing process.

Fused Deposition Modeling In fused deposition modeling (FDM) a thermoplastic filament is extruded through a heated nozzle. The nozzle traces the pattern of the slice depositing molten plastic. The stage is then moved down and the next layer is deposited on the previous one (Figure 1.3 B). FDM is the method used in consumer grade desktop printers. It is an inexpensive method but the resolution is low, typically 100 μm layers

are deposited with $\sim$30 μm x-y resolution[58]. Additionally, the materials are limited to thermoplastics.

Stereolithography In stereolithography, the slice is drawn with a laser in a photopolymer resin. The first layer is cured onto a stage, then the stage is moved and the next layer is added to the previous one (Figure 1.3 C). The advantage of stereolithography is the high resolution (as small as 25 μm layers), yet printers are expensive and are often limited to printing with proprietary resins[2].

1.2.2 Open-source Development Model Applied to Labware.

The open source development model, initially applied to software, is thriving in the development of open source scientific equipment due in part to increasing access of 3D printing[89, 90]. Additive manufacturing methods have existed for decades although the recent availability of inexpensive desktop printers[91, 92] have made it feasible for consumers to design and print prototypes and even functional parts, and consumer goods[93, 94]. Proliferation of free CAD software[95–98] and design sharing sites[99–102] have also supported the growth and popularity of open designed parts and projects. Open design 3D-printable lab equipment is an attractive idea because, like open source software, it allows free access to technology that is otherwise inaccessible due to proprietary and/or financial barriers. Open design tools create opportunity for scientists and educational programs in remote or resource limited areas to participate with inexpensive and easy to make tools[103–108]. Open source development also enables the development of custom solutions to meet unique applications not met by commercial products that are shared freely and are user modifiable[66, 93, 109–113]. Some advanced, noteworthy, open source scientific equipment include a PCR device[114], a tissue scaffold printer[115], and a two-photon microscope[116] although simple tools have potential to be impactful as they can serve a wider community.

1.2.3 Open Source Printable Labware

Some simple and clever printable parts that have emerged are ones that give a new function to a ubiquitous existing device, such as drill bit attachment designed to hold

centrifuge tubes, allowing a dremel to be used as a centrifuge[117]. Although this may make a rather crude centrifuge, it may be an adequate solution for a fraction of the cost of a commercial centrifuge. Other examples of open source research tools that utilize 3D printed parts include optics equipment[118], microscopes[119, 120], syringe pumps[3, 121], reactionware[67, 68, 70, 122], microfluidics[123, 124] and the list continues to grow[125].
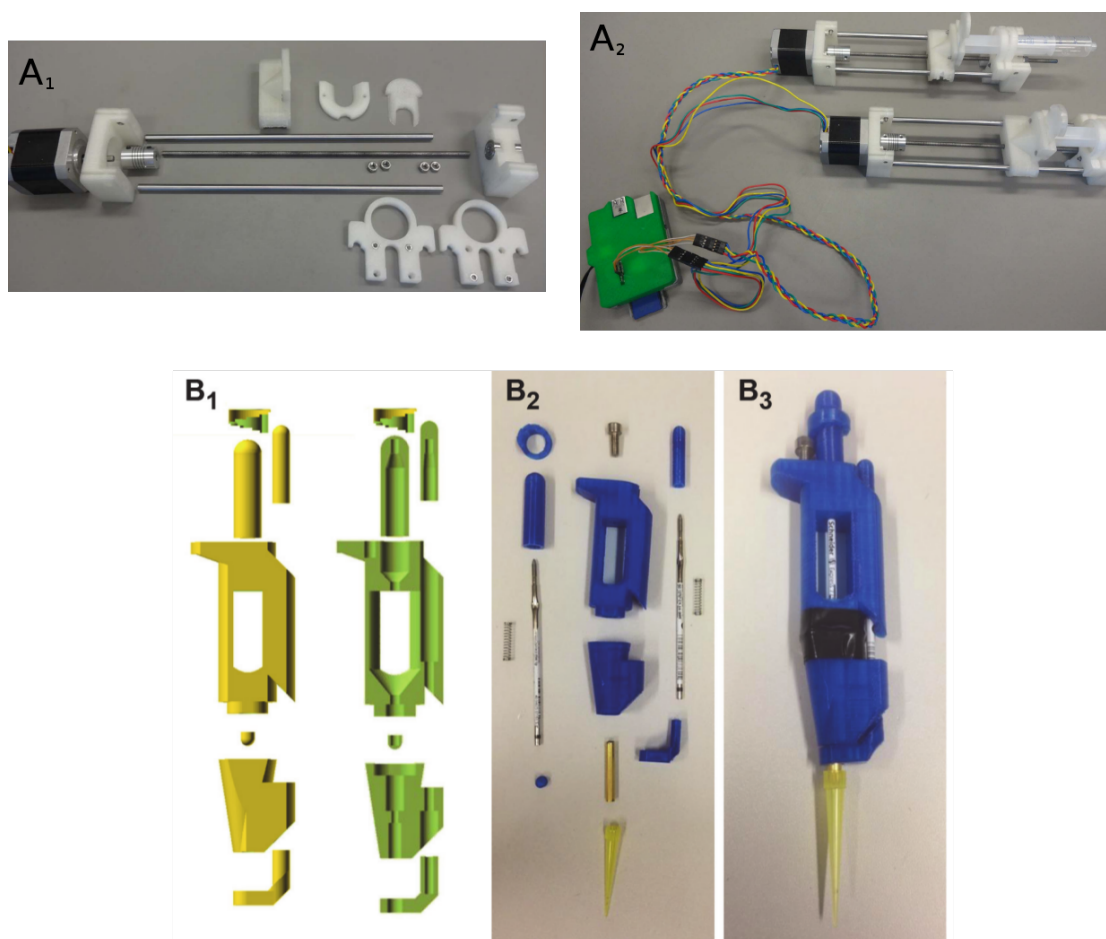
FIGURE 1.4: **Examples of open labware tools.** (A) A syringe pump made from printed parts and hardware, and driven with a Raspberry Pi controlled stepper-motor. (B) A micropipette made from printed parts and components scavenged from a retractable pen. Figures adapted from 3, 4.

1.2.4 Open Design Adjustable Micropipettes

One example of a everyday scientific tool that provides opportunity for an open design solution is the micropipette. An open design micropipette that can be made cheaply affords more options for labs and educational settings. Micropipettes are an indispensable tool used routinely in lab tasks and can easily cost $1000 USD for a set. Often a lab

will require several sets each for a dedicated task. Some pipettes may even re-calibrated for use with liquids of different properties.

Air displacement pipettes use a piston operating principle to draw liquid into the pipette[126]. In a typical commercial pipette the piston is made to be gas-tight with a gasketed plunger inside a smooth barrel. Consumer grade fused deposition modeling (FDM) printers are unable to build a smooth surface due to the formation of ridges that occur as each layer is deposited[127]. The ridges formed by FDM make it impractical to form a gas-tight seal between moving parts, even with a gasket. Existing printable open-design micropipettes get around this limitation by stretching a membrane over one end of a printed tube, which when pressed causes the displacement. The displacement membrane can be made from any elastic material such as a latex glove. A few open design micropipettes exist including a popular one which, in addition to the printed parts, uses parts scavenged from a retractable pen[4]. Because there is no built-in feature such as a readout for the user to set the displacement to a desired volume, this design requires the user to validate the volumes dispensed with a high precision scale. Without verification with a scale, the volumes dispensed can only be estimated based on calculations of the deflection of the membrane which is not a practical protocol.

1.3   Horizontal Gene Transfer and Droplets

1.3.1   Discovery of Transformation and DNA

In 1928, Griffith reported on the discovery of the "transforming principal", where an innocuous strain of pneumoconiosis was re-programed to be virulent[128]. First, Griffith demonstrated that injection of the live virulent strain resulted in a lethal infection in mice. Second, the same virulent strain was first killed with heat and then injected. This did not result in an infection and the mice lived. Third, the injection of a non-virulent strain did not result in a lethal infection in mice. Finally, Griffith injected a mixture of the non-virulent strain and the heat killed virulent strain which resulted in a lethal infection. Both virulent and non-virulent strains could then be isolated from the blood of the dead mouse. Somehow the presence of the virulent strain, although dead, passed information that allowed the non-virulent strain to transform and become virulent.

A subsequent study by Avery, McLeod and McCarty demonstrated that the presence of an overlooked substance, DNA, was responsible for re-programing strains[129]. At the time, it was believed that some yet to be discovered protein complex was the carrier of genetic information, but after this result scientists began looking more closely at DNA.

In 1951, Freeman demonstrated that a phage could re-program *Corynebacterium diphtheriae* from non-virulent to virulent[130]. This process is what is now referred to as transduction, one mechanism of horizontal gene transfer.

Meanwhile, Hershey and Chase found that the DNA is incorporated into the cell rather than the protein from the phage[131]. They confirmed this by producing two groups of phages, one with a radio labeled protein and one with radio labeled DNA. Their experiments demonstrated that the DNA was what was injected and stayed with the infected cell. James Watson's graduate study was on phages as well which began his path to the later modeling of the DNA molecule[132].

1.3.2 Mechanisms

Horizontal gene transfer (HGT) or (sometimes lateral gene transfer) describes the introduction of genes from an outside source which is distinct from vertical gene transfer where genes are passed from mother to daughter cells. HGT is the primary factor in evolution[133, 134], as well as the emergence of antibiotic resistance[135, 136]. The mechanisms of HGT are transformation, transduction and conjugation. **Transduction** involves a phage which carries and infects the host cell by injecting the DNA or RNA into the cytoplasm. In **conjugation**, genetic material is passed directly during cooperative cell-to-cell contact.

1.3.3 Transformation

Transformation is the uptake of exogenous DNA from the environment by a cell[137]. Many naturally transformable species of bacteria have been reported, such as *Streptococcus pneumoniae* and *Bacillus subtilis* and as well as many others[137]. In transformation, the recipient cell controls the process and expresses all the proteins required for DNA up-take and integration via homologous recombination. Homologous recombination is

used for repairing of double strand breaks in DNA and is also the process used to produce genetic diversity.

1.3.3.1 DNA Up-take in *S. pneumoniae*

Double strand DNA (dsDNA) encountered by a naturally transformable strain is first bound to the cell membrane and then taken into the cell with a specialized complex of membrane proteins[5, 138, 139]. First the DNA is bound to the cell and single strand breakages occur induced by binding proteins. As DNA is processed at the cell membrane, the 5' to 3' strand is degraded and released in to the extracellular space. The remaining strand is pulled into the cell from the 3' to 5' direction (Figure 1.5).

After DNA enters the cell, it is processed and scanned for homologous sequences as the recipient. The homologous sections act as markers for the donor DNA to physically interact with the recipient chromosome. In this way, new genes that are incorporated are done so in a guided way, by replacing genes of similar content. Non-homologous strands may form plasmids or are degraded. Finally, targeted sequences are integrated into the recipient DNA by homologous recombination and the resulting offspring are recombinant carriers of the new gene (Figure 1.5).
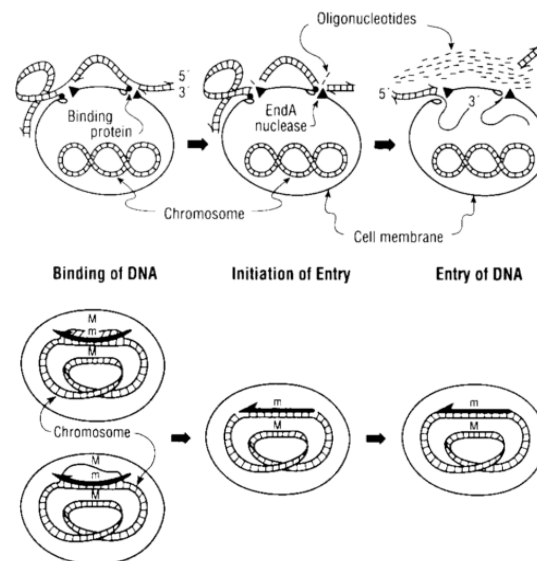
FIGURE 1.5: **Transformation mechanism in *S. pneumoniae*.** Figure adapted from 5.

1.3.3.2 Inducible Competence

S. pneumoniae relies on quorum sensing to activate to a state called competence which is the physiological ability to take up DNA. Upon reaching a high density, naturally transformable strains release a peptide pheromone that induces competence[140]. This peptide has been aptly named competence-stimulating peptide (CSP). Synthetically produced CSP can be used to induce competence in cultures even at low density. CSP has been found to be produced and detected by the competence (*com*) operon[141]. The detection of CSP activates the expression of at least 20 *com* genes[142] including those active in binding and up-take of DNA.

1.3.3.3 Competence-Induced Fratricide

It has been demonstrated that the induction of competence also triggers lysis in a fraction of population[143]. The lysis of the donor cells releases its DNA. This provides more available DNA for competent cells, which increases transformation efficiency. Lysis is caused by the production and release of bacteriolytic cell wall hydrolases, or fratricins. Fratricins narrowly affect closely related non-competent strains which are good candidates for homologous DNA[144]. The strain producing the fratricins also expresses a complementary protein which provides immunity. Competence is induced in naturally occurring strains when the population is high suggesting fratricide may serve as a check on growth or in preparation of an immune response[145, 146].

1.3.3.4 Transformation *In Vitro* vs. *In Vivo*

In research settings, transformation is typically studied between two well characterized cell types that are suspended in growth media. This provides a highly controlled environment but does not simulate the *in vivo* environment. Researchers have performed studies with lab-grown biofilms to attempt to more closely imitate a natural infection with promising results. The level of available donor DNA in cultured biofilms reaches higher concentrations[147]. The effectiveness of both fratricins and efficiency of homologous gene transfer is increased in biofilm cultures over suspensions[148]. Biofilm cultures may provide a better model but fail to reproduce frequency and extent of transformation observed in *in vivo* infections. Chronic bacterial infections typically involve

polyclonal populations. The nasopharyngeal environment provides the ideal place for polyclonal infections to thrive as biofilms. These *in vivo* biofilms result in highly efficient genetic transfer that is up to 10^7-fold higher when compared to septic infection[149]. Genome sequencing of nasopharyngeal samples taken from a patient six months apart revealed extensive transformation and the emergence of new strains[150]. Modeling suggests that the dramatic transfer that is observed *in vivo* is the result of not only continuous incremental events, but must also involve occasional extensive multi-fragment shifts[151]. These rarer transfers of long DNA fragments have not been demonstrated *in vitro*[152]. The biofilm infection's interaction with the mammalian host cells is difficult to imitate but models using epithelial cells have show better agreement to *in vivo* behaviour[153, 154].

Current studies using cell suspensions are only able to be analyzed as whole populations and do not reveal individual cell-cell transformation events.

1.3.3.5 Global Heath Considerations

S. pneumoniae causes pneumonia, meningitis and sepsis, which results an estimated 14.5 million cases of serious disease and $\sim$800000 deaths world wide in children younger than 5[155]. Treatment options include antibiotics and vaccines but can be quickly sidestepped by diverse and rapidly adapting strains. Recent targeted population studies have shown that the high selective pressure of these treatment options has resulted in the rapid spread of antibiotic resistance[156] and vaccine escape recombinants. Vaccines that target the capsule were highly effective when first introduced but due to this high selective pressure the rise of vaccine escape recombinants quickly followed[136, 157–159].

1.3.4 Droplet Microfluidics for the Encapsulation of Cells

Droplet microfludics makes and ideal platform for high-throughput sampling of single cells. Microfluidic technology can produce channels and droplets can be made to the same scale as cells and allows a multitude of probing techniques to be performed on-chip. Individual samples are created, isolated and manipulated by forming droplets of the sample in and immiscible carrier fluid. For biological samples this is typically an aqueous sample for the dispersed phase, in and oil carrier for the continuous phase.

1.3.4.1   Droplet Generation Techniques

Microfluidic droplet production is performed in three fundamental ways: T-junction, co-flowing, and flow focusing. The T-junction method where fluids intersect from two channels to one, produces large slugs that take up the width of the channels and produces droplets slow rate compared to other methods. Co-flowing involves three parallel channels. The dispersed phase channel is flanked by two continuous phase channels. At the droplet generating region the walls separating channels ends, causing the formation of droplets in the continuous phase. The flow focusing method is a special case of co-flowing, where the flow is hydrodynamically focused through a narrower neck just after the walls end that encourages the continuous phase to pinch off droplets from the dispersed phase. The advantage of the flow focusing method is a greater number of tunable parameters, and the ability to more easily produce droplets that are the size of the channels or smaller. A comprehensive review of these methods and more variations was authored by Zhu *et al.*[6].

1.3.4.2   Encapsulated Cell Analysis

Droplet encapsulation of cells allows enhanced and high-throughput analysis in a similar vain as flow cytometry methods. Cells can be encapsulated in droplets, manipulated, sorted, incubated and analyzed separately[160]. Systems can often be optimized to generate and process at rates exceeding 1000 droplets per second. Platforms have been developed to perform single cell PCR, cytotoxicity analysis, protein expression, antibody production and many more applications [161, 162]. Droplet analysis systems that have successfully been used with bacteria include digital PCR[163], screening for antibiotic resistance[164], biodiversity[165] and chemotactic sorting[166].

1.3.4.3   Limitations of the Poisson Distribution

Specific analysis may ofter require the encapsulation of a specific number of cells per droplet; for example, single-cell PCR requires one cell per droplet. Unfortunately, passive encapsulation methods are a random process, resulting in occupancy efficiency described by the Poisson distribution. The result is that cells are not uniformly distributed in droplets and even optimising cell density yields only a fraction of droplets with the target
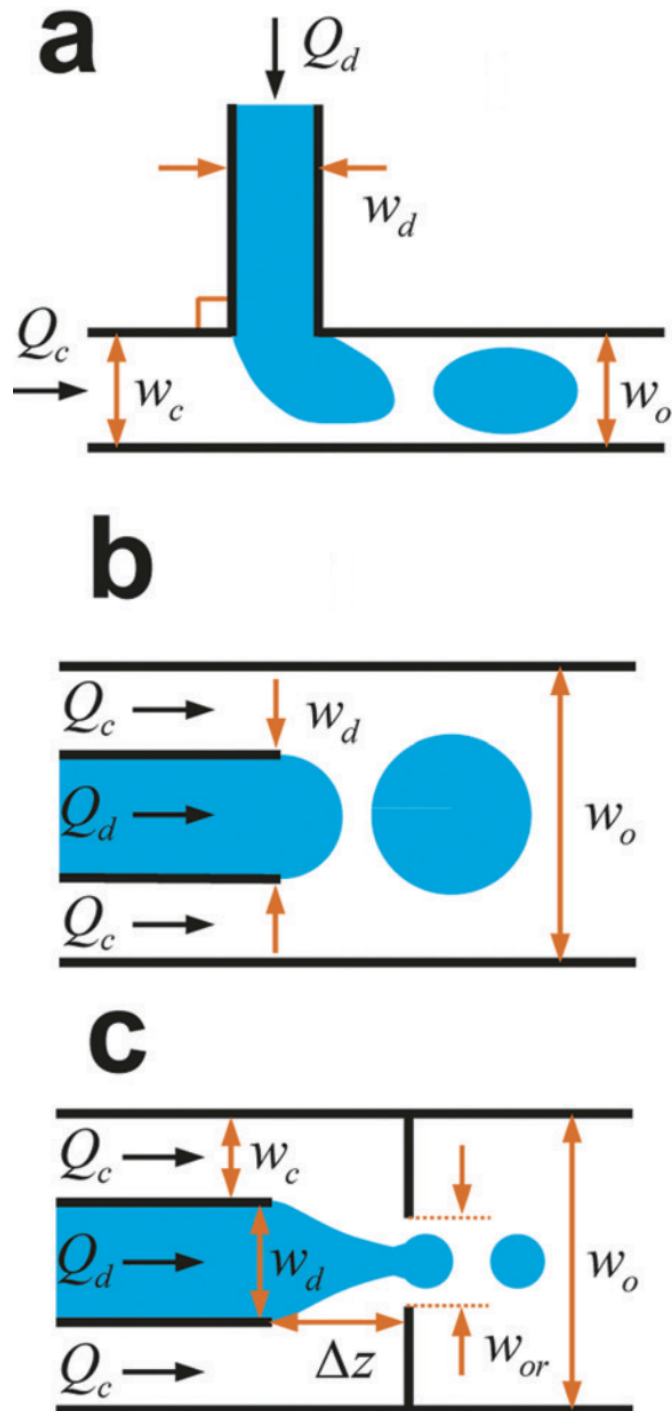
FIGURE 1.6: **Fundamental droplet generating methods for planar devices.**
(A) T-junction, (B) Co-flowing, and (C) Flow Focusing. Q represents flow rates of
continuous and dispersed phases, and w represents width parameters. Figure adapted
from 6.

number of cells. Many systems use down-stream droplet sorting to select for droplets
with target number of cells and eliminate others[167]. Methods that rely on inertial
focusing of cells into evenly spaced trains can increase uniform cell occupancy[168].

Chapter 2

Materials and Methods

(Previously published as Martin D Brennan, Megan L Rexius-Hall, and David T Eddington. A 3D-Printed Oxygen Control Insert for a 24-Well Plate. Plos One, 10(9):e0137631, 2015. ISSN 1932-6203., Martin Brennan, Fahad Bokhari, and David Eddington. Open Design 3D-Printable Adjustable Micropipette that meets ISO Standard for Accuracy. bioRxiv, 2017. Permissions statements are included in Appendix D.)

2.1   3D Printed Microfluidic Devices

2.1.1   Attempts at Casting 24-well Inserts with PDMS

Following the methods of Shawn Oppegard[1, 40] a 24-well version of the insert devices was first attempted to be cast in PDMS. An SU-8 master mold of a preliminary version of the distribution network (Figure 2.1) was made on a 6-inch silicon wafer. Dimensions for new 24-well format molds were specified and submitted to Eric Schmidt of UIC machine shop who machined the Delrin molds. The molds were designed to also hold the SU-8 master in place so the distribution network and well pillars were cast in one step. PDMS could be successfully cast and removed from the molds. Punching of holes through the narrower pillars on target to interface with the distribution network was very difficult and often caused splitting of the PDMS. Two holes need to be punched for each well for a total of 48 wells which was tedious and left a very small margin or error mistakes.

29

A new Delrin mold was designed with removable pins that would leave pre-cast through holes. Seepage of PDMS around the pins and uncured pockets of PDMS near the Delrin walls made very unsatisfactory molds. In addition, 48 pins had to be pulled from the casting with pliers before removing the molded PDMS. Because the pins did not directly interface with the distribution network, the holes had to be punched the rest of the way through anyway. A second, two-layer, SU-8 master mold was fabricated to make the membrane and cap for the bottom of each well with a compression mold, which was attached using uncured PDMS as mortar. To finish the devices, a glass plate with eight holes drilled for the ports was bonded to the top of the PDMS insert. Drilling of the the glass plate was also tedious and had a high failure rate. In ten attempts to make this device perhaps only one was successful.

Next, a "positive" insert, rather than a mold, was directly machined from Polysulfone, again by the UIC machine shop, complete with through holes bored and 200 μ tall chambers at the end of each pillar. The PDMS molded distribution network as well as the PDMS membranes were then attached with PDMS mortar to the Polysulfone insert. Unfortunately, the Polysulfone warped due to unpredictable internal forces that were expressed as the block was machined. This resulted in the pillars not being aligned in the z-direction and not reaching the specified 200 μm diffusion spacing between the membrane and the well bottom. Oxygen characterization with this device demonstrated very poor and non-uniform oxygen control (data not shown). These tedious and largely unsuccessful fabrication methods were abandoned and 3D-printable options were explored.

2.1.2 Design of 3D-printed Insert.

Here we report on the development of 3D-printed microfluidic devices for the control of oxygen in cell culture microenvironments. We demonstrate a device that nests into a 24-well culture plate to control gas in each row of the plate independently of the incubator's condition.

The device was designed to integrate with a multiwell format, specifically an off-the-shelf 24-well plate. The 24-well plate insert was designed to control gas in 4 rows of 6 wells each. Each of the 4 rows can be controlled independently from an input and also incorporates an integrated distribution network and hose barbs to simplify device

operation. The pillars extend into each well, leaving a ~500 μm gap for media between the diffusion membrane and the culture surface at the bottom of the well. Diffusion occurs rapidly across this gap, allowing control of the dissolved gas environment around the cells. The device also features a pipe within a pipe design so that gas flow enters and leaves the diffusion area in a uniform, and symmetrical flow pattern, which would not be possible with standard lithography, or the previously discussed techniques, and demonstrates the capabilities of 3D printing (Fig. 2.2).

Design of the Distribution Network   A distribution network stems from the central input that equalizes the flow along each path length by varying the channel width to the proximal, intermediate, and distal wells (Fig. 2.2). The resistances were equalized by working with the following formula:

$$rh^3x^3 - 8\mu Lhx^2 - 8\mu Lh^2 - 8\mu Lhx = 0, \tag{2.1}$$

where r is the fluid resistance, h is the channel height, x is the channel width, L is the channel path length, and μ is the viscosity of air. This formula was derived from electronic circuit theory, where resistance, current and voltage are analogous to fluidic resistance, flow and pressure, respectively. First this formula was used to calculate the resistance of the smallest channel possible for the 3D-printer to form, which is a 600 μm square. This channel is the one with the shortest path length from the inlet/outlet port. Then this resistance was used to calculate the widths for the intermediate and distal channels path lengths that would result in the same resistance in each channel. With the resistances the same in each channel, the flow rate should then be equally divided to each well. The resulting Reynolds number for even the largest channels of the distribution network are well below 100, resulting in laminar flow.
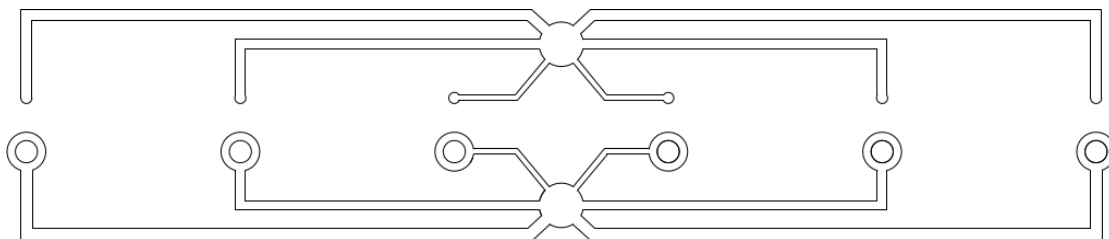
FIGURE 2.1: **2D distribution network.** Design of the distribution network with one inlet delivering gas to 6 wells. The return network mirrors the delivery network. The gas flow resistance in each channel is equalized by varying the width of channels dependent on their path length according the equation 2.1.
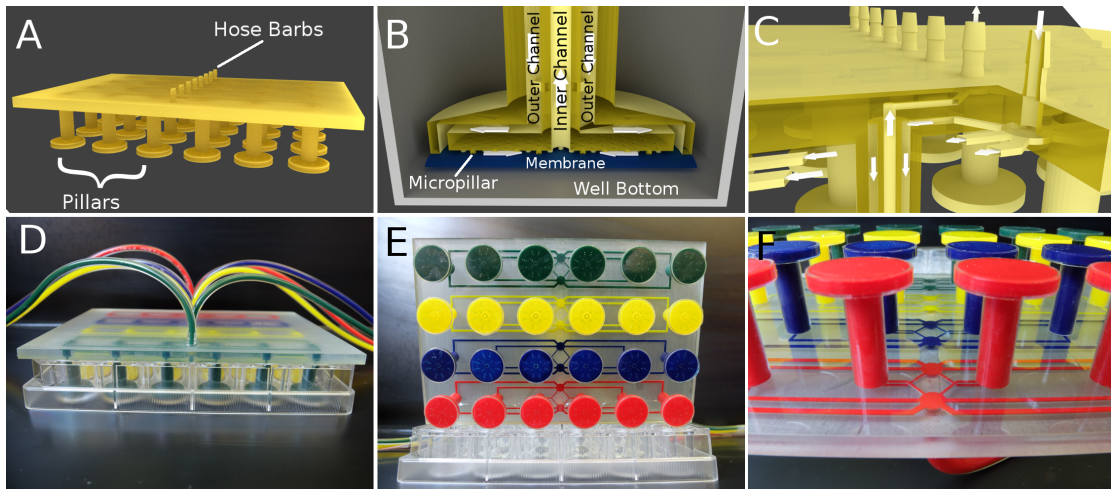
FIGURE 2.2: **Design of 24-well insert device.** (A) Rendering of whole 3D printed part. An inlet and outlet barb allows perfusion of gas to control 6 wells. (B) At the bottom of each pillar gas entering from the outer channel flows along the PDMS membrane (blue), which is supported by micropillars, and exhausts via the inner pipe. Diffusion occurs rapidly through the PDMS membrane to the cell culture spaced 500 μm away at the bottom of the well. (C) Cross-section demonstrating how the microfluidic distribution network and double pipes are connected. The two adjacent mirrored distribution networks are spaced 1 mm apart along the z-axis allowing them to overlap and enter the separate vertical pipes. The arrows indicate the flow direction. The incoming gas enters the outer pipe on its way to the bottom of the well and returns through the inner pipe. (D) Photo of the device with dyed channels in a 24-well plate. (E) Photo of the device from the bottom with four independent channel networks. (F) Photo of the printed distribution networks.

2.1.3 Fabrication of the 3D-printed Part

The fluidic distribution networks were designed in Autocad in 2D and then extruded to 3D with Blender. Because the channel path length to each well varied, the flow resistance in each channel was balanced by adjusting the width. Each distribution network services six pillars that reach into the well of the plate, leaving a 500 μm gap to the culture surface. A pipe within a pipe design was used to allow a forward and return path in each pillar that also created uniform flow across the diffusion membrane. The design was repeated to create four sets that service six wells. Hose barbs were added to each inlet and outlet port. The resulting STL file was printed by fineline prototyping with a Viper SLA system in WaterShed XC, an ABS or PBT-like, proprietary material.

Observations Working with Watershed XC   Fineline Prototyping prefers not to print anything with internal channels smaller than 600 μm square. They cite issues draining the resin from small channels as a limitation.

The material will warp if heated above ∼50 °C. If the insert warps, it ruins the insert's ability to uniformly control oxygen because the pillars do not reach the proper depth in the well. The material will also change from a colorless transparent appearance to a deep amber color if exposed to UV light or window light. It will not change color when exposed only to the florescence lights of the lab or a windowless room.

Dr. Khetani's group attempted to use these devices for controlling oxygen with their co-culture liver model but came to the conclusion that the inset material was inducing a toxic environment. Watershed XC has been reported to cause toxicity in zebrafish embryos[169]. No toxicity effects were noticed in A549 lung cancer cells.

2.1.4   3D-printed Open Well Device.

An other version of an oxygen control device was also produced with 3D printing. It was an open well version inspired by Rexius-Hall *et al.*'s large area open-well devices[170]. It was designed in the format of a 75 mm diameter polystyrene petri dish. A serpentine channel provided one gas condition for the entire plate. A PDMS membrane was attached over the channels with PDMS mortar (Figure 2.3). Integrated hose barbs allowed tubing to be directly connected. This design allowed cells to be seeded directly on the membrane which also facilitated diffusion of the gas environment of interest. This design was not pursued because the limitation of not being able to use inverted microscope imaging systems.

2.1.5   Fabrication and Attachment of Membranes

Gas permeable membranes were made by compressing 10:1 mixed and degassed PDMS between two 6 x 6 x 1/4 inch glass plates that were spaced 100 μm apart with two layers of scotch tape (for detailed protocol, see Appendix B *Molding of Gas Permeable Membranes.*). Compression molding was preferred to spinning on a wafer because the compression molds produced more uniform membranes edge-to-edge, where spinning produced inconsistent thicknesses. Also 6 x 6 inch mold produced a large enough area to cut membranes for an entire 24-well insert. This confirmed membranes were uniform across the insert as they were cut from the same membrane. Molds were baked at 50°C on a hot plate to avoid bubble formation. Mixed PDMS contains dissolved air. When
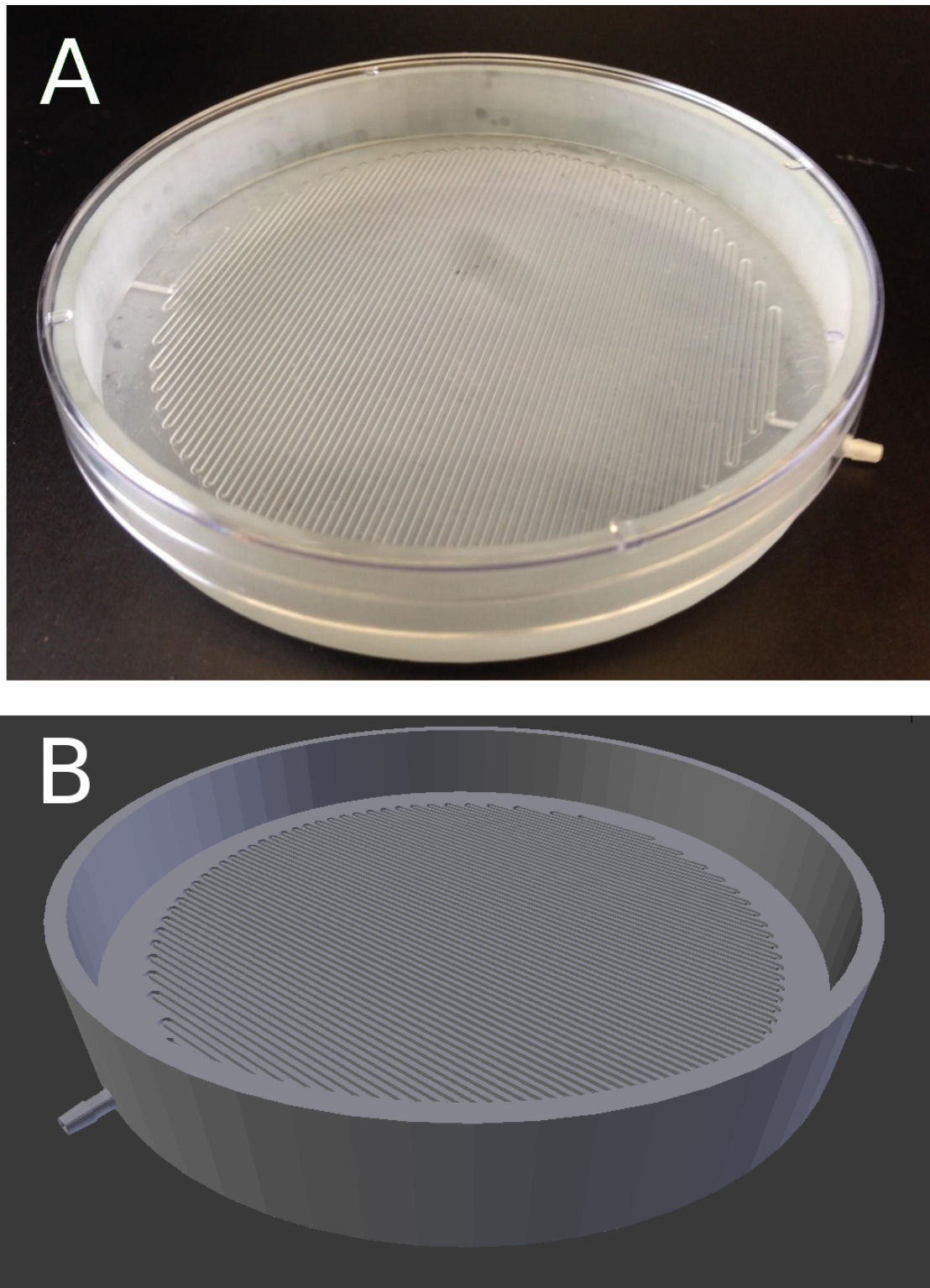
FIGURE 2.3: **An open well 3D-printed oxygen control device.** (B) The 3D part is printed with a 500 μm wide channel following a serpentine path leaving 500 μm of space between each channel. A PDMS membrane is adhered across the channels by spin coating a thin layer of PDMS on the membrane and allowing it to cure in place. (A) The device is designed so that a standard 3" petri dish lid may be used.

PDMS is heated to cure, the air expands. In this mold set-up, the gas is trapped between the two glass plates causing the spontaneous formation of bubbles in the membrane. Membranes were transferred to a transparency and placed over a cutting template and cut to size for the pillar bottoms. To attach the membranes to the 3D printed part, a small amount of PDMS was applied to the membranes and spread thin to act as a mortar. The membranes were left in place to cure overnight as heating of the 3D printed material caused unpredictable warping of the device such that the well pillars did not reach the indented depth uniformly across the 24-well plate. The device was leak tested by placing it in a 24-well plate whose wells were filled with DI water. After 20 minutes any leaks would be apparent as water could be seen in the pillar. Leaky pillars were marked and the device was placed in a vacuum desiccator to evaporate the water from inside the device. The leaky pillars were patched with additional PDMS or had their membranes replaced completely. Alternative membrane materials were briefly explored including PTFE tape (plumbers tape) and 0.2 μm HPLC membranes (FP-Vericel). Both of these membranes were attached with PDMS mortar, as described above, but seemed to be inconsistently permeable to water causing the wells to fill with water.

2.1.6 Flow Set-up

Flow through the device was driven by vacuum with a ventri sink aspirator. Vacuum was used rather than pressure from the tanks to confirm that the flow in each of the 6-well units was uniform. Also, there was concern that pressure may burst the membranes or cause them to detach. This vacuum line was split evenly into four and connected to each outlet. The inlet gas was from pressurized tanks of either 0% O_2, 5% O_2, 10% O_2, or 21% O_2. Each gas tank was also 5% CO_2 for CO_2 buffered medium. Each pressurized tank had a multistage cylinder regulator as well as an in-line IV flow regulator. An open connection was made in the lines leading to the inlets by placing tubing from 3D printed barb into the wide end of a 1000 μL pipette tip. The narrow end of the pipette tip was connected to tubing from the IV flow regulators. Flow from the pressurized tank was set to exceed the flow of the vacuum so that gas was drawn from the tank condition via the open cone connections. A rotameter was modified to measure vacuum by disassembling it and inverting the sight glass orientation. Flow allowed by the IV flowmeter in each of the four inlet lines was measured by temporarily diverting the flow with a three-way stopcock to a floating ball rotameter. This way each flow rate could be measured with

the same rotameter, and could be independently adjusted to the same flow rate. (Figure 2.4).
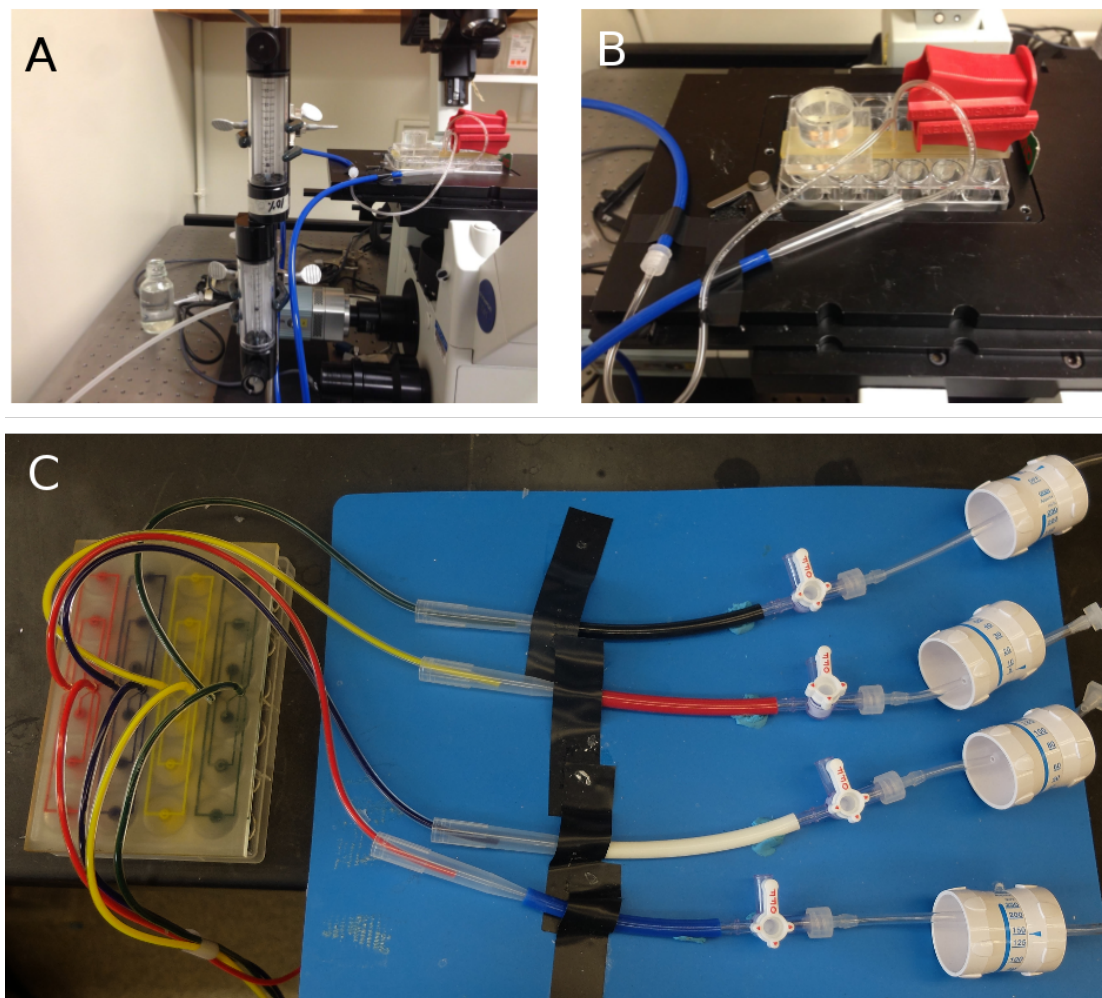
FIGURE 2.4: **Off-device flow set-up.** (A) Vacuum flow rotameter (above, with adjustment knob on the top) and pressurized flow rotameter (below, with the adjustment knob on the bottom) next to the insert on the microscope stage for oxygen characterization testing. Notice the vacuum flow rate is lower than the pressurized flow rate. (B) The open connection is formed with a micropipette tip cone where the gas of insert is drawn into the insert. This was a test insert 6-well unit that had to be prevented from tipping with weights. (C) Set-up for the four condition 24-well plate. One of the two tubing lines from each 6-well unit is connected to a vacuum source which pulls gas through the system. The inlet tubing is loosely placed in the wide end of a 1000 μL pipette tip that acts as a cone. Flow for each gas condition comes from pressurized tanks with tank top regulators (not pictured) to the IV flow rate regulators (right). The three way stopcocks allow the flow to be diverted to a rotameter to measure the flow and adjust it with the IV flow regulator.

2.1.7 Oxygen Characterization

Oxygen Sensors   PtOEPK (Pt(II) octaethylporphine ketone) sensors were created by spinning thin films from a PtOEPK in polystyrene-toluene solution. Thin film sensors were cut and fixed to the bottom of each well of a 24-well with a drop of PDMS as mortar.

Calibration of Oxygen Sensors   An oxygen scavenger solution was made by dissolving Na_2SO_3 in DI water at 2 g/L. Using sodium sulfite (Na_2SO_3) to scavenge all oxygen is the preferred method of making a 0% O_2 liquid to calibrate with. Bubbling of water with 0% O_2 gas or any other gas mixture never seemed to reach the desired level of oxygen in the gas. In an attempt to test this, 50 mL tubes of water were bubbled with 0% O_2 overnight and measured with the FOXY probe (Ocean Optics) calibrated with Na_2SO_3. The oxygen level measured in the bubbled water was never below 5% O_2. The wells were filled with the oxygen scavenger solution and the insert device was placed in the plate. 5% CO_2, balanced N_2 was flowed through the device to flush out any oxygen. The intensity of the PtOEPK sensor was measured via epi-fluorescence imaging (Olympus XI-51). A filter cube with an excitation/emission of 595/760 nm and a 620 nm dichroic mirror was used. When the intensity stabilized, images of all the sensors were taken. A motorized stage and imaging control software (metamorph) was used to memorize positions of all the wells. Each well was imaged sequentially in a 1-6, 12-7, 13-18, 24-19 order to minimize the distance and time the stage had to travel. These intensity values were considered 0% oxygen and taken as the calibration point. The plate was removed from the microscope and the insert was taken out and both the plate and insert were rinsed in DI water to wash away all the scavenger solution. DI water that was equilibrated to room temperature and atmospheric air (by placing in an open container overnight in the microscope room) was used to fill the wells. With the insert placed in the plate and 5% CO_2, balanced N_2 was flowed through the device until the intensity stabilized ($\sim$45 minutes). The 5% CO_2, 5% O_2, balanced N_2 was flowed through the device. When the intensity stabilized, a calibration point was taken that was considered 5% O_2. Next, 5% CO_2, 10% O_2, balanced N_2 was flowed through the device and the 10% calibration point was taken. Finally the water in the plate was replaced again and 5% CO_2, balanced air was flowed through the device.

Timecourse Oxygen Characterization Data Collection   Each well was imaged sequentially at intervals of 5 minutes for a total time of 6 hours. After 15 minutes of 5% CO_2, balanced air (enough time for three time points), the inlets were changed to: row 1: 5% CO_2 balanced N_2; row 2: 5% CO_2, 5% O_2 balanced N_2; row 3: 5% O_2, 10% O_2, balance N_2; row 4: 5% CO_2 balanced air.

2.1.8   Analyzing Intensities

ImageJ was used to organize images according to metadata into folders of wells including specifying calibration points. Then imageJ was used to measure intensity of each image from the time course data which was recorded into a text file for each well (Imagej macros can be found in Appendix C.1 and Appendix C.2). A two-site Stern-Volmer model was used to interpret the intensity data and generate oxygen values (Matlab code can be found in Appendix C.3).

Stern-Volmer Analysis   The intensity values of the PtOEPK sensors were converted to oxygen values according to the Stern-Volmer relationship:

$$\frac{I_0}{I} = 1 + K_{sv} \cdot [Q],\tag{2.2}$$

where I_0 is the intensity of the sensor in absence of oxygen, K_{sv} is the Stern-Volmer constant, and Q is oxygen fraction.

K_{sv} can be solved for using two known calibration points:

$$K_{sv} = \frac{I_0 - I_c}{Q_0 \cdot I_0 - Q_c \cdot I_c},\tag{2.3}$$

where I_0 and Q_0 are the intensity and level of oxygen at one calibration point and I_c and Q_c is the second calibration point.

Two-site Model   Ultimately more accurate oxygen values were calculated using multiple intermediate calibration points. A two-site Stern-Volmer model was used which assumes there are more than one quenching rate constants:

$$\frac{I}{I_0} = \frac{f_1}{1 + K_{sv1} \cdot [Q]} + \frac{f_2}{1 + K_{sv2} \cdot [Q]}, \tag{2.4}$$

where K_{sv_1}, and K_{sv_2} are new quenching rate constants fitted from three or more calibration points and f_1 and f_2 sum to 1.

The plotting of I_0/I *vs.* oxygen, and intensity *vs.* oxygen reveals the difference in between the models (Figure 2.5). The result is that the standard model is less accurate between calibration points. The time course data in Figure 2.5 demonstrates a worst-case scenario where calibration points are taken at 0% and 21% when attempting to measure 10% oxygen.

2.1.9 Cancer Cell Culture

Human lung adenocarcinoma (A549) cells were seeded at 30,000 cells per well in a 24-well plate. Note that Megan Rexius-Hall prepared the cell culture. Cells were cultured in DMEM supplemented with 10% FBS. After reaching $\sim$70% confluency, the 24-well insert was placed in the plate and the gases were perfused through the device in the same scheme as in the oxygen characterization. Each row of six wells experienced either 0%, 5%, 10% or 21% O_2, with 5% CO_2 and balanced nitrogen. The assembly was placed in an incubator at 37 °C for six hours. Tubing was run through an access port in the side of the incubator.

2.1.10 Quantitative PCR

Following six hours of oxygen modulation, the 24-well oxygen control insert was removed and culture media was aspirated. Cells in each well were washed twice with PBS, and 300 μL of a lysis solution consisting of 10 μL of β-mercaptoethanol (Sigma Aldrich) per 1 mL of lysis buffer (PureLink RNA Mini Kit; Invitrogen) was added to each well. The lysate from each well was collected as a sample. RNA was extracted according to the PureLink RNA Mini Kit manufacturer's instructions.

Synthesis of cDNA was performed using the High-Capacity cDNA Reverse Transcription Kit (Applied Biosystems), and quantitative PCR was carried out on ABI PRISM 700O
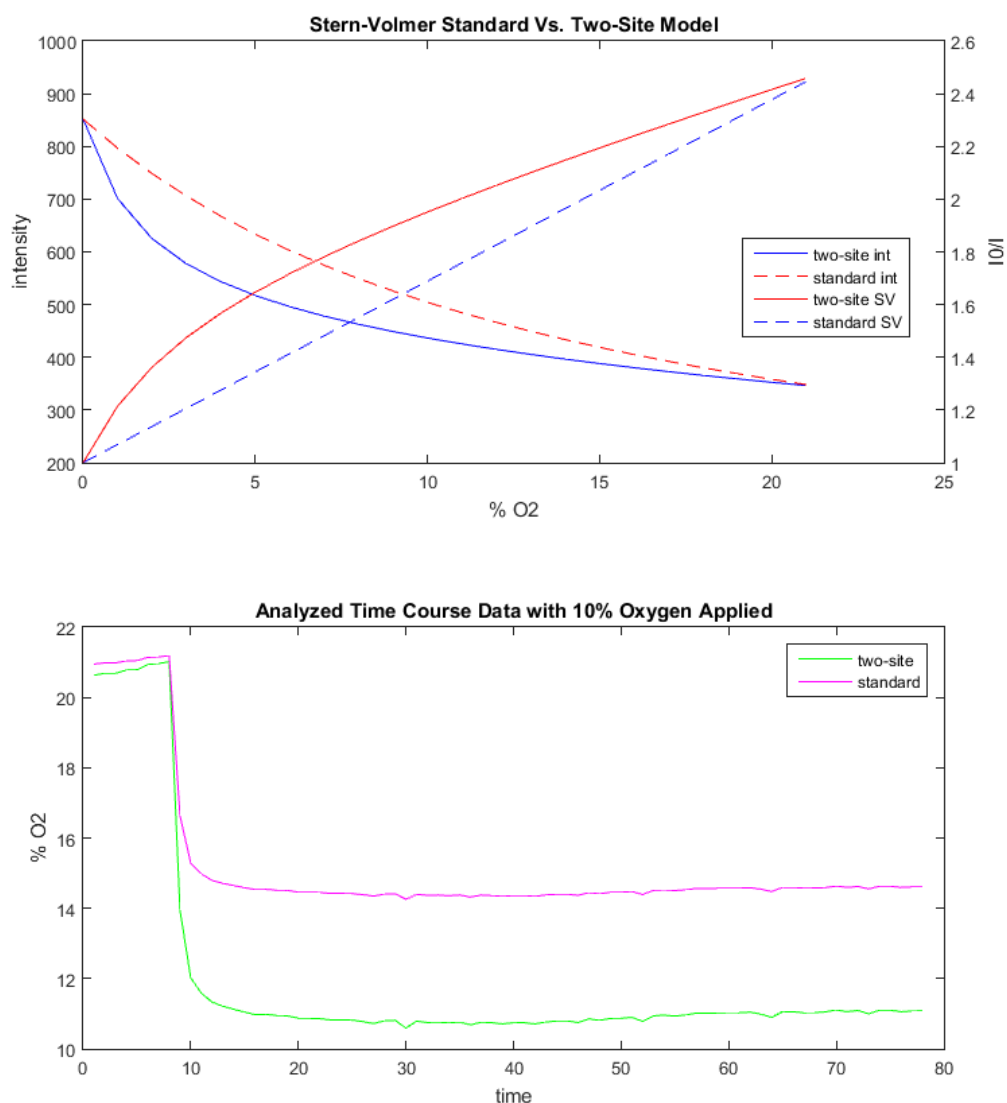
FIGURE 2.5: **Comparison of standard Stern-Volmer with the two-site model.** Time course data analyzed with both methods with the application of 10% oxygen. (below).

(Applied Biosystems) in 25 μL reactions using Taqman Gene Expression Assays. Beta-2-microglobulin (B2M) served as the endogenous control for calculations of relative gene expression. Six technical replicates from the 6-well control unit were processed for each of four oxygen conditions (0%, 5%, 10% and 21% O_2) in three independent experiments. Note that Megan Rexius-Hall performed the PCR protocol.

2.1.11 Statistical Analysis

Cell culture experiments were repeated three independent times. Data are expressed as the mean $\pm$ SD. One-way ANOVA with Tukey's multiple comparison post-test performed by Prism 5 (Graphpad) determined significance. Note that Megan Rexius-Hall performed the PCR analysis.

2.2 3D Printed Adjustable Micropipette

2.2.1 Design and Printing

The design of the pipette was inspired by the operation of a retractable pen. Initial iterations of this design was the work of a UIC Bioengineering Senior Design Team: O. Aboloye, P. Hurtado, R. Romero, and V. Sandoval. As the adviser of the team, I presented them my idea for a 3D-printable micropipette and guided them through design iterations and testing. Initial designs were made in Blender as it's an open source graphics design software. Ultimately two printable parts were designed in 3D CAD software (Solidworks). Fahad Bokhari was recruited to work on the project and arrived with a background of Solidworks, which is a more capable software than Blender for modeling parts. Note that Fahad contributed significantly to the design as well as the majority of CAD modeling.

The pipette is designed to actuate a 1 mL or 3 mL syringe to a user set displacement. The core of the design is two printed parts, the body and the plunger which are able to be printed on a consumer grade FDM printer (Figure 2.6), in this case a Makerbot Replicator. The Makerbot printed the parts in Polylactic acid (PLA) with a 10% infill, and the rafts option on. High resolution printing was preferred with 100 μm step sizes as it produced smoother parts, but standard resolution (100 μm step sizes) produced parts worked with some sanding. A 1 mL or 3 mL syringe twists to lock in the body part and is held into place by the syringe flanges. The 30-300 μL configuration uses a 1 mL pipette and the 100-1000 μL configuration uses a 3 mL pipette. The plunger part slides freely in the body part and actuates the syringe by pushing the thumb button (Figure 2.7). The pipette is spring loaded towards a set point which is adjustable by a set-screw. When the thumb button is pressed, the system locks when it reaches the
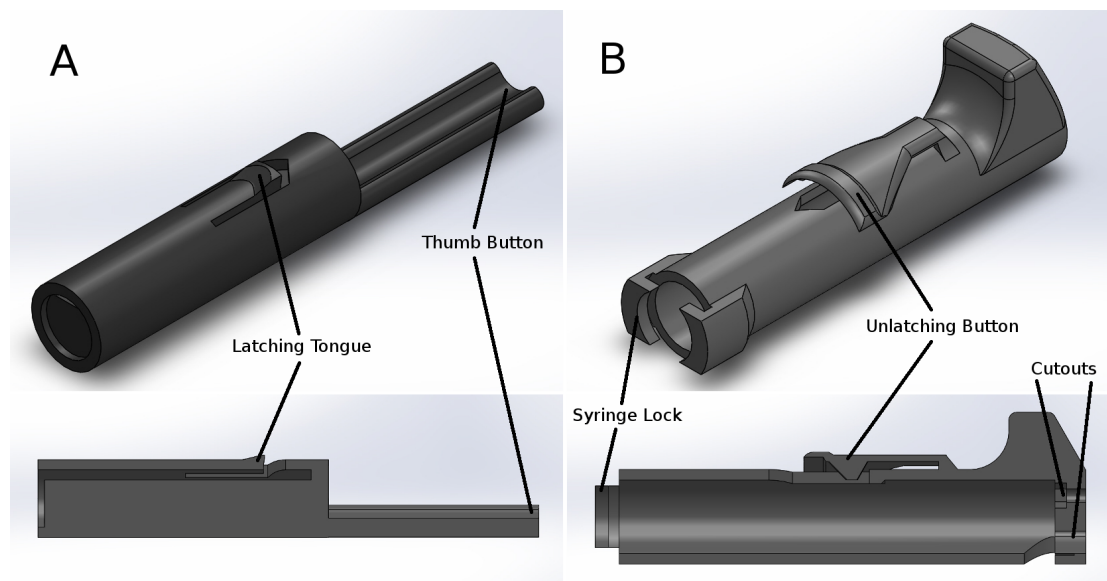
FIGURE 2.6: **CAD renderings of printable parts and cross-sections.** (A) The printed plunger part is a shaft that pushes on the syringe plunger and slides in the printed body part. The printed plunger has a latching tongue and button which interfaces with the printed body part. (B) The printed body part holds the syringe and interfaces with the printed plunger part. The body part features the unlatching button and slots to hold the syringe in place by its flanges. The body part also has two cutouts in the top for the plunger button and for the hex nut and bolt. Note that Fahad Bokhari prepared renderings of the CAD parts for this figure.

latched position where it is ready to draw in fluid. The plunger is held in place with a latching button design, which is released with the unlatching button drawing in fluid. The latching works by the design of a thin wall that is supported by a small area, effectively creating a fulcrum from the flexing of the plastic. The displacement is equal to the distance between the set position and the latched position. The pipette can also be pressed past the latched position to "blow-out" the transferred fluid completely from the pipette tip. Our printed pipette mimics commercial pipettes design, function, and user operation, making it intuitive to use.

2.2.2 Adjustment of Graduations

Our pipette uses the air-displacement method, where a vacuum is applied to a pocket of air to draw liquid into the pipette. As air is an compressible fluid, this pocket of air grows due to the weight of the liquid pulling on it. Due to this effect, the graduations on the syringe are not accurate, as they are designed for measuring liquid within the syringe. At larger volumes this effect is more pronounced, resulting in the volume measured being greater than the amount of liquid pulled into the syringe. This was remedied by creating
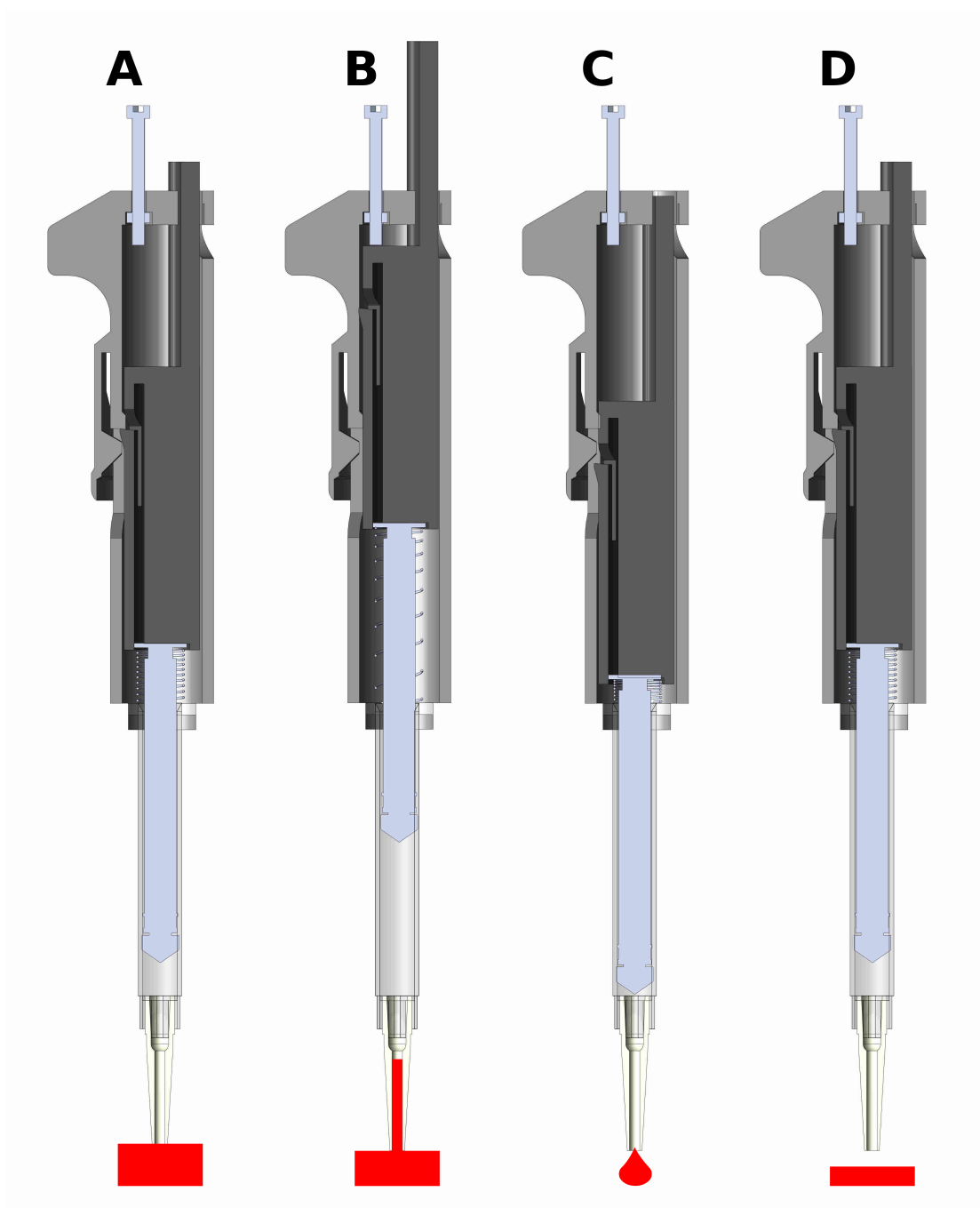
FIGURE 2.7: **CAD renderings of assembled pipette and function.** The pipette actuates the syringe to three positions. **(A) The latched position.** When the plunger is pressed the pipette locks at this position. The tip is then placed in a liquid and the unlatching button is pressed to release the pipette back to the set position (B), drawing in liquid. **(B) The set position.** The position of the screw determines the total displacement that the plunger moves. The pipette is spring loaded to return to this position. **(C) The blow-out position.** The fluid is transferred by pressing the plunger past the latched position to blow-out all the liquid. **(D) Return to the latched position.** The pipette returns to the latched position ready to perform another transfer. Note that Fahad Bokhari prepared renderings of the pipette for this figure.

a new scale to account for the expansion. The scale is printed on a transparency sheet and is taped onto the syringe for accurate measurements (see Appendix B). Note that Fahad Bokhari designed the new graduation scales.

2.2.3 Additional Parts

Additional materials required for assembly include two springs, a nut and bolt. Attempts to make a printable luer lock adapter for tips were abandoned as the surface of printed parts is too rough to make an air tight seal with the luer or pipette tip. Instead, a combination of a barbed luer adapter and elastic tubing is used to attach the pipette tips.

TABLE 2.1: Parts and cost for the 30-300 μL pipette.

30-300 mL Configuration:	Source	Unit Price	Part Number
Filament	Makerbot	$1.63	NA
1 mL Syringe	BD Biosciences	$0.15	309628
M3 Bolt, 35 mm	McMaster-Carr	$0.12	91287A026
M3 Nut	McMaster-Carr	$0.01	90591A121
Music Wire Compression Springs* (2)	Jones Spring Co	$1.23	C10-022-048
Female Luer to 1/8" Hose Barb Adapter	Cole-Parmer	$0.40	EW-30800-08
Tygon Tubing, 1/16"ID x 3/16"OD	Cole-Parmer	$0.03	EW-06407-72
300 uL Tips (10)	Fisher Scientific	$0.34	02-707-447
	Total	$3.91	

TABLE 2.2: Parts and cost for the 100-1000 μL pipette.

100-1000 mL configuration:	Source	Unit Price	Part Number
Filament	Makerbot	$1.63	NA
3 mL Syringe	BD Biosciences	$0.73	309657
M3 Bolt, 35 mm	McMaster-Carr	$0.12	91287A026
M3 Nut	McMaster-Carr	$0.01	90591A121
Music Wire Compression Springs* (2)	Jones Spring Co	$1.23	C10-022-048
Female luer to 5/32" Hose Barb Adapter	Cole-Parmer	$0.66	EW-45508-06
Tygon Tubing, 1/8"ID x 1/4"OD	Cole-Parmer	$0.05	EW-06407-76
1000 uL Tips (10)	Fisher Scientific	$0.41	02-707-400
	Total	$4.84	

*Spring Specifications: Overall length 38 mm, OD 7.62 mm, wire diameter 0.56 mm, Max load 0.86 kg, with closed and flat ends. Also available from McMaster-Carr P/N: 9657K347.

FIGURE 2.8: **Photos of assembled pipettes.** (A) Two assemblies of the pipette: the 100-1000 μL configuration (above) and the 30-300 μL configuration (below). (B) Close-up photo of the taped on scale for each of the syringes.

2.2.4 Assembly

A small amount of paraffin wax is applied to the screw to prevent slop from causing the set point to drift after each actuation. The nut is sunk into the hex inset in the printed body part. The bolt is threaded in from the top of the body into the nut. Springs are threaded onto the plunger of a 1 mL syringe for the 30-300 μL configuration. Springs are placed inside a 3 mL syringe for the 100-1000 μL configuration. The plunger part is inserted in the body and the syringe assembly is pushed in and locked from the syringe flanges to the body part to complete assembly(Figure 2.6). Parts and cost are listed in Table 2.1 and 2.2.

2.2.5 Validation

The printed pipette's accuracy and precision was characterized and compared to a commercial pipette as well as ISO 8655. The printed pipette was adjusted to the target volume by eye from the syringe graduations. Deionized water was transferred and measured with a scale. Five transfers were recorded and averaged to account for random variability. Data was taken for printed pipettes with existing syringe graduations as well as with the our adjusted scale. Data was taken with commercial pipettes of 30-300 μL and 100-1000 μL to compare to the printed pipette. Note that Fahad Bokhari helped collect data. Accuracy and precision are expressed as systematic error and random error, respectively, and are calculated according to ISO 8655 [126] (Table 3.1 and 3.2). The systematic error, or accuracy, is calculated according to the following equations where accuracy (A) is the difference of the mean volume ($\bar{V}$) and the nominal volume (V_o):

$$A = \bar{V} - V_o, A\% = 100\% \times A/V_o \tag{2.5}$$

The precision or random error is the standard deviation (s) of the measurements and (CV) is the coefficient of variation:

$$s = \sqrt{\frac{\sum_{i=1}^{n}(V_i - \bar{V})^2}{n-1}}, CV = 100\% \times s/\bar{V} \tag{2.6}$$

2.3 Droplet Encapsulation of *S. pneumoniae*

2.3.1 *S. pneumoniae* Strains

Two strains of *S. pneumoniae* were produced by Dr. Morrison of the Biological Sciences Department at UIC: CP2204 and CP2215. The strains were made to be complementary in antibiotic resistances to aid in assaying transformation events. The CP2204 strain has inducible competence so it is the designated recipient. CP2215 cannot become competent so it is the natural donor of DNA. Traits of these strains are listed in table 2.3

TABLE 2.3: Summary of phenotypes of strains used for transformation studies.

Strain	Competence	Rifampin	Spectinomycin	Novobiocin	Label
CP2204	CSP inducible	Resistant	Sensitive	Sensitive	RFP
CP2215	non-competent	Sensitive	Resistant	Resistant	GFP

2.3.2 Culturing

S. pneumoniae strains CP2204 and CP2215 were grown separately in 12 mL of chemically defined medium (CDM) with 1% casein tryptone (CAT) medium at 37°C to the desired OD (media formulas can be found in Appendix A). When the desired OD was reached suspended cultures were spun down at 8000 RCF for 8 minutes in a 4°C centrifuge. The supernatant was poured off and the cultures were re-suspended in M9 or a ratio of up to 20% CDM in M9 medium depending on the application and held at 4°C.

Observations Culturing CP2204 and CP2215   CP2215 Grows quickly after seeding in CDM whereas CP2204 has a lag phase before it eventually grows at log rates. Typically 15 μL of CP2215 and 200 μL of CP2204 (both strains were from frozen stocks of OD 4.0) were added to individual 12 mL tubes of CDM and incubated in a 37°C water bath. After about 4 hours of growth, they both met around an OD of 0.2. With an OD of less than 0.2 it was hard to see the cell pellet with CP2215 after spinning. Also, 12 mL of OD 0.2 cells yielded enough to spin down and resuspend at higher ODs for droplet encapsulation experiments.

2.3.3 Inducing Transformation

Strain CP2204 was made competent with an inducer cocktail containing CSP, BSA, and CaCl$_2$ (The specific formula can be found in Apendeix A Table A.3). The inducer cocktail is introduced to the chilled mixture of CP2204 and CP2215. The cells can be held in at 4°C in the presence of the inducer cocktail and will remain inactivated. This suspension is then brought up to 37°C to initiate cell-cell attack and transformation. Typically these reaction suspensions are transferred to a cryogenic vials and placed in a heater block at 37°C for 30 minutes. After 30 minutes suspension are diluted tenfold into CAT media and incubated at 37°C for an hour. This step dilutes the inducer inactivating it and the hour incubation allows a generation of recombinants to emerge (for detailed protocol, see Appendix B *Cell-cell Attack and Gene Transfer*).

2.3.4 Plating and Selecting for Drug Resistance

Suspensions were diluted in more CAT media for anticipated survivor counts. Typically suspensions were diluted by 100,000 for single drug agar, 100 for two drug agar, and 10 for triple drug agar. Agar was made from either CAT medium or Todd-Hewitt broth with 2% yeast extract (THY) medium by adding 4.5 g of agar per 300 mL of medium and autoclaving. 50 mm plates are filled with the following layers in order:

1. 3 mL Agar

2. 1.5 mL Agar + 75 μm to 1.5 mL cell suspension quickly mixed

3. 3 mL Agar

4. 3 mL drug agar

Layers are added at least a few minutes apart to allow them to set before the next layer is added. Plates are incubated at in a 37°C room for 48 hours before counting. Plates are incubated upside down to slow the diffusion of drug to the cell layer. Concentrations in the drug layer are listed in Appendix A Table A.4.

2.4 Droplet Generation and Cell Encapsulation

A microfluidic droplet generating device was used to encapsulate cells during transformation. A flow focusing device with two aqueous inlets was used to keep the cells and inducer separate until right before droplet generation. Downstream is a droplet incubation and observation chamber. The height of the channels are 10 μm to confine the droplets to a single plane. Pillars were spaced within the incubation chamber to prevent the chamber from collapsing during bonding or expanding while pressurized. In-line filters were placed at the inlets to prevent any debris from flowing downstream and blocking the narrow droplet generating neck. The largest incubation chamber had a volume of ~6.5 μL and was designed to take up the most possible area under a 50 mm x 22 mm coverslip. The dimensions of the droplet generating region were designed to produce 10 μm droplets (Figure 2.9).
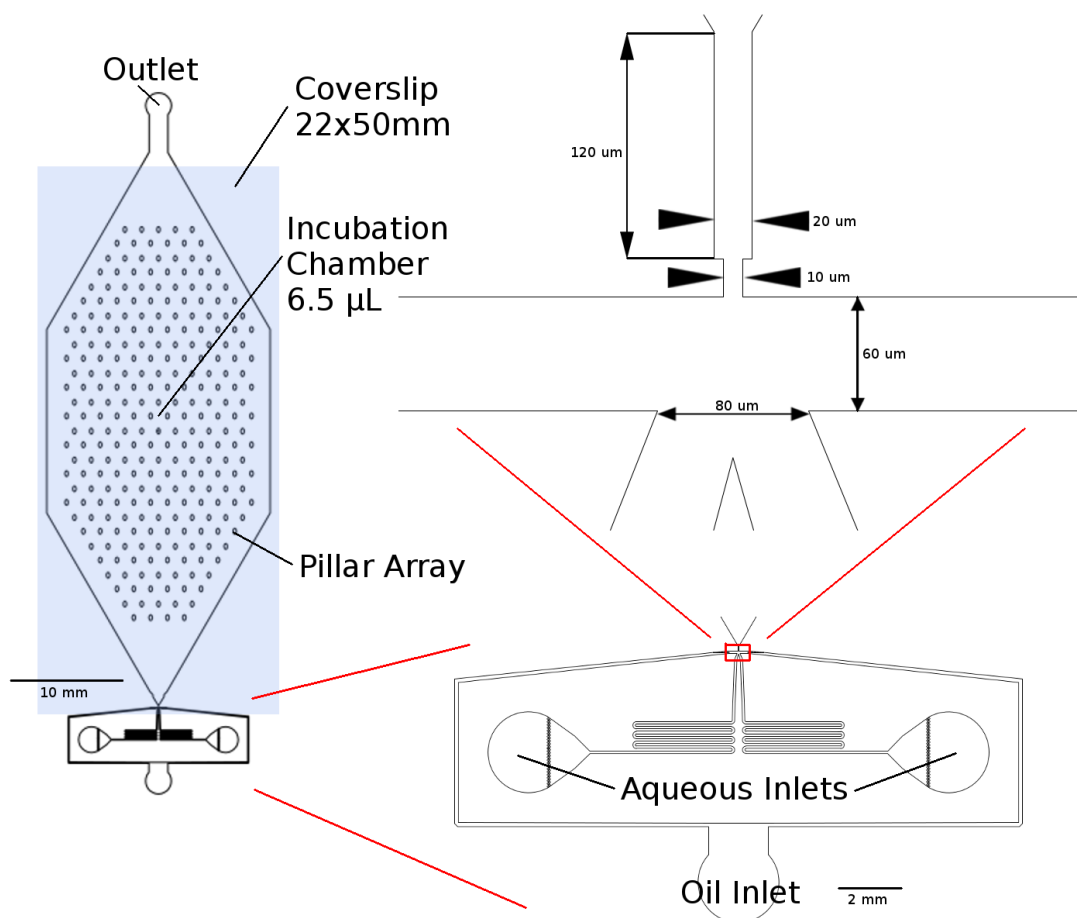
FIGURE 2.9: **Design of droplet generating chip.** The chip has two three inlets for the droplet generator. As the droplets are formed, they fill the incubation chamber. The narrowest part of the neck is 10 μm in width.

2.4.1 Fabrication of Droplet Generating Device

Master Mold Fabrication. A 2D design was made in AutoCad and exported as a DFX format. Small features such as the filter arrays were saved in a separate file and then subtracted via boolean operation in LinkCAD software. SU-8 2015 (MicroChem Corp.) was spun at 4250 RPM on a 100 mm silicon wafer to a thickness of 15 μm. The wafer was baked at 95°C for 10 minutes shielded from light. The wafer was loaded into the μPG 101 (Heilderberg Instruments). The converted file from LinkCAD was imported into the μPG 101 software. The wafer was exposed at 18 mW, 100% intensity and 4x exposure time. After exposure, the wafer was baked at 95°C for 10 minutes and then at 120°C for 30 minutes. I found that this additional bake at 120°C prevented de-lamination that is typical for SU-8 heights less than 50 μm. The uncured SU-8 was then washed away with SU-8 developer (MicroChem Corp.) on a shaker for 30 minutes.
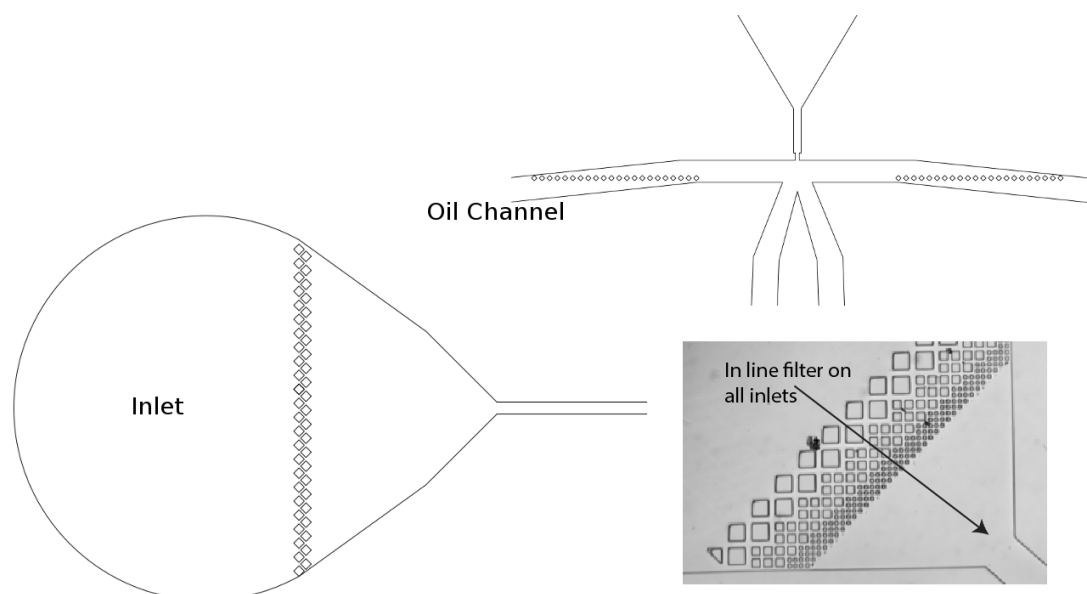
FIGURE 2.10: **In-line filters on droplet generating chip.** In-line filters were used to catch debris.

The wafer was then rinsed with acetone followed by IPA and blown dry with nitrogen (see Appendix B *Quick Protocol Overview*).

Casting of the PDMS Mold   About 30 grams of 10:1 base to curing-agent, PDMS (Slygard 184, Dow Corning) was mixed with a Thinky mixer for 2 minutes. About 10 grams of mixed PDMS was poured onto the master mold and spun at 2000 RPM. A 22 x 50 mm glass cover slip was laid on the uncured PDMS. The mold was placed in a vacuum desiccator (with the strong vacuum) to pull air bubbles from under the cover slip. The cover slip was then manually adjusted to be over the incubation chamber of the design and baked at 65°C to set in place. The wafer is transferred to a sheet of aluminum foil and walls are made around the wafer by wrapping and folding the foil at the edges. The remaining PDMS, ∼20 grams, is poured on the mold and degassed (in the weaker vacuum). The mold is then baked at 65°C for 2 hours. Baking at 85°C is faster but is causes the PDMS to shrink more relative to the coverslip, resulting in unnecessary bowing of PDMS/coverslip mold which makes bonding difficult. Curing at a lower temperature or at RT would decrease this effect, but PDMS cured at lower temperatures is more sticky and elastic, making it more difficult to release from the mold and to punch uniform inlet/outlet holes without splitting. RT curing also requires you to wait overnight to cure.

Releasing the PDMS/coverslip Mold   The PDMS is carefully peeled from the mold containing the embedded coverslip. First, the aluminum foil is removed from around the PDMS/wafer mold. The PDMS is released from the wafer starting by running a razor around the perimeter of the wafer between the PDMS and wafer. The PDMS is peeled to the edge of the coverslip on all sides. Attempting to simply peel the rest of the PDMS/coverslip mold away will result in un-embedding of the coverslip, ruining the mold. To peel the PDMS/coverslip mold successfully, a razor blade or scalpel is used to pry under the coverslip, starting from a corner on the outlet port side of the design, as it is further away from critical channels. Once one corner of the coverslip is released, the rest of the coverslip/PDMS mold should peel easily. If the PDMS tends to stick to the SU-8 rather than peeling with the coverslip silization of the SU-8 mold should be done.

Bonding and Hydrophobic Surface Treatment   The PMDS is cut to size and holes are punched with a 1 mm biopsy punch. PDMS is placed in contact with a glass slide after 45 seconds of oxygen plasma exposure (Plasma Etch, Inc.) to permanently bond. The completed chip is then baked at 135°C for at least 1 hour to strengthen plasma bonding. The chip is removed from the hot plate and allowed to cool before treating with hydrophobic coating. Novec 1720 (3M) is flowed through the device and left to stand for 10 minutes. The Novec is then flushed from the chip with air and returned to a 135°C hot plate to bake in the coating and sterilize the chip for at least 30 minutes. Note that Fahad Bokhari helped with fabrication of molds and devices.

2.4.2   Iterations of the Incubation Designs

Arrays of crab claw shaped elements were designed to trap individual droplets (Figure 2.13). When the trap and droplet sizes were tuned, the traps effectively held droplets with flowing oil. Unfortunately, droplets evaporated and eventually slipped through the traps when they were small enough. These designs were tested with water-in-oil droplets in devices without the coverslip evaporation shield. The flow of oil required to keep the droplets trapped will likely still cause evaporation regardless of the coverslip shield but this has not been tested.
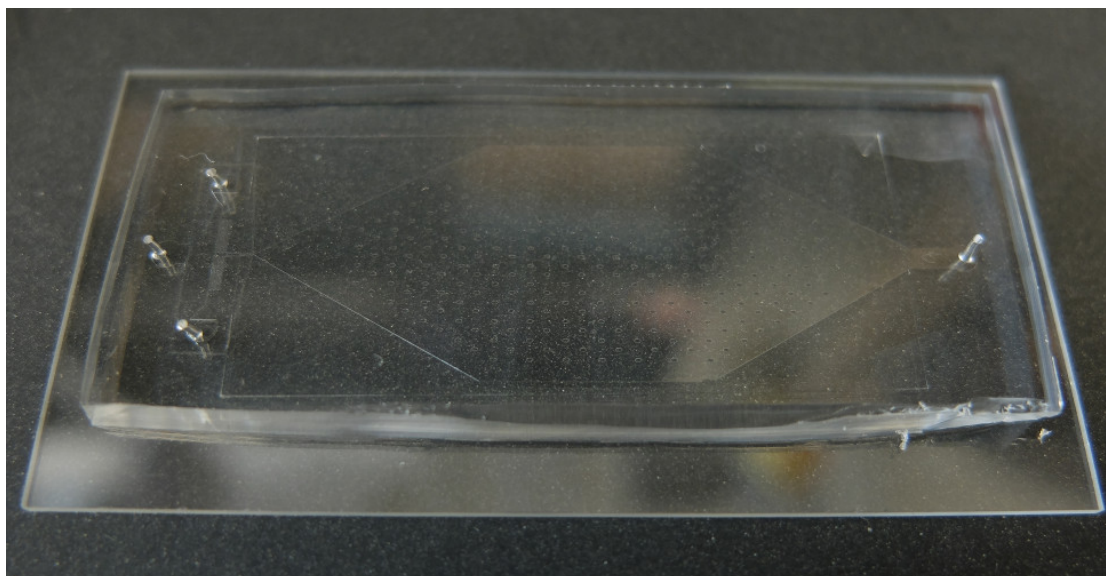
FIGURE 2.11: **Photo of completed droplet generation and incubation chip.** The PDMS/coverslip mold is bonded to a glass slide. This design has a 6.5 μL incubation chamber as described in Figure 2.9.
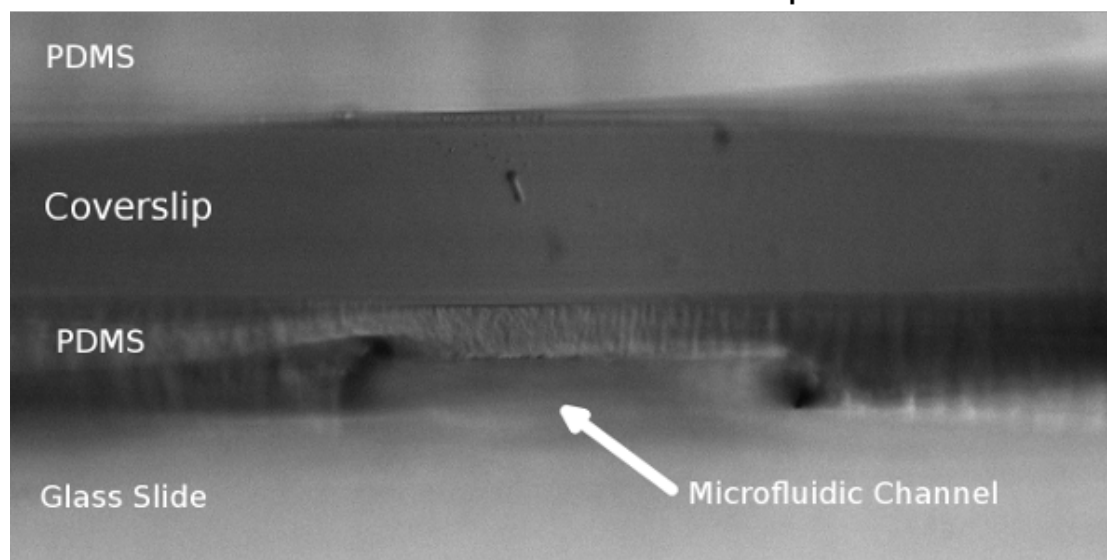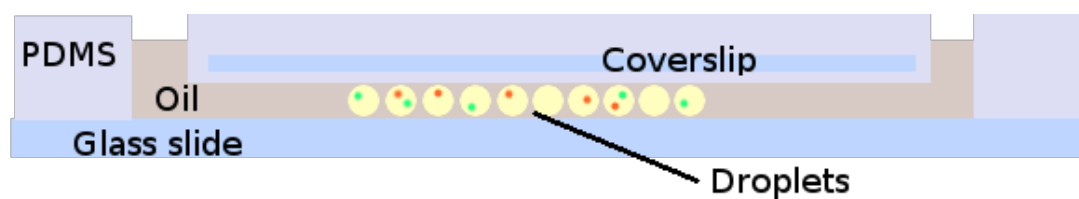
FIGURE 2.12: **Cross section design of device to prevent evaporation.** The incubation chamber is sandwiched between two layers of glass to prevent evaporation. Schematic of the design (above). A micrograph of a device cut in half (below).

Due to the evaporation, trapping was abandoned and close packed droplets were preferred, as they were self-insulating from evaporation. A new problem arose in that the droplets did not remain stationary in the chamber when the pumps were turned off. A

few designs incorporating valves were attempted but were too tedious to use. Eventually the solution that was used was to pull the tubing from the device, after the incubation chamber was full of droplets, which effectively halted the flow.
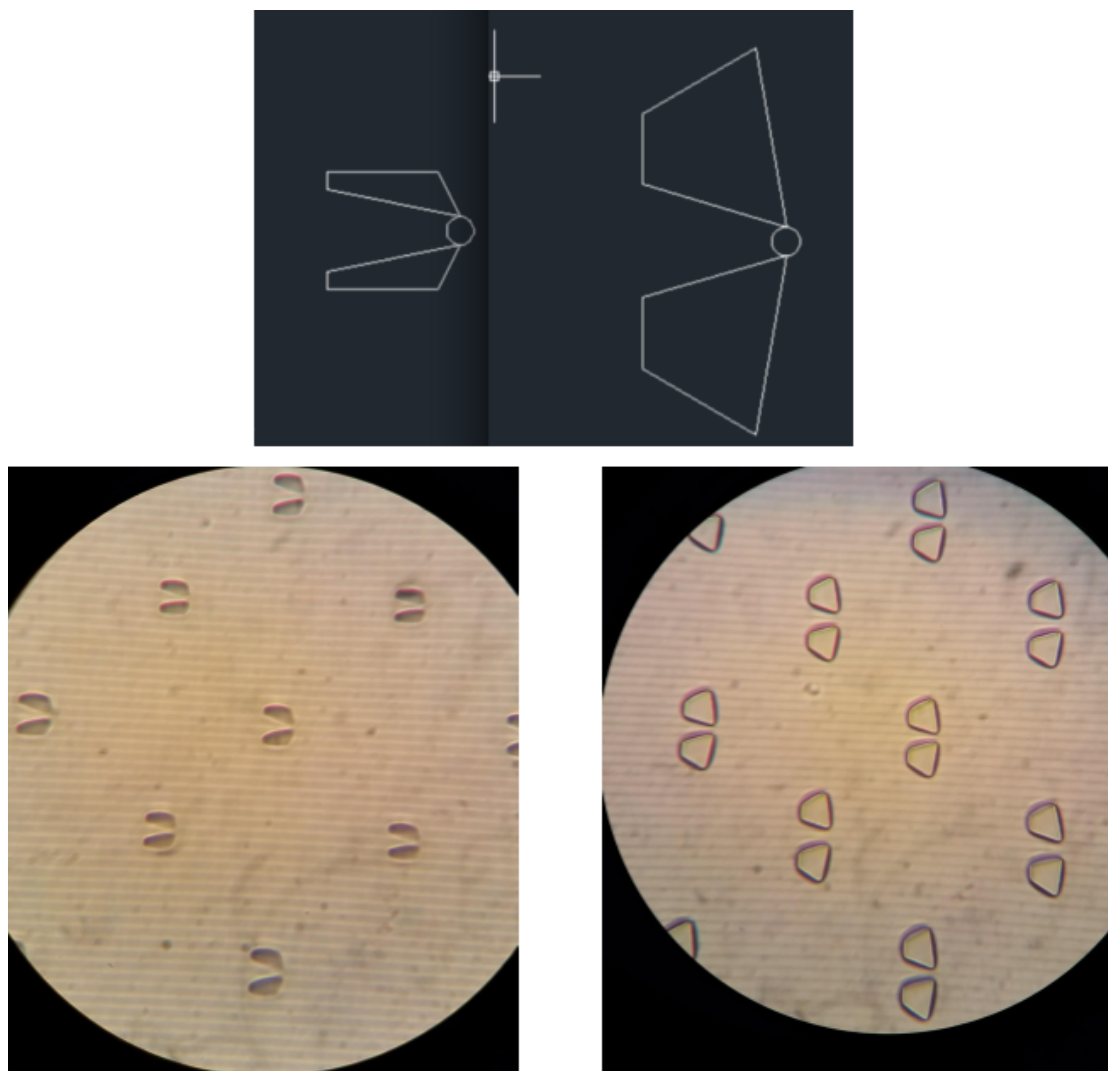
FIGURE 2.13: **Crab claw droplet traps.** An array of droplet traps were used to trap droplets individual droplets. The traps had a 5 μm opening at the back indicated by the circle in the CAD (above). Micrograph of the array in the incubation chamber (below).

2.4.3 Droplet Encapsulation of Cells

The droplet generation chip uses a flow focusing design to make water-in-oil droplets (w/o). The oil and aqueous channels converge at a narrow neck where the aqueous-oil interface is focused, causing droplets to pinch off in a size determined by the neck width (Figure 2.9). FC-40 oil with 2% (v/v) surfactant (Pico-Surf 1, Dolomite) is the continuous phase. FC-40 is a fluorinated oil that is preferred for biological applications.

It has a low viscosity and is denser than water. For testing, water with 1 μm fluorescent beads was used for the dispersed phase. For transformation studies, cells suspended in M9 media and inducer is used. The droplet encapsulation procedure is performed in a cold room to keep the cells inactivated until the desired amount of emulsion is produced(Figure 2.14). Depending on the experiment and chip design, emulsion may be stored off-chip in tubing or can be incubated on-chip in the incubation chamber (for detailed protocol, see Appendix B *Cell-cell Attack and Transformation in Droplets*). Flow is driven with two syringe pumps, one for the oil syringe and one that drives both aqueous syringes. 1 mL syringes (BD Biosciences) with blunted 21 gauge hypodermic needles and PTFE tubing was used. With the syringe and tubing primed, the tubing is inserted into the inlet ports. The aqueous pump is started first at a flow rate of 50 μL/h. The droplet generating chip is observed through a bench-top microscope(Figure 2.14). When the aqueous channels begin making progress towards the droplet generating neck, the pump with the oil syringe is started at 90 μL/h. As the flows equilibrate droplets should begin forming. The aqueous flow rate can then be reduced to 15 μL/h for the remainder of droplet formation. Droplet formation can continue until the hydrophobic surface becomes fouled or debris block the neck. It takes $\sim$1 hour to allow the device to equilibrate and fill the 6.5 μL incubation chamber with droplets.

2.4.4 Emulsion Breaking

After the transformation incubation step for 37°C for 30 minutes, the chip is returned to the cold room to push the droplets out of the incubation chamber. Oil is pumped into the oil inlet, and the aquous inlets are connected to each other with a short length of tubing which diverts all flow into the incubation chamber. It takes $\sim$1 hour to push all the droplet out of the 6.5 μL incubation chamber. The cells can then be released from the droplets into a bulk suspension for further dilution and plating. Emulsion breaking was done at room temperature.

1. After transferring the emulsion to a micro centrifuge tube, 200 μL CAT medium was added

2. The tube was spun down at 100 RCF for 30 s

3. The separated oil was pipetted out from the bottom.

FIGURE 2.14: **Encapsulation of cells was performed in a 4°C room with a benchtop inverted microscope.**

4. 400 μL of de-emulsifying agent (Pico-Break, Dolomite) was added.

5. The tube was spun down again for at 1000 RCF for 1 minute.

6. Finally, the cells suspended in media are pipetted off the top of the de-emulsifying agent.

The amount of media volume in emulsion is estimated based on the packing efficiency of spheres in a sheet. The highest volume ratio of droplets is ~70%. The volume of holding chamber is 6.5 μL, so when the holding chamber is fully packed, the volume of aqueous phase is 4.5 μL. The volume of suspension that is recovered is assumed to be ~4 μL. The recovered suspension is brought up to 400 μL which is considered to be diluted by 100-fold.

2.4.5   Imaging of Cells in Droplets

Imaging was first attempted on our epifluorescence scope (Scoppegard, Olympus x51 with RFP, and GFP filter sets and LED X-cite light source). Droplets and cells were visible in bright-field and phase contrast but were very difficult to image with fluorescence. Only a very weak RFP signal could ever be detected from cells that were not moving and no GFP signal was detected. More powerful imaging was sought at the UIC RRC.

Laser Scanning Microscope   Encapsulated cells were stored on ice while transported to the UIC Research Resource Center (RRC) core imaging facility. They were stored in the incubation chamber or in PTFE tubing. Droplets were either directly imaged through the device or transferred to a coverslip bottom plate for imaging with oil immersion objectives. Imaging was performed with a laser scanning microscope (Zeiss 510 Meta) in phase contrast, RFP and GFP modes. During imaging, the temperature control system was used to warm the samples to 37°C. Note that imaging was performed in the UIC Research Resource Center core imaging facility with the help of Megan Rexius-Hall.

2.4.6   FTIR Imaging of DNA and *E. coli* Lysis

In a side project, Fourier transform infrared spectroscopy (FTIR) imaging was used to verify DNA release from lysis of cells. First, a DNA FTIR signature was needed to be selected. DNA needed to be suspended in deuterium oxide (D_2O) rather than a H_2O based solution because of overlap of H_2O DNA FTIR signals.

Resuspending DNA in D_2O   50,000 base pair double stranded Lamba DNA (New England Biolabs) was crash precipitated out of solution and resuspended in D_2O. Two volumes of ethanol was added to the DNA in Tris buffer and chilled to precipitate the DNA. This solution was spun down and the liquid was poured off. The DNA was resuspended in 70% ethanol in D_2O and spun down again. The solution was poured off and remaining liquid was allowed to dry from the tube. Finally the DNA was resuspended in 100% D_2O.

Training *E. coli* to Grow in D$_2$O   *E. coli* strain DH5α was progressively acclimated to growth in M9. M9 minimal media was prepared in 100% D$_2$O supplemented with thiamine as well as in three other ratios of 10%, 50%, and 70% D$_2$O with the remainder H$_2$O. First, culture was started in 10% D$_2$O. Then cells were successively resuspended in, 50%, 70% and finally 100% D$_2$O. Note that culturing of *E. coli* was done by Monpichar Srisa-Art.

FTIR Imaging of *E. coli* and DNA in Droplets   Cells at a density of 8 x 10^7, grown in 100% D$_2$O, were encapsulated with the droplet generating device as described above. Droplets were then flowed from the device in to a calcium fluoride (CaF$_2$) microfluidic chip for imaging. The CaF$_2$ chip was required because both PDMS and glass block the IR spectrum. In the second part of the experiment, lysis buffer (lysozyme 10 mg/ml in: Tris HCl, pH 8.0, with 0.1 M NaCl, 1 mM EDTA, and 5% [w/v] TRITON X-100) was encapsulated with the cells. Imaging was performed on a microscope with a 2D FTIR array (Bruker hyperion 3000). Note that FTIR imaging was performed with the help of Michael Barich in Dr. Amber Krummel's lab at Colorado State University.

Chapter 3

Results

(Previously published as Martin D Brennan, Megan L Rexius-Hall, and David T Eddington. A 3D-Printed Oxygen Control Insert for a 24-Well Plate. Plos One, 10(9):e0137631, 2015. ISSN 1932-6203., Martin Brennan, Fahad Bokhari, and David Eddington. Open Design 3D-Printable Adjustable Micropipette that meets ISO Standard for Accuracy. bioRxiv, 2017. Permissions statements are included in Appendix D.)

3.1 Oxygen Control Insert

3.1.1 Oxygen Control

Standard *vs.* Two-site Stern-Volmer Analysis   Oxygen sensor intensity data was analyzed with both standard Stern-Volmer with only 0% and 21% calibration points and also with a two-site model with 5 intermediate calibration points (Figure 3.1). The oxygen levels that were measured were 0%, 5%, 10% and 21%. The standard Stern-Volmer analysis dramatically skews values in between the calibration points. The two-site model allows accurate measurements anywhere within the range of calibration points.

Final Insert Oxygen Characterization   Oxygen control in the 24-well insert device was quantified with a platinum-based (PtOEPK) planar oxygen sensor placed at the bottom of the well, as shown in Fig. 3.2. The device reaches steady state in 30

minutes and can then hold the oxygen level near 0% O_2 indefinitely, while 95% N_2, 5% CO_2 is pumped through the device. A different gas condition can be used in each separate iteration of the 6-well unit allowing 6 technical replicates of up to 4 different gas conditions in one 24-well plate (Fig. 3.2). There was little variation in the oxygen levels measured in each of the 6 wells controlled by a single inlet, demonstrating the distribution network worked effectively.

3.1.2 Bioverifcation of Oxygen Control

Oxygen levels of 21%, 10%, 5%, and 0% were applied to each set of 6 wells in which A549 cells were cultured. Measurement of relative gene expression confirmed biological responsiveness of cells under the device's control. The device's ability to control the gas environment was demonstrated with hypoxia-induced upregulation of VEGFA mRNA in the A549 cells (Fig. 3.3). Quantitative PCR showed a significant increase in the relative gene expression of VEGFA in wells exposed to 0% O_2 for 6 hours as compared to 21% O_2. Hypoxia-induced alterations in gene expression usually indicate a HIF-transduced hypoxic signal in cells. When a HIF transcription factor undergoes nuclear translocation, it can initiate transcription of genes by binding to the hypoxia response element (HRE)[171] on its target genes. VEGFA has previously been shown to have a functional HRE, and upregulation has been observed in A549 cells under hypoxic conditions[172].

3.2 3D-printable Pipette

3.2.1 Accuracy and Precision Validation

Using the adjusted syringe graduation scale, our printed pipette meets ISO 8655 standards, but using the existing syringe graduation scale does not meet the ISO standard for accuracy. According to ISO 8655 for a pipette with the maximum nominal volume of 1000 μL the systematic error cannot exceed 8 μL and the random error cannot exceed 3 μL [126]. For the maximum nominal volume of 300 μL the systemic error cannot exceed 4 μL and the random error cannot exceed 1.5 μL. The commercial pipettes met these standards handily, but in our initial tests with our printed pipette we noticed large

negative systematic error suggesting that we were missing a biasing factor. This error was exaggerated while transferring larger volumes (fig. 3.4, and fig. 3.5). After further investigation we realized that the water in the tip pulls on the air due to gravity which causes the air to expand slightly, but enough to make measuring with the graduations inaccurate. The graduations are intended to measure incompressible fluids within the syringe while we were using them to measure air while under vacuum. The syringe graduations could not be expected to serve as a 1:1 volume ratio of air to water pulled into the tip, because the air had expanded under vacuum. This explains the negative systematic error we were experiencing.

Our solution was to replace the built-in scale with a scale that accounted for the expansion. We compared expected volumes with actual measurements and noticed a linear relationship. We scaled up the graduations by a factor of 1:1.027 for both the 100-1000 μL, and 30-300 μL configurations. These scales were exported to portable document format (PDF) so that they are most easily printed to scale by an end user. These adjusted scales are printed on paper or a transparency sheet and taped onto the syringe with the zero at the plunger when the pipette is in the latched position (Appendix B). With the new scale taped on the syringe our validation testing met the ISO 8655 standard. Replacing the scale with our scale that accounts for the expansion corrected this effect. Our printed pipette with the adjusted scale meets ISO standards for accuracy and precision. (Table 3.1 and 3.2, and Figures 3.5 and 3.4).

TABLE 3.1: ISO 8655 for 100-1000 μL comparing a commercial pipette with our printed pipette used with existing 3 mL syringe scale and an adjusted scale.

		Mean	Systematic Error	% Sys. err.	Random Error	% Rand. err.
1000 μL	ISO 8655, 100-1000 μL	1000	8.00	0.80	3.00	0.30
	Commercial Pipette	1002.98	2.98	0.30	1.72	0.17
	Printed Pipette	949.29	-50.71	-5.07	0.60	0.06
	Printed Pipette Scale	1003.57	3.57	0.36	0.89	0.09
500 μL	ISO 8655, 100-1000 μL	500	8.00	1.60	3.00	0.60
	Commercial Pipette	503.67	3.67	0.73	0.49	0.10
	Printed Pipette	475.99	-24.01	-4.80	4.75	1.00
	Printed Pipette Scale	503.62	3.62	0.72	1.64	0.33
200 μL	ISO 8655, 100-1000 μL	200	8.00	4.00	3.00	1.50
	Commercial Pipette	204.61	4.61	2.30	0.15	0.07
	Printed Pipette	186.55	-13.45	-6.72	1.31	0.70
	Printed Pipette Scale	201.87	1.87	0.94	1.47	0.73
100 μL	ISO 8655, 100-1000 μL	100	8.00	8.00	3.00	3.00
	Commercial Pipette	104.29	4.29	4.29	1.65	1.58
	Printed Pipette	94.02	-5.98	-5.98	4.81	5.12
	Printed Pipette Scale	101.00	1.00	1.00	1.05	1.04

TABLE 3.2: ISO 8655 for 30-300 μL comparing a commercial pipette with our printed pipette used with existing 3 mL syringe scale and an adjusted scale.

		Mean	Systematic Error	% Sys. err.	Random Error	% Rand. err.
300 μL	ISO 8655, 30-300 μL	300	4.00	1.33	1.50	0.50
	Commercial Pipette	301.19	1.19	0.40	0.53	0.18
	Printed Pipette	286.91	-13.09	-4.36	0.42	0.15
	Printed Pipette Scale	299.11	-0.89	-0.30	0.48	0.16
200 μL	ISO 8655, 30-300 μL	200	4	2	1.5	0.75
	Commercial Pipette	200.06	0.06	0.03	0.46	0.23
	Printed Pipette	193.40	-6.60	-3.30	2.86	1.48
	Printed Pipette Scale	200.57	0.57	0.28	0.86	0.43
50 μL	ISO 8655, 30-300 μL	50	4	8	1.5	3
	Commercial Pipette	49.02	-0.98	-1.96	0.10	0.20
	Printed Pipette	49.62	-0.38	-0.76	1.26	2.53
	Printed Pipette Scale	48.73	-1.27	-2.54	1.11	2.27
30 μL	ISO 8655, 30-300 μL	30	4	13.3	1.5	5
	Commercial Pipette	29.08	-0.92	-3.06	0.09	0.31
	Printed Pipette	29.22	-0.78	-2.59	0.31	1.07
	Printed Pipette Scale	27.78	-2.22	-7.41	1.37	4.93

3.3 Cell Encapsulation and Transformation

3.3.1 Droplet Formation

Monodisperse droplets of water in oil could be produced of $\sim$10μm in diameter. Droplets were stable and did not coalesce once formed. The downstream region of the device held the droplets in monolayer plane for convenient observation and imaging (Figure 3.6).

3.3.2 Prevention of Evaporation of Droplets

Due to the small volume of the droplets, they were susceptible to evaporation which caused them to shrink and disappear completely in less than 30 minutes. It was observed that closely packed regions of the incubation chamber evaporated more slowly and progressed from the perimeter in. It was hypothesized that in areas with higher densities of droplets, the oil was saturated with dissolved water vapor, which slowed or prevented evaporation. Once water vapor entered the oil, it can readily pass into the PDMS bulk of the device, which accelerates evaporation of the droplets.

3.3.3 Droplet Formation with Culture Media

Droplet formation in CDM, CAT, and LB medium failed. Jetting of the aqueous media at the droplet formation neck prevented proper droplet formation. M9 medium did produce droplets. Later testing showed that a ratio of up to 20% CDM in M9 was able to produce droplets. Coating the channels with a hydrophobic surface coating (Novec 1720, 3M) improved the stability of droplet formation. Coating with the hydrophobic coating also resulted in the added benefit of preventing large droplets or pockets of dispersed phase from sticking in the incubation chamber. The unfortunate result of the Novec 1720 coating was that it seemed to leave behind debris that could end up blocking the droplet neck. Additional filters were added in the oil channels just up-stream of the droplet generating region to catch these debris. 100% CDM was re-tested with the hydrophobic coating but did not generate droplets. Devices with a narrower neck of ~5 μm reduced the amount of flow rate tuning that was required to stabilize monodisperse production of droplets. Despite experimenting with neck width and attempting to tune droplet size with pump flow rate, stable monodisperse production of droplets smaller than ~15 μm was not achieved.

Observation of Cell Aggregates in Channels   Chains of cells appeared to adhere to channel walls, especially in sections that had constrictions or narrowed, such as at the inlets and filters. Less aggregation occurred when devices were treated with the hydrophobic coating (Novec 1720, 3M). It is hypothesized that these chains make up only a small fraction of the total cell population and the vast majority of non-chain-forming cells pass through the channels. Ultimately the narrower constrictions of the inlet filters were removed from the design as a precaution, to avoid the risk of complete blockage by the aggregating cells (Figure 3.8).

3.3.4 Transformation in Dilutions of CDM in M9 minimal medium

Transformation testing at high OD, up to 1.0, produced single and double recombinants. Single recombinants are CP2204 cells that gained Spc^R (RS plates) or Nov^R (RN plates) and double recombinats gained both Spc^R and Nov^R (RNS plates). Ratios of 20%, 10%, and 1% CDM in M9, as well as M9 medium only, produced single and double recombinants (Table 3.3.) Transformation efficiency was attenuated compared to transformation

in 100% CDM. Testing transformation in M9 medium confirmed that transformation did not occur in the absence of CSP or when the strains were kept separate (Table 3.3). The detailed protocol can be found in Appendix B). Small and large colonies were observed on some plates. Later plating on THY agar resulted in more uniform sized colonies.

3.3.5 Imaging of Cells in Droplets

Cells could be imaged in droplets with phase contrast microscopy. All cells appeared to fluoresce for RFP rather than a spilt population of RFP and GFP that was expected. Because the bacteria was moving, a relatively high laser power needed to be used, which resulted in photobleaching of the cells. Individual cells, as well as pairs and groups could be seen moving within the droplets. Rarely, clumps of cells were observed in droplets (Figure 3.9 A and Figure 3.10 E). Diplococci cells were observed as well as individual cocci. Time lapse imaging for up to 30 minutes did not reveal any obvious fratricide events, lysis or disappearance of cells. Devices with coverslip bottoms allowed imaging with higher magnification oil immersion objectives, which resulted in higher quality images (Figure 3.10.)

3.3.6 Occupancy Distribution of Cells in Droplets

Twenty-five representative cells were selected and viewed in time lapse and the number of unique cells was estimated (Figure 3.12). The amount of cells in each droplet ranged from 1 to 5 cells. The average occupancy was 2.5 cells per droplet and the mode was 2 cells per droplet.

3.3.7 Droplet Size

Images of droplets with clear and in-focus cells were used to estimate droplet size. ImageJ was used to measure the cell length, which was used as a frame of reference for the droplet diameter (Figure 3.13). The average diameter of these droplets was measured to be 16 μm. The incubation chamber is 10 μm tall. Because the droplets were larger than 10 μm in diameter, it was assumed that they were compressed in the z direction deforming the spherical shape and changing to an ellipsoid shape. Calculations of volume took into account this deformation using equation:

TABLE 3.3: Experiment testing efficacy of M9 media and inducible competence.

Reaction	CDM	Inducer (CSP)	Cells	Rifampicin (R)	R-Small	Spectinomycin (S)	RN	RN-small	RS	RS-small	RNS
1	20%	+	Mix	2.15E+08	1.04E+09	2.73E+08	4.25E+04	5.96E+05	2.93E+04	1.15E+06	64
2	0%	+	Mix	2.36E+08	-	2.33E+08	3.94E+04	5.81E+05	2.79E+04	9.98E+05	35
3	20%	-	Mix	1.87E+09	-	2.04E+08	0	-	0	-	0
4	0%	-	Mix	8.24E+08	-	2.12E+08	0	-	0	-	0
5	20%	+	CP2215	0	-	2.33E+08	0	-	0	-	0
6	20%	+	CP2204	1.80E+09	-	0	0	-	0	-	0

Note: The -small tag are counts of smaller more numerous CFUs that emerged after 2 day incubation.

TABLE 3.4: Estimation of droplet size using *S. pneumoniae* cells as a reference.

Droplet	Cell	Diplococci pneumoniae	Single pneumoniae	Cell length (pixel)	Droplet diameter (pixel)	Calculated droplet diameter (μm)	Calculated droplet volume (μm^3)
1	1	X		2.1	30.1	28.7	4304.9
	2	X		2.4	30.1	25.1	3302.6
2	1		X	1.3	19.7	15.7	1296.8
	2		X	1.1	19.7	17.9	1680.4
3	1		X	1.8	19.9	11.0	636.6
	2		X	1.3	19.9	15.5	1265.0
4	1		X	1.4	19.9	13.9	1016.8
5	1		X	1.3	19.9	14.7	1136.5
6	1	X		2.5	17.9	14.4	1082.4
	2		X	1.0	17.9	17.2	1545.4
7	1		X	13.1	200.4	15.3	1222.4
8	1		X	1.4	17.7	12.7	839.1
	2		X	1.4	17.7	12.7	850.0

Note: Individual *S. pneumoniae* cells are between 0.5 and 1.25 μm in diameter. For simplicity, one single pneumoniae cell was assumed to be 1 μm in diameter and a diplococci pneumoniae was assumed to be 2 μm in length.

$$V = \frac{4}{3}\pi abc, \tag{3.1}$$

where $a = b =$ the observed radius of the droplet, and $c = 5$ μm. The average volume was calculated to be $1.5E^{-9}$ mL^3(Table 3.4) with a coefficient of variation (CV) of 68%. Using this to calculate the cell density yields $1.6E^9$ cells/mL^3.

3.3.8 FTIR Imaging of DNA and *E. coli*

Signature peaks for DNA were found around 1400 wavenumber·cm^{-1} (Figure 3.14) and 3000 wavenumber·cm^{-1}. The peak was higher with freshly resuspended DNA in D$_2$O. After a week this sample was tested and the peaks were smaller but still present. It is assumed that residual protons are slowly exchanged with deuterons in the sample over time. Therefore, the signature from this one week incubated sample is considered to be a more accurate signal for DNA.

FTIR imaging comparisons between the *E. coli* with and without lysis buffer showed that in non lysed cells the DNA was in confined within the cells. In the droplets with lysis buffer the DNA is found spread throughout the droplet (Figure 3.15).

TABLE 3.5: Droplet encapsulated and non-encapsulated control cell counts.

Jan 24 OD: 0.1	S	R	RN	RS	RNS
droplets	0.00E+00	8.89E+04	0.00E+00	0.00E+00	0.00E+00
control	4.00E+05	8.36E+07	0.00E+00	0.00E+00	0.00E+00

Feb 14 OD: 0.2	S*	R	RN	RS*	RNS
droplets	6.13E+08	7.07E+08	0.00E+00	9.69E+06	0.00E+00
control	4.80E+10	4.93E+10	0.00E+00	2.67E+08	0.00E+00

March 07 OD: 1	S	R	RN	RS	RNS
droplets	0.00E+00	4.89E+06	0.00E+00	0.00E+00	0.00E+00
control	4.89E+06	3.60E+09	0.00E+00	0.00E+00	0.00E+00

March 22 OD: 1	S	R	RN	RS	RNS
droplets	0.00E+00	4.44E+05	0.00E+00	0.00E+00	0.00E+00
control	2.67E+06	2.48E+09	0.00E+00	0.00E+00	0.00E+00

*Streptomycin was mistakenly used rather than spectinomycin. One or both strains are apparently resistance to streptomycin. These CFUs counts are a false result.

3.3.9 Transformation in Droplets

Experiments attempting transformation in droplets resulted in zero transformants in either droplet encapsulated sample and non-encapsulated control samples. Cell counts were unexpectedly low in the non-encapsulated control, especially for CP2215 the Spc^R strain. CP2215 in the encapsulation sample did not survive and the Rif^R CP2204 counts were reduced by 10^4-fold. The control for these experiments also produced similar low CFU counts (Table 3.5).

Further control experiments were designed to find what was happening to the cells and at what stage in the procedure. In one experiment, quick emulsions were made by vortexing suspension with an equal volume of oil. Emulsions of suspensions were tested with both M9 and CDM medium. In addition, two dilutions were tested for the 1 h incubation step. All of the reaction conditions tested yielded similar and expected CFU counts compared to other non-emulsion or non-encapsulation experiments. No condition reproduced the loss of cells that was experienced during droplet encapsulation experiments.

More control experiments were performed to test if time held at chilled temperatures killed cells. Again, M9 medium was compared to CDM medium. Rather than a complete transformation test, the survival of each strain was tested at different time-points along a temperate cycle. The temperature protocol followed the approximate times the cells

TABLE 3.6: Comparison of emulsified suspensions in CDM *vs.* M9 and the effect on cell viability and transformation.

Rx	Rx Condition	Media	1hr dilution	Rifampicin (R)	Spectinomycin (S)	RN	RS	RNS
1	Emulsion	CDM	1.00E-01	1.47E+07	1.57E+07	5.00E+03	2.50E+03	9.87E+03
2	Bulk	M9	1.00E-02	8.13E+07	5.60E+07	3.00E+03	5.00E+03	4.40E+03
3	Bulk	M9	1.00E-01	8.11E+07	5.55E+07	4.96E+04	9.00E+03	1.61E+04
4	Emulsion	M9	1.00E-01	4.00E+07	3.63E+07	4.10E+03	1.90E+03	5.33E+03
5	Bulk	CDM	1.00E-02	1.83E+08	4.75E+08	1.01E+06	9.00E+04	2.63E+05
6	Bulk	CDM	1.00E-01	9.13E+07	6.93E+07	2.05E+05	7.07E+04	2.25E+05

were held during each stage of a droplet transformation experiment. These control experiments also did not reveal the condition that caused the dramatic loss of cells. It seems that the cells are not affected by being held in M9 or CDM medium at 4°C, or cycles of 4°C to 37°C to RT.
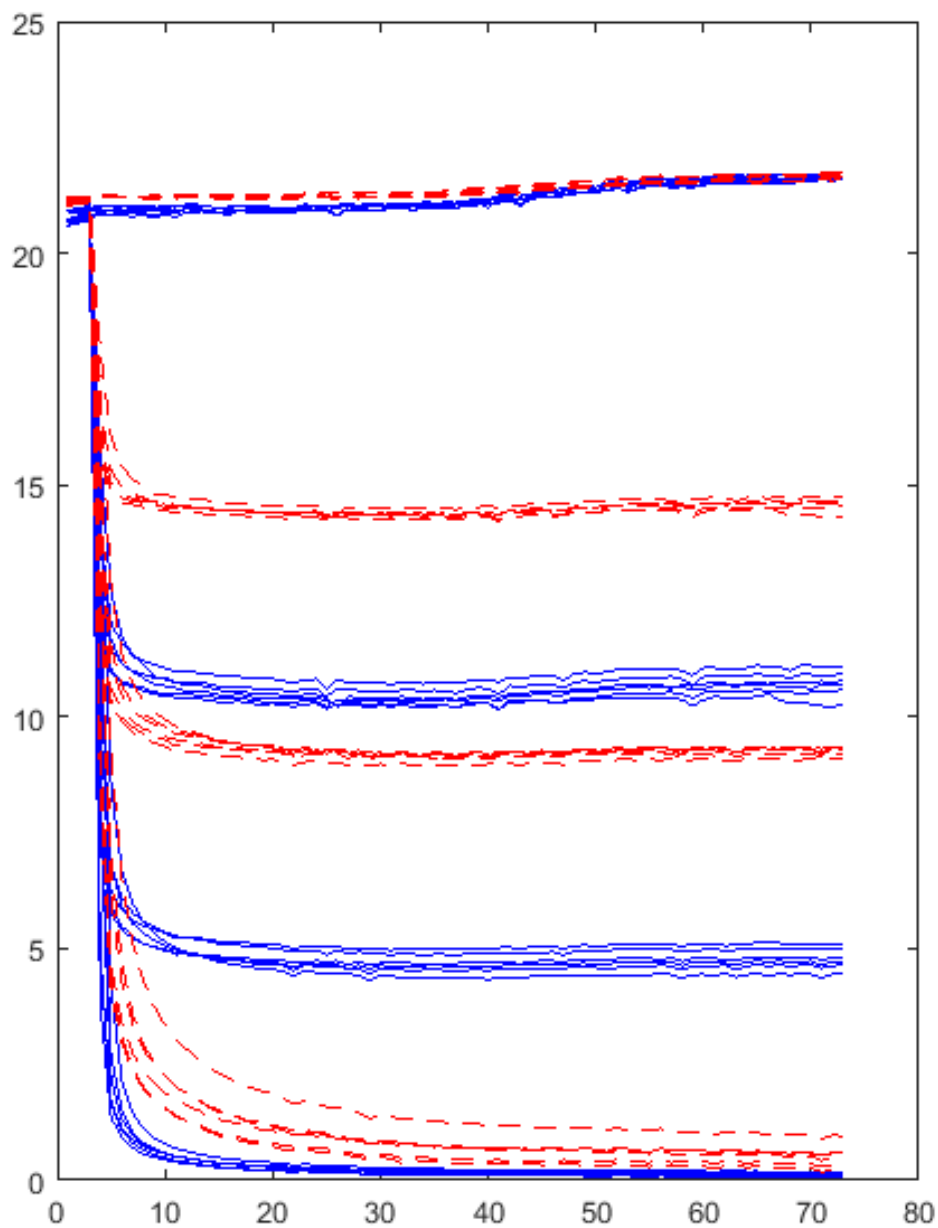
FIGURE 3.1: **Data analyzed with the standard and two-site Stern-Volmer model.** The same time course data analyzed with only 0% and 21% calibration points (red dotted-line) *vs.* a two-site model that with five calibration points(blue line). The oxygen conditions that were applied were 0%, 5%, 10% and 21%.
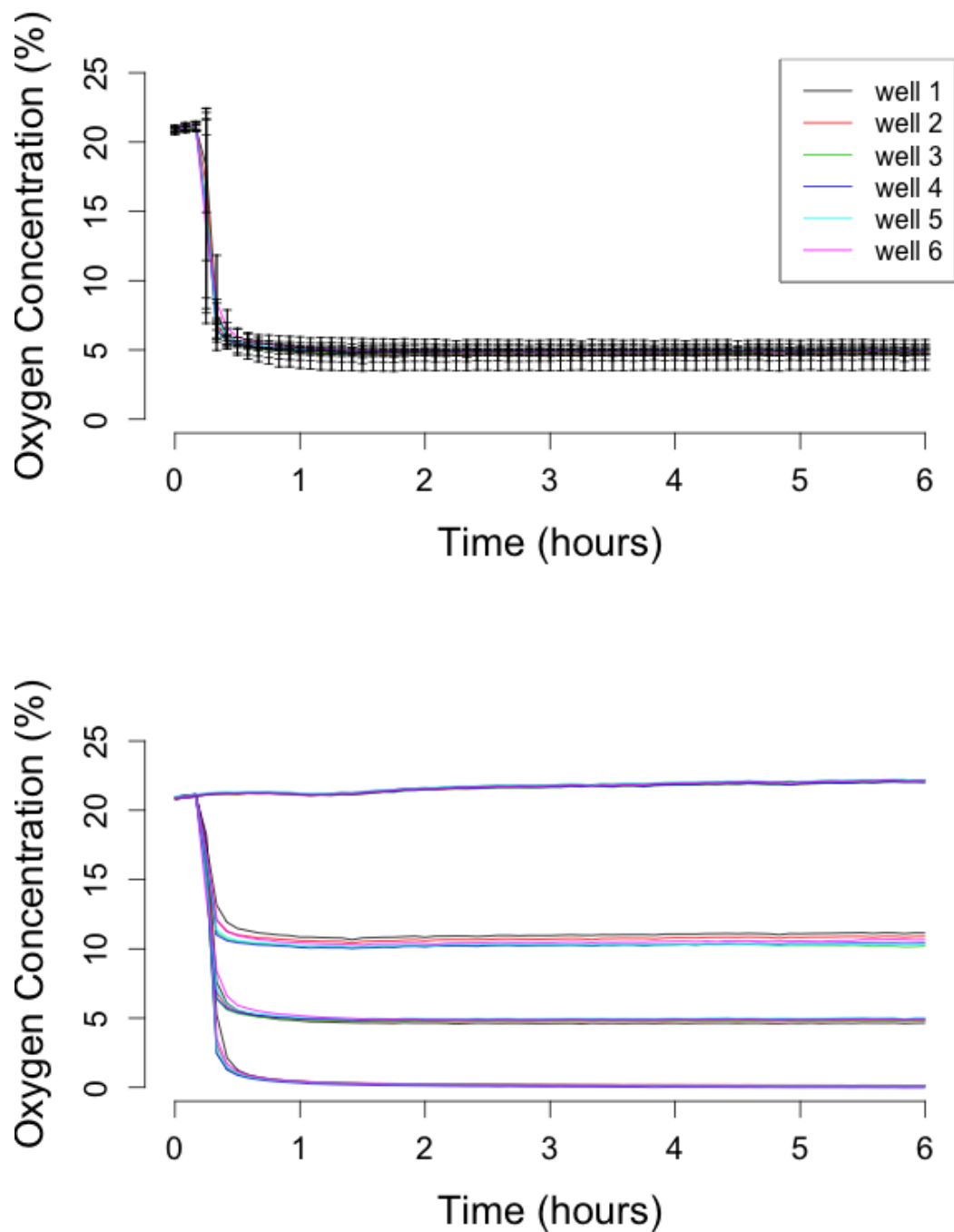
FIGURE 3.2: **Oxygen characterization in 24-well insert.** Time course data of oxygen being evacuated from the culture area as 5% oxygen gas mix is perfused through the device (above). Error bars are the standard deviation N=3. Four oxygen conditions are demonstrated in a 24-well plate (below). Each 6-well row of the plate can be controlled independently. Mean N=3 error bars not shown.
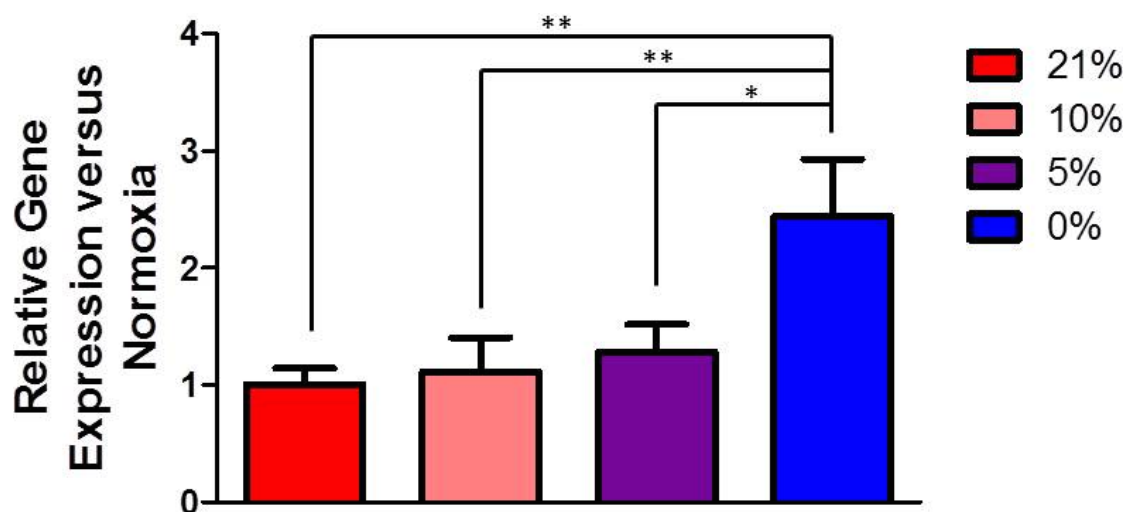
FIGURE 3.3: **PCR data.** VEGFA expression in A549 cells after exposure to different oxygen conditions set-up by the insert device. Data are expressed as mean $\pm$ SD, N=3. Note that Megan Rexius-Hall performed the PCR analysis and prepared this figure.
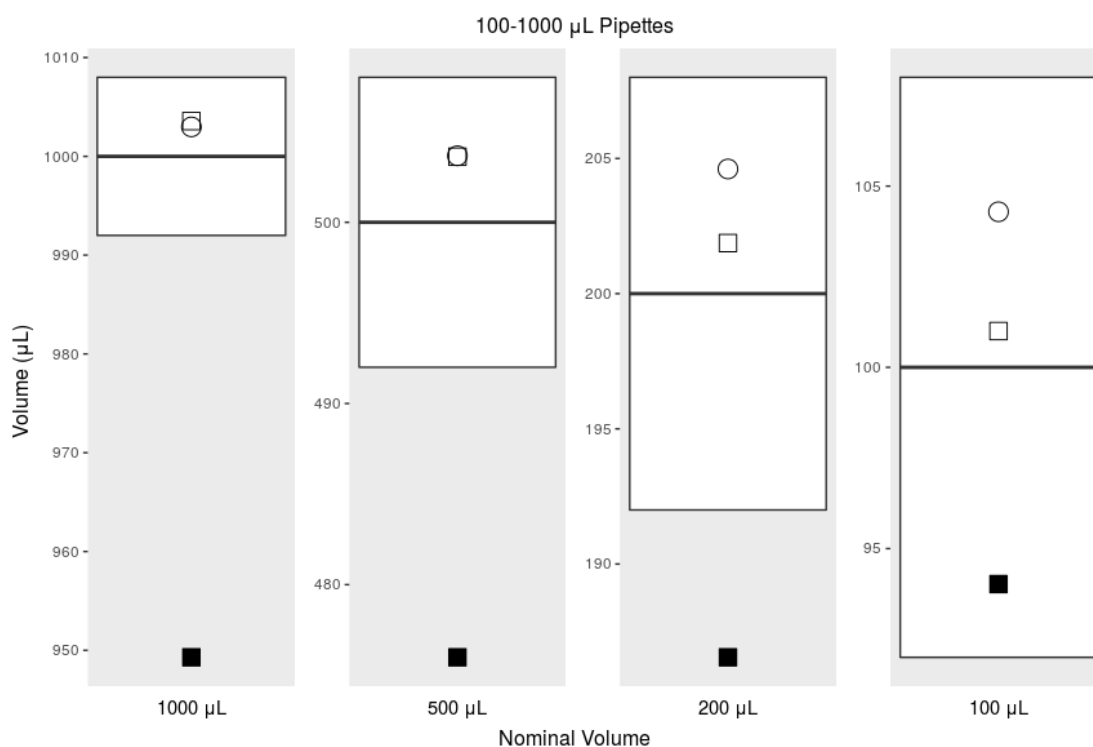
FIGURE 3.4: **Comparison of the accuracy, or systematic error, between 100-1000 μL pipettes.** The box plot indicates the range of the ISO standard, the plotted circle indicates the commercial pipette, and the plotted squares are the printed pipette. Empty squares are with the printed pipette with our adjusted graduation scale, and the filled squares are measurements taken with the syringe's existing graduations. (Data from Table 3.1)
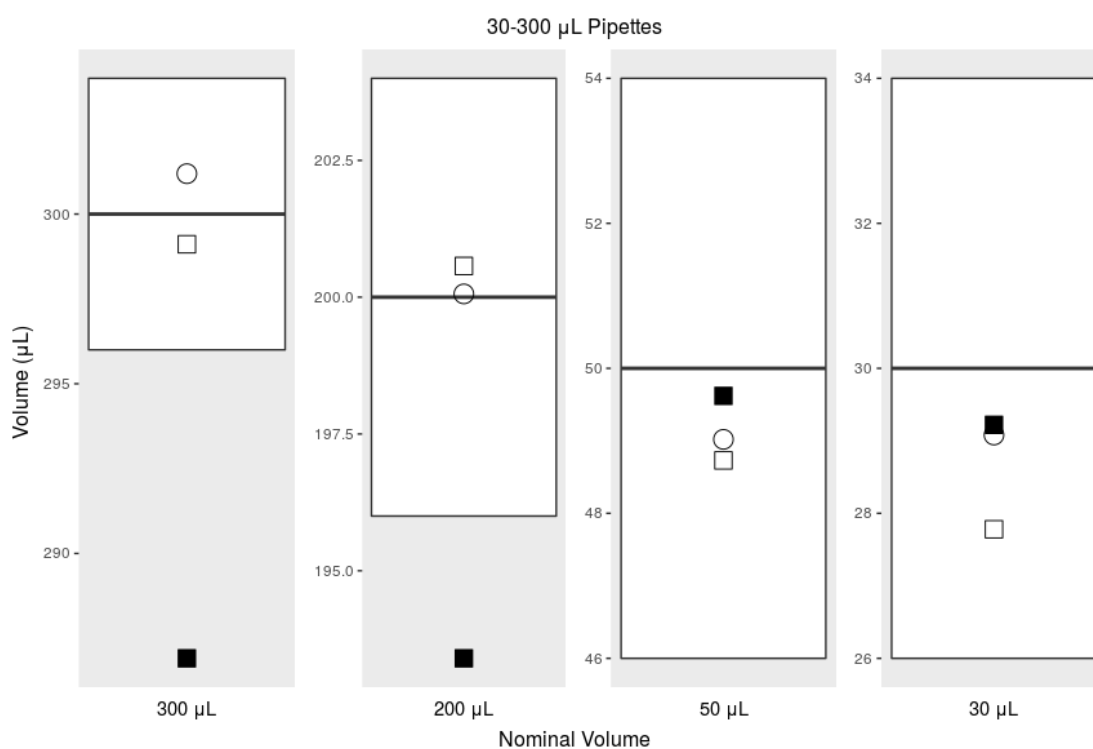
FIGURE 3.5: **Comparison of the accuracy, or systematic error, between 30-300 μL pipettes.** The box plot indicates the range of the ISO standard, the plotted circle indicates the commercial pipette, and the plotted squares are the printed pipette. Empty squares are with the printed pipette with our adjusted graduation scale, and the filled squares are measurements taken with the syringe's existing graduations. (Data from Table 3.2)
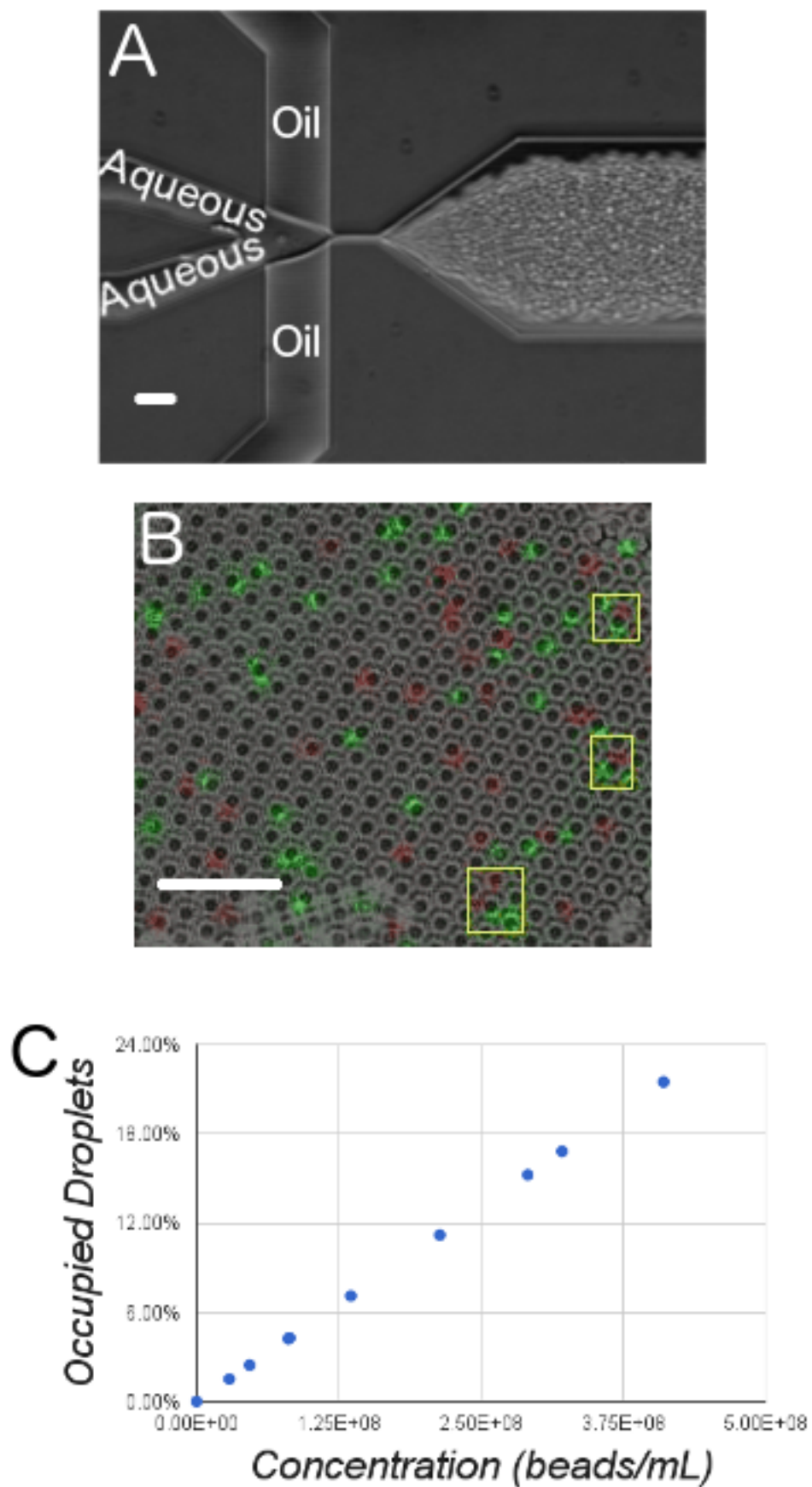
FIGURE 3.6: **Micrograph of droplet production.** (A) and encapsulation of green and red beads(B). Yellow boxes indicate droplets with a red and a green bead. (C) Occupancy characterization dependant on concentration of beads.
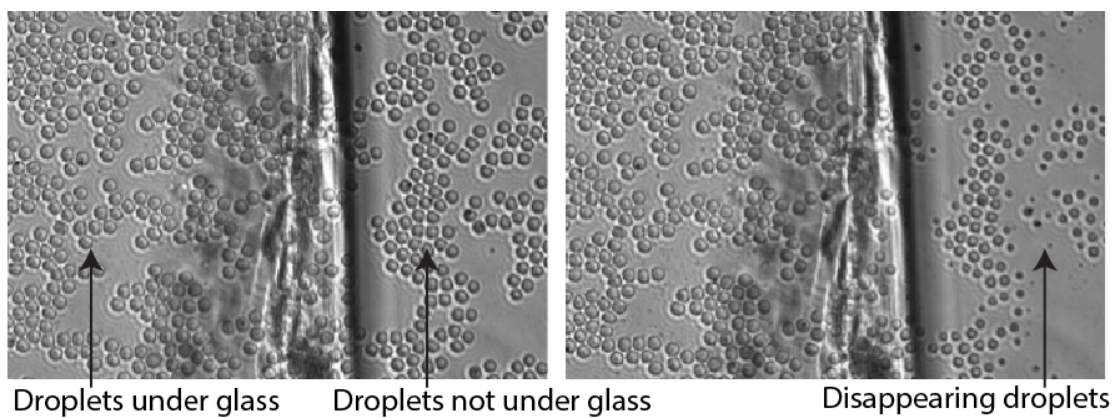
FIGURE 3.7: **The prevention of droplet evaporation by the coverslip layer.**
Droplets on the left of each image are under a coverslip layer of the incubation chamber.
The right panel is after 10 minutes of incubation showing the evaporation of the droplets
that are not under the coverslip.
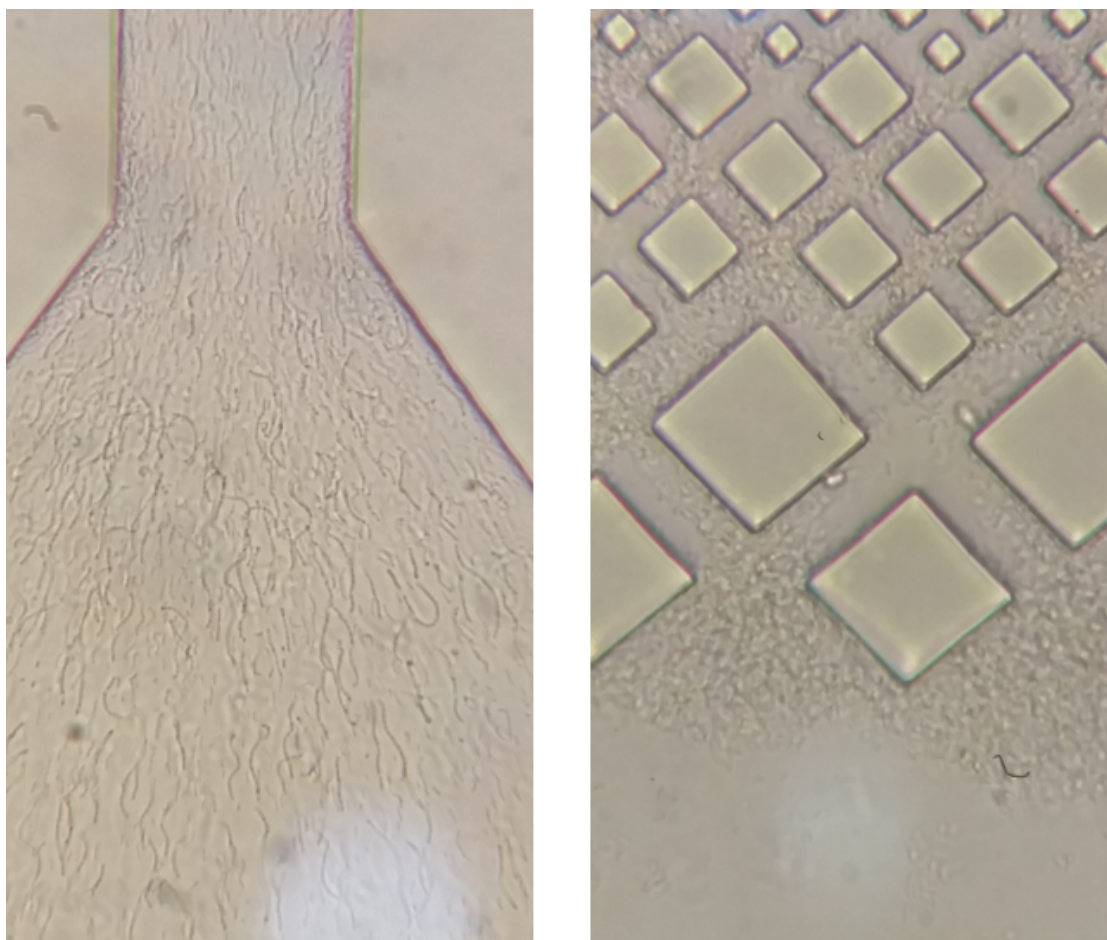
FIGURE 3.8: **Aggregate of cells in channels.** Cells adhere to the channel walls
as the inlets narrow (Left). Aggregates in the filters at the inlets (Right). The flow
direction for both images is from bottom to top.
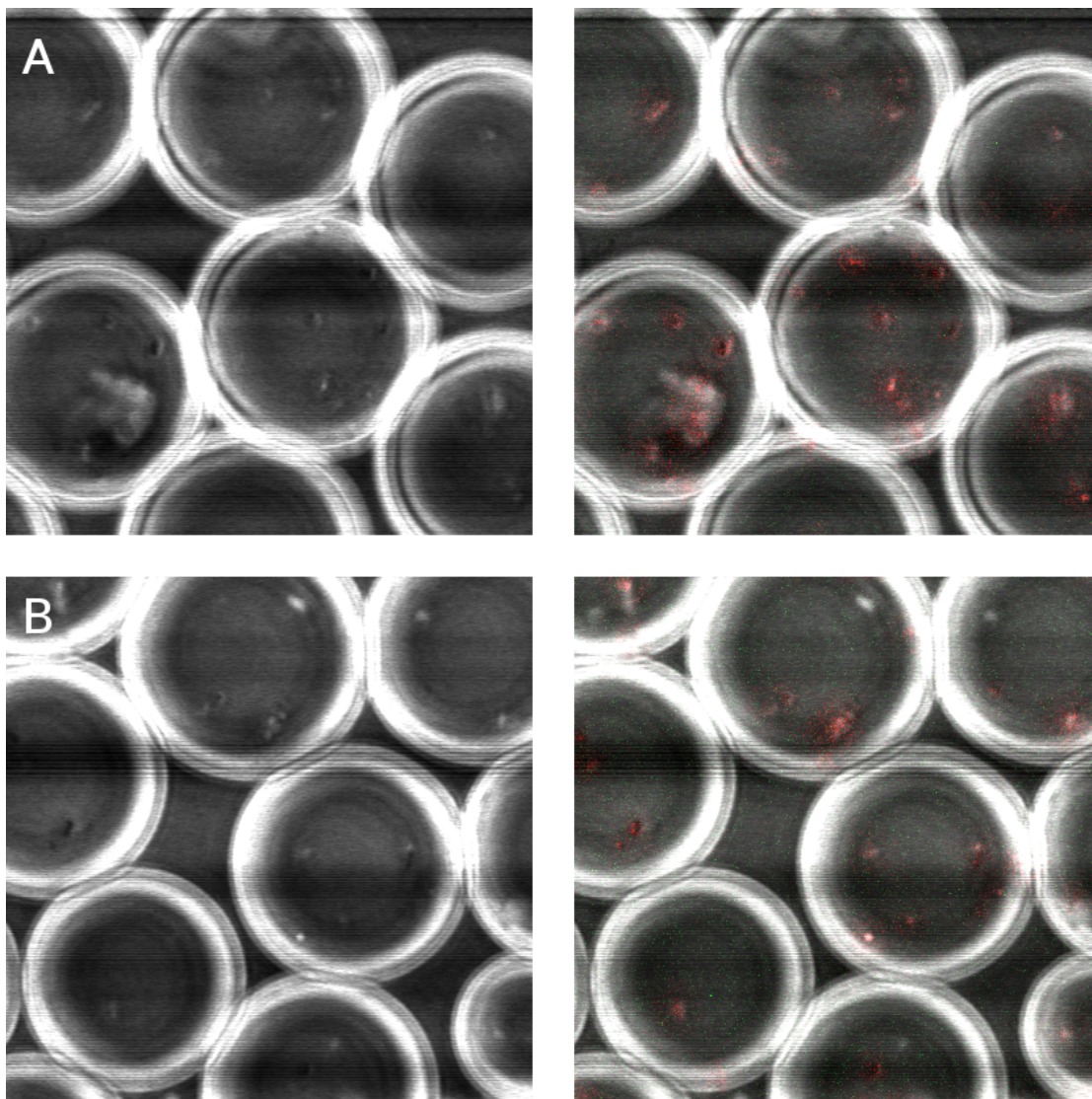
FIGURE 3.9: **Cells in droplets within the on-chip incubation chamber.** The left panel is phase contrast. The right panels are composite are overlays of RFP and GFP on the phase contrast image.
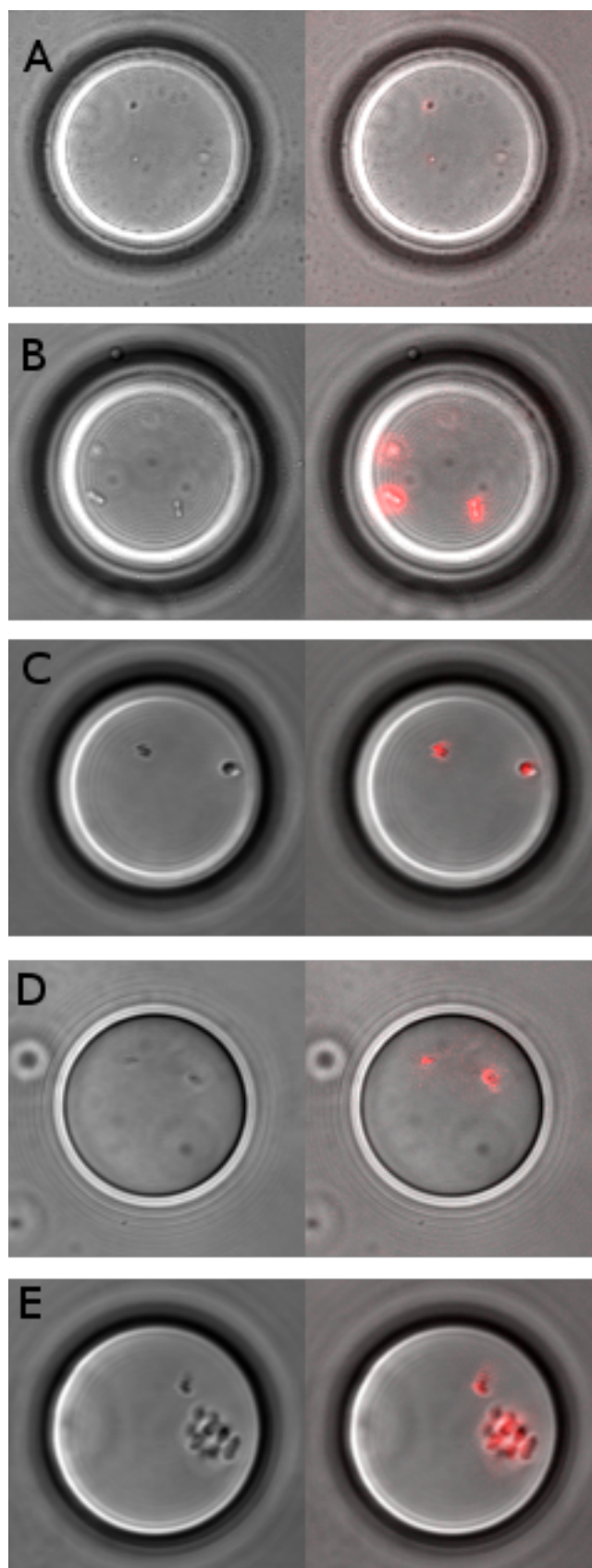
FIGURE 3.10: **Cells in droplets dispensed between coverslips.** Droplets were selected that had two or three cells. The left panels are phase contrast and the right panels are RFP overlays.
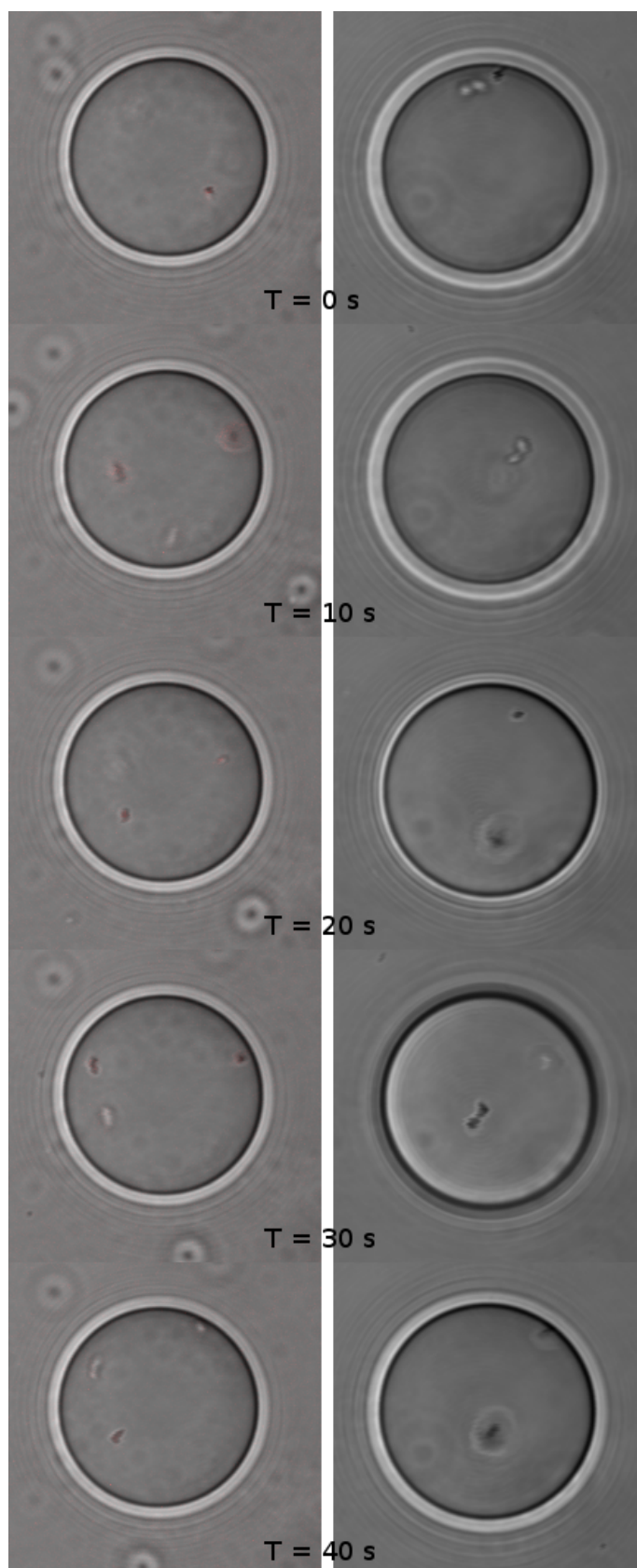
FIGURE 3.11: **Time lapse images of two selected droplets taken 10 seconds apart showing movement of cells within the droplets.**

Droplet Occupancy Distribution
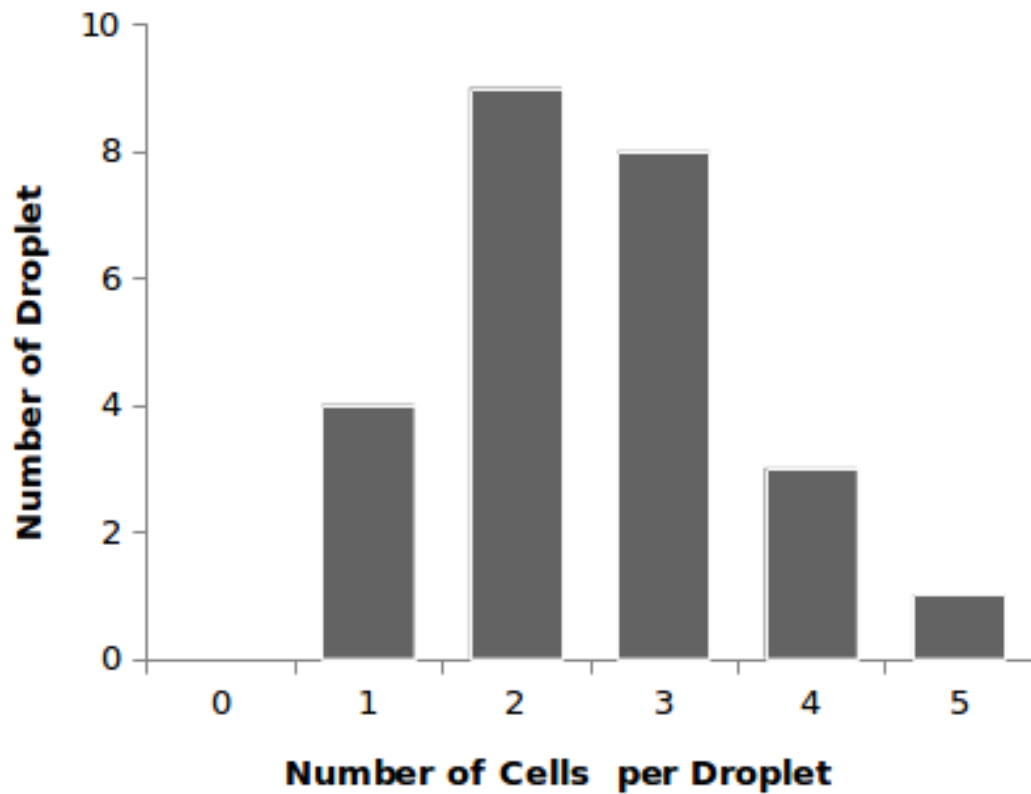
FIGURE 3.12: **Occupancy distribution of 25 representative droplets.**
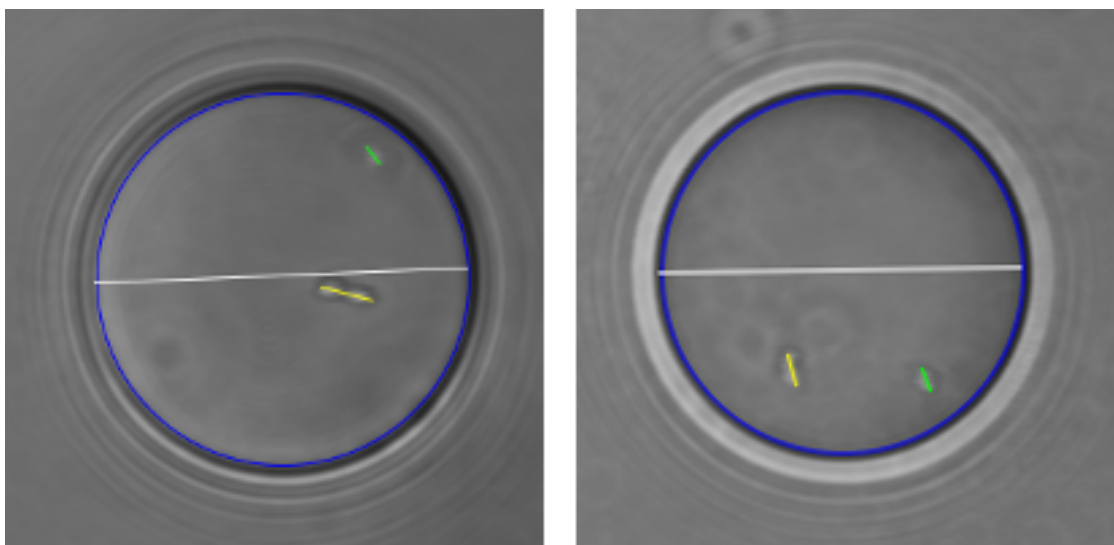
FIGURE 3.13: **Measurement of droplet size using cells as reference.** Green: the length of a single *S. pneumoniae* cell, yellow: the length of diplococcus pneumoniae, blue: droplet, white: the diameter of droplet.
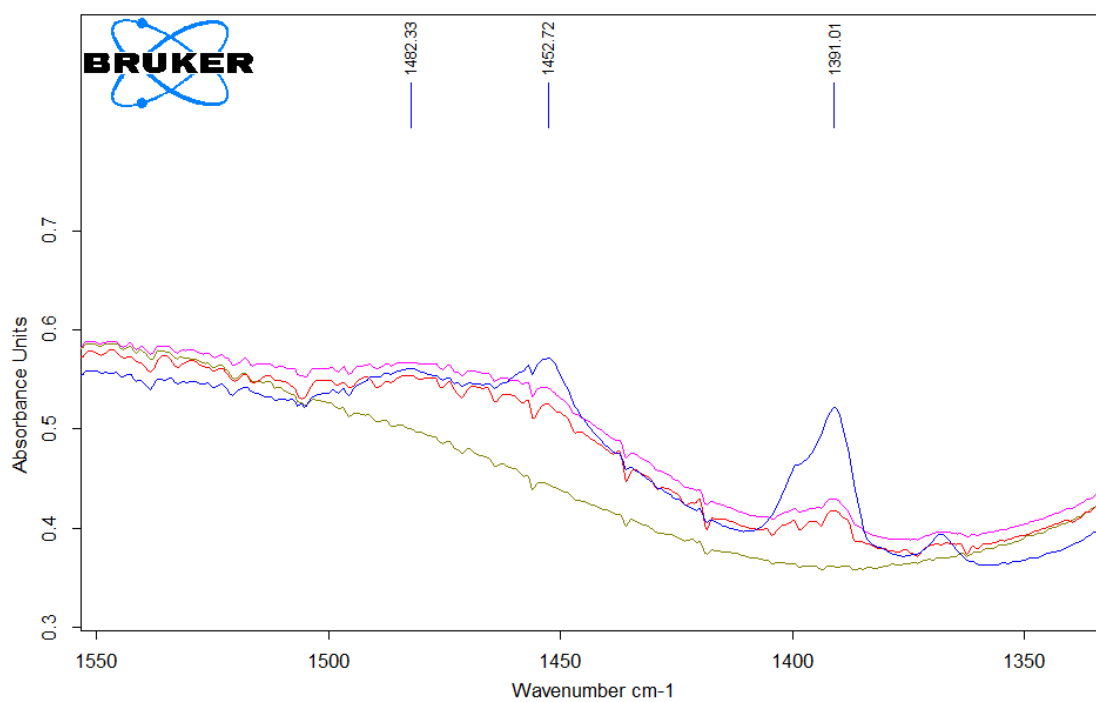
FIGURE 3.14: **DNA FTIR signal.** FTIR signal of Lambda DNA resuspended in D_2O. The relatively smooth brown line is D_2O only as a reference. The blue line with the most significant peaks at 1390 and 1450 wavenumber$\cdot cm^{-1}$ is freshly suspended DNA in D_2O. The intermediate red and pink lines are two readings from the same sample incubated for 1 week in D_2O.
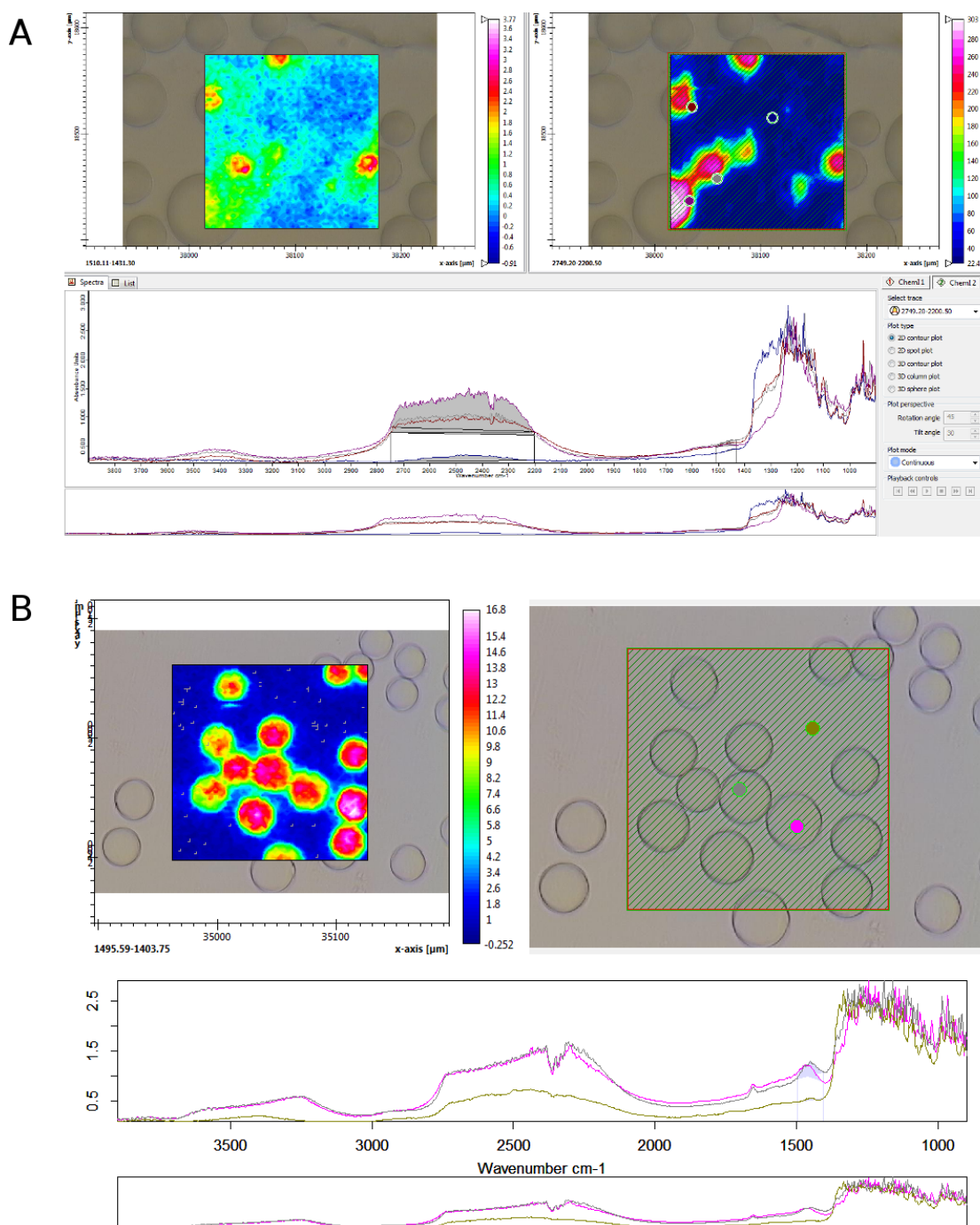
FIGURE 3.15: **FTIR signal of DNA in droplets with encapsulated *E. coli*.**
FTIR signal of DNA shows that it is confined within cells (A, left). An overlay of the
D_2O signal is also shown (A, right). (B) In droplets with cells encapsulated with lysis
buffer, the DNA is detected within the whole droplet.

Chapter 4

Discussion

(Previously published as Martin D Brennan, Megan L Rexius-Hall, and David T Eddington. A 3D-Printed Oxygen Control Insert for a 24-Well Plate. Plos One, 10(9):e0137631, 2015. ISSN 1932-6203., Martin Brennan, Fahad Bokhari, and David Eddington. Open Design 3D-Printable Adjustable Micropipette that meets ISO Standard for Accuracy. bioRxiv, 2017. Permissions statements are included in Appendix D.)

4.1   Oxygen Control Insert

Improvement From Previous PDMS Devices   This new iteration of the multi-well insert for oxygen control maintains the convenient features of the previous 6 well-plate design[1, 40] while improving distribution and interfacing with tubing directly via the 3D-printed hose barbs. Oxygen control is performed in an off-the-shelf culture plate allowing standard protocols to be used for analysis assays or imaging. Additional protocols are often required when cells are seeded within microfluidic chips. The ability to independently control oxygen across each row of the plate enables more efficient experiments as a separate incubator or hypoxic chamber is not needed for each condition. This oxygen insert proved to be a capable platform for controlling oxygen in a 24-well plate. The desired dissolved gas concentration was reached in about 30 minutes and the desired concentration was uniformly delivered across each well in the 6-well unit. Bioverification of oxygen control with A549 cells was also a success as the cells responded by upregulation of VEGFA mRNA after 6 hours of 0% O_2. The VEGFA gene expression

in A549 cells confirms a biological response using the multi-well insert. This 3D-printed device improves on our previous design in a number of ways. First, this 3D printed insert provides a step up in multiwell plate support while simplifying fabrication. No microfabrication, PDMS molding or Parylene coating is required like previous devices[1]. The only fabrication step with the oxygen control insert is the attachment of the oxygen permeable membranes. It would be convenient if a 3D-printed material was oxygen permeable to print the device with. Direct 3D printing with PDMS is being actively developed [87, 173], which is exciting for potential oxygen control and biocompatible devices.

Conveniently, the non-permanent adhesion of membranes to the 3D-part allows them to be removed and replaced if they are damaged. In PDMS devices the layers are bonded permanently via plasma bonding, so damage to a membrane is not repairable. 3D-printing also enables higher levels of intricacy without any additional fabrication, allowing us to include the distribution network, overlapping of channels, and the "pipe within a pipe" design. A comparable PDMS device would require several additional microfabricated layers to be manually aligned to reproduce just the distribution network.

Limitation of 3D Printing Materials   One major limitation of 3D printing thus far is the limited choice of materials. Watershed XC, the material used for the oxygen insert, is a proprietary material whose exact formula is not shared. Au *et al.* authored an excellent report on the capabilities of this material and printing technology for microfludics [75]. Unknown materials in contact with cells provokes biocompatibility concerns although no effects were noticed with A549 cells. Watershed XC as well as several other popular 3D printed materials have been shown to be toxic to zebrafish embryos[169]. Watershed XC is delivered as a colorless transparent material but turns to an amber yellow when left out exposed to light. This suggests that material is not completely cured and may leach substances into the culture media. In all our experiments with A549 cells, inserts were sterilized by spraying with 70% ethanol and exposed to UV light in a biosaftey hood overnight. No biocompatibility effects were noticed, perhaps due to the UV sterilization step that may have fixed some uncured material and prevented it from leaching into the media.

4.1.1 Improving and Expanding Function of the Insert

Moving forward with additive manufacturing of microfluidic devices is desirable as it will enable highly integrated designs without any additional fabrication. The most immediate step would be making designs for higher number plates like the 48-well and 96-well formats. With the flexibility of 3D-printable devices, many additional features can be integrated to future design iterations of this insert.

Reducing the Number of Gas Tanks   Despite the compact design of the device, it still relies on bulky pressurized cylinders to supply the gas of interest. In the design's current configuration, one tank is required for each desired gas condition. An integrated dilution-tree gas mixer could allow more conditions in a single plate, perhaps even one per well while also reducing the number of gas tanks required as inputs[174]. Additionally, the gas set-up for this device included a vacuum source to drive flow through the device. This was to make sure that flow through each of the four units was even without the need to independently measure each one and also to reduce the chance of bubble formation and bursting of the membranes. These concerns may have been exaggerated and the device could be driven with pressure from the tanks eliminating the need for a vacuum source. With 3D-printing, an integrated flow regulation valve could be included into the device as well.

Media Exchange   With the existing design, the insert must be removed from the plate to exchange media. Ports in each well or a media perfusion system can be integrated to the design to enable long term studies. Live oxygen measurement could also potentially be performed through ports or sensors could even be integrated into each well. Live oxygen measurement could be performed by integrating excitation and detection modules[23]. Additionally, the bottom of each well provides an opportunity for further functionalization with existing microfluidic oxygen landscape schemes. Rather than a uniform condition across the well bottom binary[170], gradient[48], and other designs can be integrated.

Exploring Alternative Membrane Materials   PDMS is not desirable for large-scale manufactured production where injection molding is preferred. Other plastics such

as low density polyethylene (LDPE) and PTFE would be good candidates for membrane materials as they have acceptable oxygen diffusion rates. Permanent thermal bonding of PDMS and other plastics to Watershed XC has been reported[75], so this insert would potential allow testing of these material as oxygen permeable membranes.

4.1.2   Sharing CAD Designs

One of the convenient advantages of the push towards 3D-printed devices is the shareability of designs. Every dimension is completely defined in the CAD models, so the sharing of the printable design file can eliminate ambiguities of traditional documentation[2]. This allows others to quickly reproduce devices and results without first needing to reproduce designs and learn fabrication. Many researches in far-ranging disciplines have an interest in investigating the role of oxygen or other dissolved gasses in their studies. This insert, whose fabrication is outsourced, allows convenient control in an ubiquitous multi-sample platform enabling a non-expert to perform oxygen studies. To facilitate sharing in this case, the design and documentation is freely available in an on-line repository [175].

4.2   3D-printed Pipette

A functional pipette was produced from the assembly of the 3D printed parts and additional hardware. 3D-printable micropipette works by actuating a disposable syringe to a user adjustable set point. This allows the user to set the pipette to a volume by reading the graduations on the syringe barrel. An adjusted graduation scale was developed, to be used in place of the printed on scale, that corrects for the compressibility of air which allows the pipette to be set accurately. When the adjusted graduation scale is used, the pipette is capable of satisfying ISO specifications for accuracy and precision.

Improvement From Existing Designs   Our printed pipette improves on existing open design pipettes in several ways. Most significantly, the user is able to adjust the syringe accurately without verifying the volume with a scale. The pipette can be adjusted to any discrete volume within range. In addition, the assembly requires no permanent connections using tape or glue which allows for re-configuration and easy

replacement of parts. Conveniently, our design can also reach to the bottom of a 15 mL conical tube, allowing tasks such as aspirating supernatant fluid from a cell pellet, a feature not possible with competing designs[4]. Unlike existing designs, our design does not use a membrane that may wear out and require replacement. The only major limitation of this design compared to the biropipette[4] is the option for a pipette tip ejector. The biropipette also uses arguably easier to source parts (a pen *vs.* a syringe) relative to what is required from our design. The biropipette also was developed in OpenSCAD which is free and open source CAD software while our design was created in Solidworks a proprietary software. This creates a limitation for users who may not have access to the proprietary software used to make the design. Fortunately the produced STL files are universal and can be imported an modified by any CAD software.

Limitations of the Design The luer to pipette tip connection is a good candidate for a 3D printed solution. Unfortunately the current state of FDM can not make this adapter with high enough resolution or critically, surface smoothness. Other printing techniques, such as stereolithography (SLA) and MultiJet Printing (MJP), provide higher resolution and smoother finishing, yet FDM is the the most widely available and affordable of printing technologies. SLA printers are coming down in price but are still significantly more expensive especially considering the higher cost of the consumable resin vs. FDM filament. Ultimately the goal of this project is to make this pipette cheap and easy to make.

Our design relies heavily on the syringe, a specialized part, for the core function as well as accuracy. Fortunately, as disposable syringes are a regulated medical device they must meet high standards, making them a reliable part for this design. As good as the performance of our printed pipette is, a commercial pipette should be expected to be more reliable and would be preferred for critical procedures. Adjusting our printed pipette to the desired volume requires more time and attention, which would be tedious for procedures requiring many adjustments. On the other hand, due to the $6 cost to make, many printed pipettes could be assembled and pre-set, each for a planned transfer, rather than re-adjusting one commercial pipette for each step. The printable pipette can also be used as a disposable, sparing the commercial micropipette, in situations where cross-contamination and resterilization is required, or damage from volatile reagents is

a concern. This pipette would also be ideal for high school and teaching labs or any resource limited program.

Improvements Moving Forward One critical limitation of this pipette is the absence of pipette tip ejection feature. For practical use of this pipette in a lab setting, this is an essential convenience. To add this feature to our pipette, a significant redesign would need to be undertaken. First, the syringe is not held in place strongly enough to stay in place as a tip is pushed off. The printed body part would have to extend to the end of the syringe, but there is not much room for it to interface with to hold it in place. Also, a better solution for creating a quick seal between the pipette tip and the syringe needs to be developed. Currently elastic tubing is used as a sort of gasket to provide a seal and hold the pipette tip in place. A typical ejection system would struggle to push a pipette tip off of this gasket. The problem with 3D printing a luer-to-tip adaptor is that the ridges formed by each layer by FDM printers prevents an air-tight seal. A few solutions have been developed to re-finish or smooth these ridges that may provide viable options[127]. In addition, configurations for transferring volumes below 30 μL would extend the range of this pipetting system. Disposable syringes of a nominal volume as low as 0.3 mL are available and would provide a good working range for a 5-50 μL configuration to be developed.

4.2.1 Sharing the Design as an Open-Source Project

The open design nature of this project encourages anyone to view the documentation and download the CAD designs for printing[176] (Figure 4.1). The project is currently under the GNU General Public License v2.0[177], which allows it to be used, modified, distributed and sold and extends these freedoms to all the recipients of the designs as well. The on-line repository (a GitHub repository [102]) is also set up so that users can download a working directory to their computer and modify and submit fixes and improvements back to the project managers. It is the goal of this project, as is every open-source project, to encourage collaborative and transparent work for all to use.
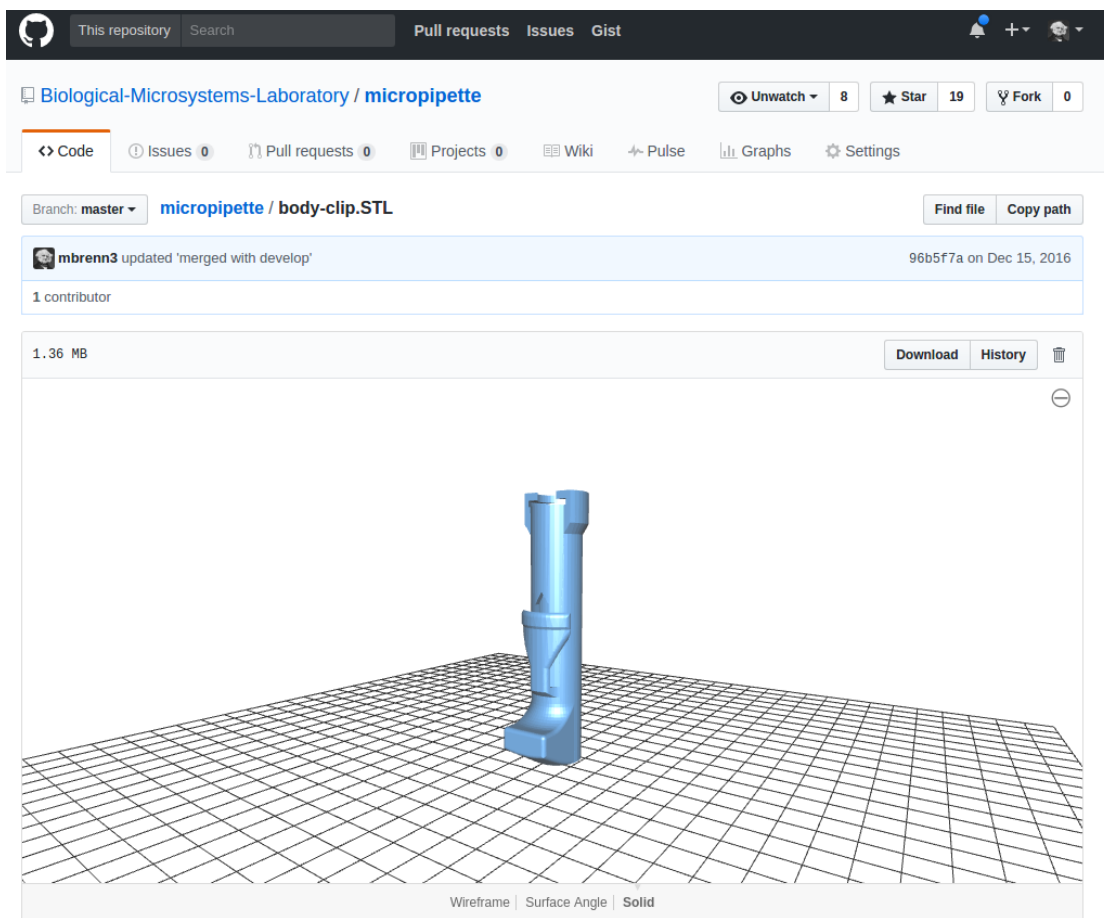
FIGURE 4.1: **Screenshot of the GitHub repository for the pipette project.**
The documentation and CAD files are keep in a version controlled online repository
that enables anyone to download and print a pipette. This platform also allows the
interactive viewing of STL files.

4.3 Droplet Encapsulation and Transformation of *S. pneumoniae* On-chip

4.3.1 Droplet Production with Culture Media

Moving from Water to Culture Medium Droplet production of water in oil (w/o)
droplets was easier than media in oil. This could be due to one or more components in
the media that may tip the solution to be more hydrophobic in nature. M9, a minimal
growth media typically used for culturing *E. Coli*, was noticeably more water-like com-
pared to the more syrupy CDM, LB, and CAT media. These qualitative observations
of different media properties lead to experimenting with dilutions of CDM in M9 that
were ultimately a success. Coating of the channels with a hydrophbic surface coating

(Novec 1720, 3M) resulted in droplet formation with a solution of up to a 20% dilution of CDM in M9 although fouling eventually occurred after ∼30 minutes of droplet generation. This fouling of the hydrophobic surface treatment and wetting of areas by the dispersed phase downstream of the generating region could be caused by adsorption of media components or adherence of cells to the channel walls. Adherence of chains of cells to channel walls was observed in upstream areas of the device (Figure 3.8). The wetting of channel walls downstream of the generating neck, from the dispersed phase, caused the droplet break-up mode to shift from monodisperse dripping to jetting. When this happened, the dispersed phase flow stream invaded far past the droplet generating neck, which produced large polydisperse droplets.

Filling and Draining the Incubation Chamber with Droplets   The 6.5 μm volume of the droplet device could be filled with droplets in ∼20 minutes once droplet formation stabilized. After the 30 minute incubation at 37 °C for transformation, the droplets could be successfully flowed out of the device although this process was not very quick or efficient. The oil moved through the device, but flowed around droplets bunched in the middle of the chamber. This required flowing more oil for longer time to push out all the droplets. This also results in droplets being suspended in an excess of oil, which may cause them to evaporate in the tubing before the emulsion breaking step. A better designed chamber or process that allows quick unloading of droplets should be considered for future experiments. Possibly using CAT media to push out the oil and suspended droplets would work better, rather than using more oil.

Options for Droplet Generation with Rich Medium   Conveniently, transformation was successful in M9 medium so droplet encapsulation experiments could proceed. Despite this, it would be ideal to be able to perform encapsulation with various rich media in the future. Other droplet formation geometries may be able to successfully make droplets using CDM or rich media. Non-planar geometries such as 3D axisymmetric designs would be good candidates for this as they avoid any unintentional wetting of areas with the dispersed phase[178]. These devices are more complicated to fabricate as they involve aligning pulled microcapillaries in the center of channels. For these preliminary studies we elected for the simpler, reproducible planar lithography based geometries,

but more involved designs should be considered if it results in more freedom of media choices.

4.3.2 Imaging of Cells in Droplets

Fluorescence Imaging   Cells could be successfully imaged in the device's incubation chamber although quality was improved when imaging through a glass coverslip. Cells could be observed with phase contrast and RFP modes but no GFP signal was detected. It seemed that all cells that appeared with phase contrast also produced a RFP signal. This may be due to some natural autofluorescence properties of the cells or a mistaken addition of the RFP gene to both strains. This could also indicate that the GFP labeled CP2215 victim strain is already lysed by the time imaging is performed. This would add evidence to observation that CP2215 did not survive the encapsulation process (Table 3.5). An additional degree of difficultly in detecting fluorescence signal was due to the motion of the cells. Imaging the moving cells required a higher excitation laser power to detect the fluorescence signal. This also lead to significant photobleaching of the signal which is apparent in time lapse acquisitions. The fluorescence properties of these strains should be independently verified by imaging larger colonies, perhaps is as biofilm [154]. While fluorescence protein expressing cells would be more convenient to work with, another possibility would be to manually stain the cells during their growth stage (using BacLight Bacterial Stain). Excess stain could be washed from the pellet before resuspending in M9 medium.

Cell Occupancy Distribution   Counts of cells per droplet produced a random distribution of cells in accordance to the Poisson distribution, as expected. One to five cells were observed occupying each droplet with an average of 2.5 cells per droplet and the mode of 2 cells per droplet. These results come close to the goal of the project which is to isolate individual pairs of droplets. Ideally no droplets would contain more than 2 cells. To achieve this a higher ratio of droplets to cells is required. This can be accomplished by decreasing the cell concentration or decreasing the size of the droplets (thereby making them more numerous if the volume is kept constant). The average droplet size was estimated to be 16 um which is larger than the target size of 10 or less. Tuning the droplet size closer to 10 would shift occupancy distribution in a more

favorable direction for this projects goals. Should a higher than random frequency of 2 cells per droplet be desired in the future methods can be explored such as inertial flow focusing[179, 180] or or droplet sorting methods[167].

Estimation of Droplet Size   The size of the droplets was estimated by using cells as a frame of reference. Cells were assumed to be 1 μm in length for individual cells or 2 μm in length for diplococci. After measuring several cell/droplet images, the average droplet diameter was then estimated to be 16 μm. The volume was then calculated assuming the droplets were deformed into an ellipsoid shape due to the 10 μm height of the channels. Using these calculations, the average volume of a droplet was estimated to be $1.5E^{-9}$ mL^3. This corresponds to a cell density of $1.6E^9$ cells/mL^3, which agrees with 1.0 OD measurement. The coefficient of variation (CV) was calculated to be 68%. Monodisperse is considered to have a CV of less than 5%. Using the cell size as a frame of reference is not ideal because the error is large when measuring a small one μm cell and this error scales when applied to measuring the much larger droplet sizes. In addition, it is not clear exactly where the edges of the droplet are and if they were even measured accurately due to the plane of focus. Future devices can include features that are on the order of desired droplet sizes to serve as a better size reference for measuring.

Prevention of Evaporation of Droplets   The addition of the coverslip to the incubation chamber was critical in preventing evaporation of the droplets. This shielded the incubation chamber above and below with a gas impermeable glass layer. In the absence of the coverslip, droplets would shrink in size and eventually disappear completely in less than 20 minutes. This is due to high gas permeability of PDMS[18]. To avoid the additional step of adding a coverslip layer, fabrication of chips with hard plastic or glass could be considered or even coating the inside of the PDMS with Parylene[1] would prevent evaporation.

FTIR Imaging of DNA in *E. coli*   FTIR imaging confirmed that DNA was confined to the cell within droplets, but in the presence of lysis buffer, DNA was released and spread throughout the droplet. This experiment suggests that DNA is distributed throughout the droplet after lysis and should be available for uptake by a competent cell. Released DNA is also contained within the droplet and did not escape into the oil

carrier phase. Perhaps future experiments can be conducted with *S. pneumoniae* and timed properly to observe cell-cell attack and lysis.

4.3.3 Bulk Transformation *vs.* Droplet Encapsulated

Transformation between strain CP2204 and CP2215 in bulk media was tested in many conditions. Transformation efficiency at high OD needed to be confirmed because estimated cell density required to achieve 2 cells per $\sim$10 μm droplets, which was higher than typical liquid transformation studies. There was concern that cell densities higher than 0.3 OD would cause stress that would negatively influence transformation efficiency. Successful transformation at up to OD 1.0 in M9 minimal media was demonstrated without significant effect to transformation efficiency. Controls were also performed to demonstrate that transformation only occurred in the presence of CSP and only in the presence of both strains (Table 3.3).

Transformation of Encapsulated Cells   With high density tests in M9 a success, encapsulation experiments could proceed. For these experiments one sample of cell mix (CP2204 and CP2215 in equal parts) was encapsulated in droplets and a sample of cell mix was keep as a bulk suspension to serve as the control. The cells were encapsulated with inducer in a 4°C room, a process that took $\sim$1 hour. CSP was also added to the control cells then both samples were incubated at 37°C for 30 minutes to allow transformation. After the 30 minutes incubation, both samples were returned to the cold room while droplets were pushed out of the incubation chamber, a process that took $\sim$ 1 hour. Emulsion breaking was done on the lab bench at room temperature. Both samples were diluted by 100-fold into CAT medium and incubated for 1 hour before further dilution and plating. Unfortunately, this protocol yielded no transformants for both the encapsulated and control sample. For the droplet encapsulated cells, counts of Rif^R CFUs were 10^4-fold lower than expected and zero Spc^R strains were observed. The control sample counts for Rif^R were only slightly attenuated, but the counts for the Spc^R were 10^3-fold lower than expected. This procedure was repeated three more times with similar results (Table 3.5, Figure 4.2).

CP2215 (the designated donor or victim) did not survive the encapsulation reaction and the non-encapsulated control counts were significantly attenuated in a range from
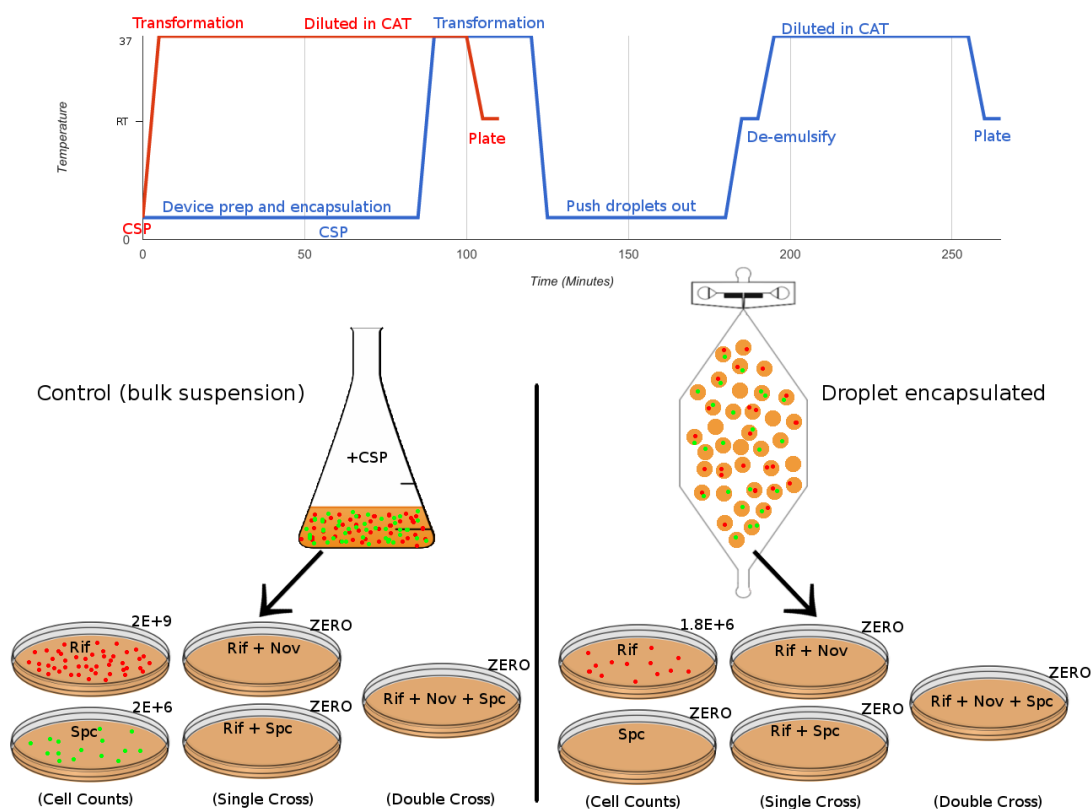
FIGURE 4.2: **Illustration of cell encapsulation experiments.** The time course of the encapsulation protocol is show above and is plotted with along side a typical bulk transformation protocol time course. Below is and illustration of the control sample (left) and the experiment sample (right) which is encapsulated.

$\sim 10^5$ to $\sim 10^6$ cells/mL. These counts are $\sim 10^3$-fold lower than expected *vs.* the results of initial testing in M9 (Table 3.3) and quick emulsion experiments (Table 3.6). In addition, no transformation was observed in either the encapsulated reactions or the non-encapsulated controls. Had these low cell counts only affected the encapsulated sample, the assumption would be that some stage of the encapsulation or emulsion breaking process was stressing or killing the cells, but it seems that even the control condition affected the viability of CP2215, as well as not providing the proper conditions for transformation.

Testing with "Quick" Emulsion in M9 and CDM   Further testing experiments were done to determine if the emulsion or emulsion breaking process may be affecting the cells as well as the difference between CDM and M9. Quick emulsions were made by vortexing cell suspensions with oil. This was done with cells suspended in M9 and CDM. The results of this experiment were acceptable cells counts for both strains and conditions as well as transformation for each condition (Table 3.6). The potentially

critical difference between these tests and the encapsulation procedures is the amount of time that cells are held in M9. The encapsulation process takes at least ∼45 minutes and is done in the cold room whereas the quick emulsion was made in seconds at the lab bench at room temperature. Also flowing out of the droplets takes an additional ∼1 hour and is also done in the cold room. The quick emulsion control reaction could immediately proceed to the emulsion breaking step after the ∼ 30 minute transformation. The total time that cells are kept in M9 is about 2 hours longer during encapsulation experiments. Even though most of this time the cells are kept chilled it seems likely that it induces considerable stress resulting in lower cell viability and no transformation.

4.3.4   Future Directions

Tests that can be immediately performed include determining the viability of cells suspended in M9 for extended periods of up to two or three hours. These tests should be done with and without the inducer cocktail as well. If these tests demonstrate that cells do not survive or do not undergo transformation during extended time on M9, the encapsulation procedure could be shortened. Currently the goal is to produce ∼5 μL of emulsion which is a large enough volume to confidently transfer with a micropipette. The device can be designed with a much smaller sized incubation chamber or even no on-chip incubation chamber at all. A smaller amount of droplets can be generated quickly and then immediately flowed off chip into gas impermeable tubing. The droplets can then be incubated in the tubing and then immediately dispensed into a centrifuge tube for the emulsion breaking process where cells are diluted into CAT medium. This will significantly reduce the amount of time that cells spend in M9 hopefully increasing viability and transformation.

Independent Test of Attacker Strain   A positive note is that CP2204, the attacker strain, does survive the encapsulation and emulsion breaking procedures. It's possible that some condition is causing the victim strain, CP2215, to die yet not release its DNA. The attacker strain can be independently tested to see if it is still able to transform in these conditions by adding some known donor DNA into the suspension.

Chip Fabrication for Improving Imaging   In addition to designing devices to work more quickly with smaller volumes of droplets, devices for better imaging of droplets can be designed. Devices with coverslip bottom rather than a 1 mm thick glass slide will enable better imaging with close working distance oil immersion objectives. Fabrication of coverslip bottom devices will have to take into account incorporating two brittle coverslip layers. An additional concern is that PDMS and glass expand to different degrees during changes in temperature. PDMS expands and contracts significantly due to changes in temperature yet when it is bonded to a glass slide it is held flat. More flexible coverslips will warp due to the expansion and contraction of PDMS, which complicates imaging with close working objectives.

Conclusion

This thesis has presented the design and development of three devices for the study of biological systems: A 3D printed oxygen control insert for a 24-well plate, a 3D-printable micropipette, and a microfluidic droplet generating device for the encapsulation and observation of gene transfer between pairs of cells.

3D printing microfluidic chips have been limited to oxygen-impermeable materials. We demonstrate oxygen control in 3D-printed devices with the addition of a gas permeable PDMS membrane. Oxygen control was demonstrated in a 24-well plate, and PCR detection of upregulation of VEGFA mRNA in A549 cells shows that the device effectively controls oxygen as expected. 3D printing allows complex designs, integrated tubing connectors, and is comparable in price to standard PDMS fabrication. This technique represents a bridge to commercialization where robust devices can be more easily shared and disseminated. While injection molding, hot embossing, or other industrial processes are cheaper when making hundreds to thousands of devices, it is not practical to make an injection mold when making tens to hundreds of devices. In addition, PDMS fabrication would be too time consuming, expensive, and the failure rate would be unacceptable. 3D printing is an excellent solution to these device fabrication needs.

We have also presented an open design micropipette that uses 3D-printable parts in addition to a disposable syringe and a few easily sourced pieces of hardware. Our open design pipette is novel in that it allows the user to set the pipette to the desired

volume without the need to calibrate or verify with a weighing scale. We validated the accuracy and precision of our pipette and developed a new graduation scale to correct for the use of the syringe for air-displacement measurements that meets the ISO standard for adjustable pipettes. Our design is free to use and modify to encourage further collaborative development.

Finally, we have demonstrated a method of encapsulating *S. pneumoniae* in droplets of minimal media with a planar flow focusing device but additional methods must be explored to produce droplets of rich media. The addition of a coverslip layer prevents evaporation of droplets which allows incubation and imaging of encapsulated cells. Imaging of the droplets showed an average of 2.5 cells per droplet and mode of 2 cells per droplet. Further testing must be performed to develop a protocol to assay for transformation of encapsulated cells.

Appendix A

Media Recipes

TABLE A.1: Formula for M9 medium.

	Component	Common Name	Concentration (mg/L)
1. M9 salts	$Na_2HPO_4 \cdot 7\,H_2O$	Sodium Monohydrogen Phosphate Heptahydrate	12800
	KH_2PO_4	Monopotassium phosphate	3000
	NaCl	Sodium chloride	500
	NH_4Cl	Ammonium chloride	1000
2. Carbon source	Glucose	Glucose	4000
3. Additional salts	$CaCl_2$	Calcium chloride	11.1
	$MgSO_4$	Magnesium sulfate	240

TABLE A.2: Formula for chemically defined medium (CDM).

	Component	Common Name	Concentration (mg/L)
1. Mineral salts	$FeSO_4 \cdot 7\,H_2O$	Iron(II) sulfate heptahydrate	5
	$Fe(NO_3)_2 \cdot 9\,H_2O$	Iron(III) nitrate nonahydrate	1
	K_2HPO_4	Dipotassium phosphate	200
	KH_2PO_4	Monopotassium phosphate	1000
	$MgSO_4 \cdot 7\,H_2O$	Magnesium sulfate heptahydrate	700
	$MnSO_4$	Manganese(II) sulfate	5
2. Amino Acids	DL-Alanine	Alanine (racemic)	100
	L-Arginine	Arginine	100
	L-Aspartic acid	Aspartic acid	100
	L-Cystine	Cystine	50
	L-Glutamic acid	Glutamic acid	100
	L-Glutamine	Glutamine	200
	Glycine	Glycine	100
	L-Histidine	Histidine	100
	L-Isoleucine	Isoleucine	100
	L-Leucine	Leucine	100
	L-Lysine	Lysine	100
	L-methionine	Methionine	100
	L-phenylalanine	Phenylalanine	100
	L-Proline	Proline	100
	Hydroxy-L-proline	Hydroxyproline	100
	L-Serine	Serine	100
	L-Threonine	Threonine	200
	L-Tryptophan	Tryptophan	100
	L-Valine	Valine	100
3. Vitamins	p-Aminobenzoic acid	para-aminobenzoic	0.2
	Biotin	Biotin	0.2
	Folic acid	Folic acid	0.8
	Niacinamide	Niacinamide	1
	β-Nicotinamide adenine dinucleotide	NAD+/NADH	2.5
	Pantothenate calcium salt	Calcium Pantothenate	2
	Pyridoxal	Pyridoxal	1
	Pyridoxamine dihydrochloride	Pyridoxamine (source of B6)	1
	Riboflavin	Riboflavin (B2)	2
	Thiamine hydrochloride	Thiamine (B1)	1
	Vitamin B12	Vitamin B12	0.1
4. Sugar	Glucose	Glucose	10000
5. Nucleobases	Adenine	Adenine	20
	Guanine hydrochloride	Guanine hydrochloride	20
	Uracil	Uracil	20
6. Salts	$CaCl_2 \cdot 6\,H_2O$	Calcium Chloride Hexahydrate	10
	$NaC_2H_3O_2 \cdot 3\,H_2O$	Sodium Acetate Trihydrate	4500
	L-Cysteine	Cysteine	500
	$NaHCO_3$	Sodium bicarbonate	2500
	$NaH_2PO_4 \cdot H_2O$	Sodium dihydrogen phosphate monohydrate	3195
	Na_2HPO_4	Disodium phosphate	7350

TABLE A.3: Formula for inducer cocktail.

Component	Stock	unit	Inducer
CSP	250	μg/mL	0.1
BSA	4	%	0.004*
CaCl2	1	M	0.005

*typically 0.04% BSA is used to prevent non-specific binding but was reduced in these experiments to prevent fouling of they hydrophobic droplet generator

TABLE A.4: Concentration for drug agar overlay.

Drug	Overlay	Stock
Rifampin	40 μg/mL	20 mg/mL
Novobiocin	10 μg/mL	10 mg/mL
Spectinomycin	160 μg/mL	100 mg/mL

This concentration assumes a 3 mL overlay layer with a 12 mL total volume per plate.

Appendix B

Supplementary Information

3000μl
2000μl
1000μl
0μl
1cm
1in

1000µl
900µl
800µl
700µl
600µl
500µl
400µl
300µl
200µl
100 µl
0 µl

1 cm

1 in.
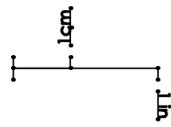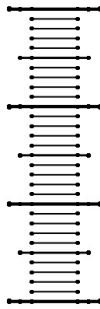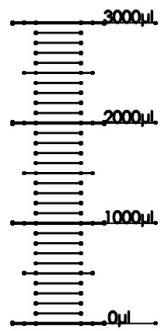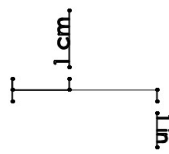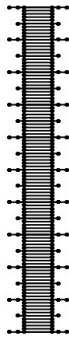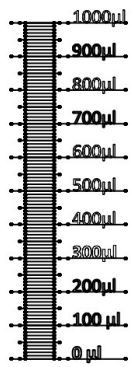
Molding of Gas Permeable Membranes.

1. Place a sheet of foil on a hot plate.

2. Place a 6-inch square 1/4-inch thick glass plate on foil.

3. Put two layers of scotch tape on the left and right edges of the glass (should give a 100 um spacing).

4. Pour on ~5 mL 10:1 mixed and degassed PDMS in center of the plate.

5. Roll on transparency sheet so as not to make bubbles.

6. Place second 6-inch 1/4-inch glass plate on top of the transparency.

7. Place a weight on top of the whole assembly to compress.

8. Fold the foil around the plates to prevent them from sliding around and the PDMS from dripping.

9. Set the hot plate to 50 °C and bake for ~4+ hours. (Any warmer and bubbles will spontaneously appear in PDMS, and the transparency may warp.)

10. Disassemble the mold and transfer it to a transparency to cut out membranes.

11. Spread on some uncured PDMS to act as a glue and then cut out and place on each pillar.

12. Place the transparency over a printed out template of 24 circles and cut manually.

13. Let the PDMS cure overnight at room temperature.

14. The next day, apply more PDMS around the edge of the pillars to caulk the edge where the membrane and pillar meet, and let PDMS cure overnight again.

15. Test the device by placing it in a 24-well plate that is filled with DI water. After a few minutes any leaks will be evident as the pillar will be flooded with water.

16. Remove the water from the inside of the device by placing it in a vacuum desiccator and allowing the water to evaporate.

17. Patch the leaks with more PDMS or by replacing the membrane if needed.

Quick Protocol Overview

1. Export a complete, joined design to dxf file
2. Convert with linkCad
3. Upload design to uPG software
4. Load wafer ready to be exposed
5. Expose

CAD design

The design must have no overlapping lines. The best way to check for this is to make sure that everything joins properly. You can also select and delete parts of the design to see if any stray lines are hidden under your design.

You do not want to have any borders or outlines that are a single line (such as wafer boundaries). The uPG will print everything starting at the outermost line.

Center your design. The X-Y origin should be the center of your design.

The uPG passes over the entire area of the design regardless of whether there are gaps between areas. It writes vertical lines (y-direction) and then moves over one position in the x direction. The time your design takes to write depends on how many vertical lines the uPG needs to scan. So it is best to align your designs to take up the least amount of space in the x-direction.

For example, B M L takes more time the BML, but both of these examples would take at least 3 times more write time as:

B

M

L

Conversion with LinkCAD

The uPG software cannot see features within features. It exposes everything inside the outermost line. LinkCad tricks the uPG into printing features within features by cleverly cutting design into smaller separate adjacent parts.

1. Save your design as a dxf formatted file.
2. Open linkCad. Leave the import and export formats as DXF. Note: dxf format has no scale information so it asks you to enter it. Give it whatever scale you are using in your dwg file. Typically 1 unit = 1 mm. Scale 1 times. Set the exports units the same.

3. Browse to and import your dxf file.

4. Typically you will have a number of open polygons. Check "join adjacent open polygons" and "Close open polygons" and click repair.

5. Click view at the top of the screen, and turn fill on (it looks like a "%" sign in the tool bar) to help visualize what will be exposed. Areas that are to be exposed are filled in with gray. You'll notice that features within features are filled in twice. We will fix that in the next step.

6. Go to Tools > De-Embed Polygons. Depending on the geometry of you design on option may work better. Usually "Cut-line in re-entrant polygons" works.

7. Now you should see the preview with you design in gray with no double exposed areas. If it doesn't look right most likely there is an un-joined or overlapping line in your original design. Problem areas are usually highlighted with a triangle.

8. Go back to the convert tab and click next. A few open remaining polygons are OK as long as the preview looked good.

9. Click next again and save the converted dxf. It's best to use a new file name indicating that it is converted.

Converting Designs with Arrays

If you design includes any array it is usually too complex for the De-embed polygon function. For arrays you will add it as a second file during the conversion process.

1. Save the array separately from the main design. You must insure that the array lines up with the main design. The easiest way to do this is to create the whole design with the array and save as two different files. Then delete the array in one file, and everything but the array in the second file.

2. Proceed as above with the main file (minus arrays). After you De-Embed polygons you will subtract the array from the first file.

3. Go to Tools > Boolean Operations on Files.

4. Select the array as "File (B)". The select A minus B (subtract). Leave Explode cells checked. The precision can be 10 nm or lower.

5. Your array should be successfully cut out from the design.

6. If your array contains a large number of elements the preview may freeze when you try to zoom in to check. You can check a small portion by using the window-drawing-zoom option rather than incrementally zooming in. The to return click the zoom to full image option. You should see the array elements in white (if they are intended to be pillars) and cuts going out.

Setting up the uPG for exposure

You will want to have a wafer ready with SU-8, softbakeing.

1. Turn on the compressor and vacuum pump.

2. Start the uPG exposure wizard software and load the design. If you used 1 unit = 1 mm in

the LinkCAD conversion then you want to scale by 1000000.

3. The preview is useless. Don't worry if there is a large black filled in part. What is important to check is the overall design dimensions. This is the actual size that it will print as. Compare them to your design. If they are off something was scaled wrong. Also check the centering. A few microns off is OK but if there is a significant offset it may print off the wafer.

4. Click show control panel and click 'To Load' in the resulting window.

5. Get your wafer ready by using a razor to scrape off any SU-8 from the bottom or use a moist kimwipe with acetone and clean the bottom and then blow off any debris.

6. Use the aligning pins to center the wafer on the stage and turn on the vacuum with the blue switch.

7. Remove the aligning pins and click 'To Center'. Next click focus.

8. Exposure settings depend on the thickness of your SU-8. The highest energy for one pass is 18 MW at 99% strength and 4X time. If your SU-8 is 20 micrometer one pass at these settings should be good. For small features (less than 15um), unidirectional mode should have a check mark. If your design is taller or shorter you will need to run multiple passes or increase the speed (3x 2x or 1x) or decrease exposure energy. You can tell if your design is over exposed if the surface of the cured SU-8 has a cracked appearance. SU-8 under 20 micrometers also has a good chance of peeling away when it is developed. One solution for this is to do a post-post exposure bake at 120C before developing. Another option is to spin and cure a thin layer of SU-8 (like SU-8 2002 @ 2000 rpm) on the wafer before spinning the design layer. This helps the design layer adhere.

9. Expose X number of times (use team-viewer to run again remotely).

Multi-Layer Masters

1. expose the first layer as above, align the wafer with the pins in a way that you can place it again on the stage in approximately the same way. Usually you can place the of the corners of straight edges at a pin.

2. Complementary alignment marks must be added to each layer of the design. Place the distinct feature of the alignment marks at an integer coordinate as it is easier to type in later. Alignment marks placed at 12 O'clock, and 6 O'clock will not add any write time for the design.

3. Use the advanced alignment with the exposure wizard.

4. Check the mark1 and mark2 and enter the coordinates of the distinct feature

5. A green cross-hairs will appear with a live camera image of the wafer. If you were lucky enough to place the wafer in close to the same position than you should see you alignment mark. Move the stage or the cross-hairs to the location that corresponds to the coordinates and click the middle mouse button(scroll wheel)

6. You will be prompted to do the same for the second alignment mark.

7. Finally it will give you a report telling you how much it will compensate for re-alignment. If these numbers seem odd you may have switch alignment marks.

Masters of around 10 um in height and smaller have a special issues with alignment because

total internal reflection causes the marks to be invisible through the camera (you're not crazy). The solution is to selectively wash away the SU-8 around the alignment mark. Take a q-tip sponge and wet it with developer. The carefully wash away the SU-8 from around the alignment mark. You must place the alignment mark far enough away from the design so that you avoid washing away areas of the design.

Checklist

- [ ] Is the design joined with no overlapping lines or wafer outlines?
- [ ] Do the dimensions in the preview of the uPG make sense?
- [ ] Did you scrape SU-8 off the back of the wafer before loading?
- [ ] Did you remove the alignment pins after you loaded the wafer?
- [ ] Is team-viewer running if a second exposure is needed?

Cell-cell Attack and Gene Transfer

Testing Transformation in M9 with Controls

Sep 12 2016

Cell cultures

Attacker: CP2204 Rif-r Nov-s Sp-s. Stock 4/15/16. OD 0.2 BoxMorrison2016#1-20.

Victim: Cp2215 Nov-r Sp-r. Stock 4/15/16 OD 0.2 BoxMorrison2016#21-40

Thaw Stock cells @ 0C. Dilute for growth in CDM + 1%CAT 12mL/tube.

Media batch CAT:9/6/16 (yuri), CDM+CHO+G:9/12/16

To CAT from stock shelf add phosphate and glucose. For 300 mL CAT add 10 mL 0.5 M K2HPO4 (sterile filtered) and 3 mL 20% glucose (sterile filtered).

Grow to OD = 0.3 and chill to 0C for use.

cells	Cp2204	Cp2204	Cp2204	CP2215	CP2215	CP2215
vol	250 uL	100 ul	100 uL	250 uL	100 uL	100 uL
tube	A	B	C	D	E	F
2:20	37C	37C	37C	37C	37C	37C

Attack Reaction

Cell Prep:

At OD 0.3 chill to 0C.

Take 2 x 12 mL tubes of cell suspension and spin down at 8k rcf for 8 min in chilled incubator.

Pour off supernatant and resuspend in 1.1 mL chilled M9 resulting in OD 3.278

Combine cells suspensions to make 2.2 mL suspension, each strain at OD 1.63, hold at 0C.

Reaction Scheme:

Each reaction has cells of each strain at OD = 1.0 and the same inducer concentration.

Prepare reaction tubes according to following scheme. First add CDM, then M9 then inducer to each tube and finally cells. Mix/vortex tubes and gently centrifuge to bottom.

Rx	%M9	%CDM	Inducer	CP2204	CP2215
1	80	20	w	w	w
2	100	0	w	w	w
3	80	20	w/o	w	w
4	100	0	w/o	w	w
5	80	20	w	w	w/o
6	80	20	w	w/o	w

Rx	M9	CDM	Inducer	Cell Mix	CP2204	CP2215
1	0	120	114	366	–	–
2	120	0	114	366	–	–

Rx	M9	CDM	Inducer	Cell Mix	CP2204	CP2215
3	0	120	0	366	–	–
4	120	0	0	366	–	–
5	120	0	114	–	366	w/o
6	120	0	114	–	w/o	366

Inducer Prep:

component	Stock	Inducer	Dilute by	working stock	Vol/RX	Total (4.2x(Vol/RX))
CSP	250 ug/mL	0.2 ug/mL*	50	5 ug/mL	24 uL	100.8 uL
BSA	4%	0.04%	10	0.4%	60 uL	252 uL
CaCl2	1 M	5 mM	10	100 mM	30 uL	126 uL

typically 0.1 ug/mL of CSP is used, it was doubled in this case to encourage transformation

Preparing Working Stocks:

Working Stocks	Stock	M9	dH2O
CSP	25 uL	1 mL	–
BSA	100 uL	1 mL	–
CaCl2	100 uL	–	1 mL

Put reaction tubes in heat block at 37C for **35 minutes**. *reaction started at:*

After 30 min reaction the 600 uL reaction mixture was diluted into 6 mL CAT and incubated at 37C for 60 minutes. *Incubation started at:*

Dilution Scheme

2 mL open tubes were used: 108 total tubes

150 uL from reacion tube pippetted into 4 1.5 mL tubes and incubated for 1 hr. = 10E-1 Plated RNS

150 uL was pipetted into 7 tubes of 1.5 mL = 10E-2 Plated RN and RS

15 uL pipetted into 1.5 mL = 10E-4 do not plate

15 uL pipetted into 1.5 mL = 10E-6 6 tubes plated with R and S

Plates are filled with:

1. 3 mL CAT agar
2. 1.5 mL cells + 1.5 mL agar
3. 3 mL CAT agar
4. 3 mL Drug agar

Drug Assay Prep

Drug	overlay	Stock
R	40 ug/mL	20 mg/mL
N	10 ug/mL	10 mg/mL
S	160	100 mg/mL

Agar	Total Plates	Volume Agar	R	N	S
R	15	55 mL	111 uL	–	–
S	15	55 mL	–	–	88 uL
RN	15	55 mL	111 uL	55 uL	–

Agar	Total Plates	Volume Agar	R	N	S
RS	15	55 mL	111 uL	–	88 uL
RNS	15	55 mL	111 uL	55 uL	88 uL

Results

Cell Counts Cells/mL

RX	Dilution	Colonies	squares	squares/plate	colonies/plate	Drug	Cells/ml
1	1.00E-06	91	1	4	364	R	2.43E+08
1	1.00E-06	82	1	4	328	R	2.19E+08
1	1.00E-06	69	1	4	276	R	1.84E+08
1	1.00E-06	52	3	100	1733.333333	R-small	1.16E+09
1	1.00E-06	42	3	100	1400	R-small	9.33E+08
1	1.00E-06	46	3	100	1533.333333	R-small	1.02E+09
1	1.00E-06	88	1	4	352	S	2.35E+08
1	1.00E-06	117	1	4	468	S	3.12E+08
1	1.00E-06	102	1	4	408	S	2.72E+08
1	1.00E-02	119	3	20	793.3333333	RN	5.29E+04
1	1.00E-02	73	3	20	486.6666667	RN	3.24E+04
1	1.00E-02	95	3	20	633.3333333	RN	4.22E+04
1	1.00E-02	297	3	100	9900	RN-small	6.60E+05
1	1.00E-02	273	3	100	9100	RN-small	6.07E+05
1	1.00E-02	234	3	100	7800	RN-small	5.20E+05
1	1.00E-02	67	3	20	446.6666667	RS	2.98E+04
1	1.00E-02	65	3	20	433.3333333	RS	2.89E+04
1	1.00E-02	66	3	20	440	RS	2.93E+04
1	1.00E-02	130	3	370	16033.33333	RS-small	1.07E+06
1	1.00E-02	169	3	370	20843.33333	RS-small	1.39E+06
1	1.00E-02	121	3	370	14923.33333	RS-small	9.95E+05
1	1.00E-01				16	RNS	106.67
1	1.00E-01				7	RNS	46.67
1	1.00E-01				6	RNS	40.00
2	1.00E-06	68	1	4	272	R	1.81E+08
2	1.00E-06	117	1	4	468	R	3.12E+08
2	1.00E-06	80	1	4	320	R	2.13E+08
2	1.00E-06	80	1	4	320	S	2.13E+08
2	1.00E-06	77	1	4	308	S	2.05E+08
2	1.00E-06	105	1	4	420	S	2.80E+08
2	1.00E-02	77	3	20	513.3333333	RN	3.42E+04

RX	Dilution	Colonies	squares	squares/plate	colonies/plate	Drug	Cells/ml
2	1.00E-02	77	3	20	513.3333333	RN	3.42E+04
2	1.00E-02	77	3	29	744.3333333	RN	4.96E+04
2	1.00E-02	69	3	370	8510	RN-small	5.67E+05
2	1.00E-02	79	3	370	9743.333333	RN-small	6.50E+05
2	1.00E-02	64	3	370	7893.333333	RN-small	5.26E+05
2	1.00E-02	57	3	20	513.3333333	RS	3.42E+04
2	1.00E-02	54	3	20	380	RS	2.53E+04
2	1.00E-02	56	3	20	360	RS	2.40E+04
2	1.00E-02	121	3	370	14923.33333	RS-small	9.95E+05
2	1.00E-02	110	3	370	13566.66667	RS-small	9.04E+05
2	1.00E-02	133	3	370	16403.33333	RS-small	1.09E+06
2	1.00E-01				6	RNS	4.00E+01
2	1.00E-01				3	RNS	2.00E+01
2	1.00E-01				7	RNS	4.67E+01
3	1.00E-06	123	3	40	1640	R	1.09E+09
3	1.00E-06	117	3	40	1560	R	1.04E+09
3	1.00E-06	130	1	40	5200	R	3.47E+09
3	1.00E-06	69	1	4	276	S	1.84E+08
3	1.00E-06	95	1	4	380	S	2.53E+08
3	1.00E-06	65	1	4	260	S	1.73E+08
3	1.00E-02				0	RN	0.00E+00
3	1.00E-02				0	RN	0.00E+00
3	1.00E-02				0	RN	0.00E+00
3	1.00E-02				0	RS	0.00E+00
3	1.00E-02				0	RS	0.00E+00
3	1.00E-02				0	RS	0.00E+00
3	1.00E-01				0	RNS	0.00E+00
3	1.00E-01				0	RNS	0.00E+00
3	1.00E-01				0	RNS	0.00E+00
4	1.00E-06	104	3	40	1386.666667	R	9.24E+08
4	1.00E-06	94	3	40	1253.333333	R	8.36E+08
4	1.00E-06	80	3	40	1066.666667	R	7.11E+08
4	1.00E-06	67	1	4	268	S	1.79E+08
4	1.00E-06	74	1	4	296	S	1.97E+08
4	1.00E-06	97	1	4	388	S	2.59E+08
4	1.00E-02				0	RN	0.00E+00

RX	Dilution	Colonies	squares	squares/plate	colonies/plate	Drug	Cells/ml
4	1.00E-02				0	RN	0.00E+00
4	1.00E-02				1	RN	6.67E+01
4	1.00E-02				1	RS	6.67E+01
4	1.00E-02				0	RS	0.00E+00
4	1.00E-02				0	RS	0.00E+00
4	1.00E-01				0	RNS	0.00E+00
4	1.00E-01				0	RNS	0.00E+00
4	1.00E-01				0	RNS	0.00E+00
5	1.00E-06				0	R	0.00E+00
5	1.00E-06				0	R	0.00E+00
5	1.00E-06				0	R	0.00E+00
5	1.00E-06	87	1	4	348	S	2.32E+08
5	1.00E-06	98	1	4	392	S	2.61E+08
5	1.00E-06	77	1	4	308	S	2.05E+08
5	1.00E-02				0	RN	0.00E+00
5	1.00E-02				0	RN	0.00E+00
5	1.00E-02				0	RN	0.00E+00
5	1.00E-02				0	RS	0.00E+00
5	1.00E-02				0	RS	0.00E+00
5	1.00E-02				0	RS	0.00E+00
5	1.00E-01				0	RNS	0.00E+00
5	1.00E-01				0	RNS	0.00E+00
5	1.00E-01				0	RNS	0.00E+00
6	1.00E-06	208	3	40	2773.333333	R	1.85E+09
6	1.00E-06	219	3	40	2920	R	1.95E+09
6	1.00E-06	181	3	40	2413.333333	R	1.61E+09
6	1.00E-06				2	S	1.33E+06
6	1.00E-06				0	S	0.00E+00
6	1.00E-06				0	S	0.00E+00
6	1.00E-02				0	RN	0.00E+00
6	1.00E-02				0	RN	0.00E+00
6	1.00E-02				0	RN	0.00E+00
6	1.00E-02				0	RS	0.00E+00
6	1.00E-02				0	RS	0.00E+00
6	1.00E-02				0	RS	0.00E+00
6	1.00E-01				0	RNS	0.00E+00

RX	Dilution	Colonies	squares	squares/plate	colonies/plate	Drug	Cells/ml
6	1.00E−01				0	RNS	0.00E+00
6	1.00E−01				0	RNS	0.00E+00

Summary of Results by cell count (cells/mL)

Reaction	CDM	Inducer (CSP)	Cells	Rifampicin (R)	R-Small	Spectinomycin (S)	RN	RN-small	RS	RS-small	RNS
1	20%	+	Mix	2.15E+08	1.04E+09	2.73E+08	4.25E+04	5.96E+05	2.93E+04	1.15E+06	64.44444444
2	0%	+	Mix	2.36E+08	–	2.33E+08	3.94E+04	5.81E+05	2.79E+04	9.98E+05	35.55555556
3	20%	–	Mix	1.87E+09	–	2.04E+08	0	–	0	–	0
4	0%	–	Mix	8.24E+08	–	2.12E+08	0	–	0	–	0
5	20%	+	CP2204	0	–	2.33E+08	0	–	0	–	0
6	20%	+	CP2215	1.80E+09	–	0	0	–	0	–	0

Cell-cell Attack and Transformation in Droplets

March 22 2017

One volume of cells is made into and emulsion with the device and compared to a control volume reacted in bulk suspension. Cells are reacted at OD of 1.0.

Cell cultures:

Strain	Competence	Rifampin	Spectinomycin	Novobiocin	Label
CP2204	inducible w CSP	Resistant	Sensitive	Sensitive	RFP
CP2215	non-competent	Sensitive	Resistant	Resistant	GFP

Thaw Stock cells @ 0C. Stock: box Morrison 2017. Dilute for growth in CDM + 1% CAT 12mL/tube.

For 12 mL growth tubes:	OD
*Resuspend Volume (mL)	0.75
*Desired OD in Reaction	1
Cell mix	2
Each Srain resuspended	4
Grow to	*0.25*

strains:	Cp2204	CP2215
volume seeded:	200 uL	15 uL
9:40	37C	37C
9:40	0.021	0
10:20	0.036	0.01

Attack Reaction

Cell Prep:

For 12 mL growth tubes:	OD
*Resuspend Volume (mL)	0.75
*Desired OD in Reaction	1

For 12 mL growth tubes:		OD
Cell mix		2
Each Srain resuspended		4
Grow to		*0.25*

1. Take 2 x 12 mL tubes of cell suspension and spin down at 8k rcf for 8 min in chilled incubator.

2. Pour off supernatant and resuspend in M9.

3. Combine 350 uL of each strain to make 700 uL cell mix.

4. Pull 350 uL of cell mix into syringe

Inducer Prep:

Produce 700 uL of double strength inducer in M9 and pull 500 uL into a syringe:

cell suspension volume to match	700					
Component	Stock	unit	Inducer	Dilute by	Working Stock	2x inducer
CSP	250	ug/mL	0.1	50	5	28
BSA	4	%	0.004*	10	0.4	14
CaCl2	1	M	0.005	10	0.1	70
M9						588

typically 0.04 % of BSA is used, it was reduced to prevent fouling of hydrophobic device

Preparing Working Stocks:

Working Stocks	Stock	M9	dH2O
CSP	25 uL	1 mL	–
BSA	100 uL	1 mL	–
CaCl2	100 uL	–	1 mL

M9 Media	1000 mL	10 mL M9
dH20 mL	700	7
M9 Salts mL	200	2
20% glucose mL	20	0.2
MgSO4 mL	2	0.02
CaCl2 uL	100	1*

10 uL can be added from the diluted inducer stock rather than 1 ul from standard stock

Reaction Scheme:

Droplet production was performed in the cold room. When cells combine with inducer in droplet device they will be diluted to OD of 1 each. The remaining cell mix and inducer was kept in the cold room to be combined as a control. After the device chamber is full of emulsion the heated stage is turned to 37C, and the control cells are placed in a heated block.

The entire chamber is not full of droplets. The generator failed about half-way through. A long 'string' of fouled area formed causing jetting rather then nice droplet formation. Flow rate of 50 ul/h was used for oil and 10 uL/h for the aqueous.

reaction started at: 3:20

Emlusion Breaking

Emulsion is flowed from the device after 30 min into a centrifuge tube. Both reaction tubes were taken out and placed at room temperature while emulsion breaking was performed.

1. Starting with emlusion add 200 uL CAT

2. Spin down for 30 seconds at 100 x g (in simple centrifuge at heidi's bench)

3. Pipette oil out from bottom

4. add two times volume of pico break and gently rock tube

5. spin again for 1 min at 100-1000 x g

6. pipette out top(cells) ~ 200 uL

Reactions ~200 uL were transfered to another tube tube and brought up to 400 uL with CAT

Reactions were incubated for 60 minutes at 37 C.

Incubation started at:

Dilution Scheme

Assume 4 uL of suspension is extracted from the emulsion.

extracted suspension is brought up to 400 uL = 10^{-2}, (Incubation concentration)

75 uL plated into 3 wells, 10^{-2}, 3xRNS

75 uL transfered into 750 uL CAT to make 10^{-3}, plate 75 uL into 3xRS, 3xRN

75 uL pipetted into 7.5 mL CAT to make 10^{-5}, plate 75 uL into 3xR, 3xS.

Plates are filled with:

24-well plates used:

1. 150 uL CAT agar
2. 75 uL cells + 75 uL agar
3. 150 uL CAT agar
4. 150 uL Drug agar

Drug Assay Prep

Drug	overlay	Stock
R	40 ug/mL	20 mg/mL
N	10 ug/mL	10 mg/mL

Drug	overlay	Stock
S	160	100 mg/mL

Drug	overlay mg/mL	Stock mg/mL	Volume agar mL	pipette mL	ul
R	0.04	20	10	0.02	20
N	0.01	10	10	0.01	10
S	0.16	100	10	0.016	16

Results

Cell Counts Cells/mL

RX	Dilution	Colonies/	squares	squares/plate(MAG)	colonies/plate	Drug	Cells/ml	Ave
1	1.00E-05				0	S	0.00E+00	
1	1.00E-05				0	S	0.00E+00	0.00E+00
1	1.00E-05				0	S	0.00E+00	
1	1.00E-05				1	R	1.33E+06	
1	1.00E-05				0	R	0.00E+00	4.44E+05
1	1.00E-05				0	R	0.00E+00	
1	1.00E-03				0	RN	0.00E+00	
1	1.00E-03				0	RN	0.00E+00	0.00E+00
1	1.00E-03				0	RN	0.00E+00	
1	1.00E-03				0	RS	0.00E+00	
1	1.00E-03				0	RS	0.00E+00	0.00E+00
1	1.00E-03				0	RS	0.00E+00	

RX	Dilution	Colonies/	squares	squares/plate(MAG)	colonies/plate	Drug	Cells/ml	Ave
1	1.00E-02				0	RNS	0.00E+00	
1	1.00E-02				0	RNS	0.00E+00	0.00E+00
1	1.00E-02				0	RNS	0.00E+00	
control	Dilution	Colonies/	squares	squares/plate(MAG)	colonies/plate	Drug	Cells/ml	Ave
2	1.00E-05				2	S	2.67E+06	
2	1.00E-05				0	S	0.00E+00	2.67E+06
2	1.00E-05				4	S	5.33E+06	
2	1.00E-05	15	1	100	1350	R	1.80E+09	
2	1.00E-05	19	1	100	1710	R	2.28E+09	2.48E+09
2	1.00E-05	28	1	100	2520	R	3.36E+09	
2	1.00E-03				0	RN	0.00E+00	
2	1.00E-03				0	RN	0.00E+00	0.00E+00
2	1.00E-03				0	RN	0.00E+00	
2	1.00E-03				0	RS	0.00E+00	
2	1.00E-03				0	RS	0.00E+00	0.00E+00
2	1.00E-03				0	RS	0.00E+00	
2	1.00E-02				0	RNS	0.00E+00	
2	1.00E-02				0	RNS	0.00E+00	0.00E+00
2	1.00E-02				0	RNS	0.00E+00	

Summary of Results by cell count (cells/mL)

March 22 OD: 1	S	R	RN	RS	RNS
droplets	0.00E+00	4.44E+05	0.00E+00	0.00E+00	0.00E+00
control	2.67E+06	2.48E+09	0.00E+00	0.00E+00	0.00E+00

Discussion and Conclusion

No transformation was observed in droplets or in control. No S resistant cells survived (CP2215) droplets. R resistant counts from droplets were also low.

Appendix:

To CAT from stock shelf add phosphate and glucose. For 300 mL CAT add 10 mL of 0.5 M K2HPO4 (sterile filtered) and 3 mL of 20% glucose (sterile filtered).

Appendix C

Code

```
/////////////////////////////
//Set up directories
/////////////////////////////


// Asks for the directory with the Raw MDA data in it and the .md files (the date
    ↪   ex '091514')
direxperiment = getDirectory("Choose the Experiment Directory ");
//print("experiment directory: " + direxperiment);



// Gets the parent path for the directory with the Raw-MDA data
pathmda = File.getParent(direxperiment) + '/raw-mda'
// pathmda = direxperiment + 'raw-mda/'
//print("pathmda: " + pathmda);


// renames the Main directory to raw-mda
File.rename(direxperiment,pathmda);


// makes a directory with the original experiment directory name (the date)
File.makeDirectory(direxperiment);


// moves the raw-mda directory into the experiment directory (the date)
File.rename(pathmda,direxperiment+'raw-mda');


/////////////////////////////////////////////////////
//Stack builder
/////////////////////////////////////////////////////


// Makes directory for the stacks to go
File.makeDirectory(direxperiment+'collected-stacks');
```

```
/////Define paths  for .nd files - optional may change to user input by leaving
    ↪ select blank in stack builder
pathmda = direxperiment+'raw-mda/'
//print("pathmda:" + pathmda);


pathstacks = direxperiment+'collected-stacks'+'/'
//print("pathstacks:" + pathstacks);


// Makes stacks in the stacks folder. You can either enter a path in the the
    ↪ select=, or leave it blank to prompt the user to select the nd files.
// **The macro will quit if the prompt for the nd file is canceled.**
File.makeDirectory(direxperiment+'collected-stacks/zero');
pathzero = direxperiment+'collected-stacks/zero/'
run("Metamorph nd file (stack builder)", "select= all_timepoints all_positions
    ↪ open=[pathzero]"); //pathss
File.makeDirectory(direxperiment+'collected-stacks/one');
pathone = direxperiment+'collected-stacks/one/'
run("Metamorph nd file (stack builder)", "select= all_timepoints all_positions
    ↪ open=[pathone]");
File.makeDirectory(direxperiment+'collected-stacks/seven');
pathseven = direxperiment+'collected-stacks/seven/'
run("Metamorph nd file (stack builder)", "select= all_timepoints all_positions
    ↪ open=[pathseven]");
File.makeDirectory(direxperiment+'collected-stacks/fifteen');
pathfifteen = direxperiment+'collected-stacks/fifteen/'
run("Metamorph nd file (stack builder)", "select= all_timepoints all_positions
    ↪ open=[pathfifteen]");
File.makeDirectory(direxperiment+'collected-stacks/twentyone');
pathtwentyone = direxperiment+'collected-stacks/twentyone/'
run("Metamorph nd file (stack builder)", "select= all_timepoints all_positions
    ↪ open=[pathtwentyone]");
File.makeDirectory(direxperiment+'collected-stacks/exp');
pathexp = direxperiment+'collected-stacks/exp/'
run("Metamorph nd file (stack builder)", "select= all_timepoints all_positions
    ↪ open=[pathexp]");


File.makeDirectory(direxperiment+'collected-stacks/concatenated-stacks');
pathcat = direxperiment+'collected-stacks/concatenated-stacks/'


listzero = getFileList(pathzero)
listone = getFileList(pathone)
listseven = getFileList(pathseven)
listfifteen = getFileList(pathfifteen)
listtwentyone = getFileList(pathtwentyone)
listexp = getFileList(pathexp)


for(j=0; j<listexp.length; j++){
     open(pathzero+listzero[j]);
```

```
        open(pathone+listone[j]);
        open(pathseven+listseven[j]);
        open(pathfifteen+listfifteen[j]);
        open(pathtwentyone+listtwentyone[j]);
        open(pathexp+listexp[j]);
        run("Concatenate...", "all_open title=temp-stack");
        saveAs("Tiff", pathcat+"well"+j+1);
        //run("Close All");
        File.makeDirectory(pathcat+"well"+j+1);
        pathsaveseq = pathcat+"well"+j+1+"/";
        run("Image Sequence... ", "format=TIFF name=sequence start=0 digits=4 save=
    ↪  pathsaveseq");
        input =pathsaveseq;
        listseq= getFileList(pathsaveseq);
        print(listseq.length);
        run("Close All");
        for (k = 0; k < listseq.length; k++) {
            action(input, listseq[k]);
            function action(input, filename) {
            open(input + filename);
            //makeRectangle(473, 155, 106, 110);
            run("Measure");
            close();
            }
        }
        //saveAs("Results", pathcat+"well"+j+1+".csv");
        //run("Clear Results");
        run("Close All");
}
```

CODE C.1: stack-builder.ijm

```
dir= getDirectory("Choose a Directory");
pathzero = dir+'zero/'
pathone = dir+'one/'
// File.makeDirectory('concatenated-stacks')
pathcat = dir+'concatenated-stacks/'
//print(pathexp)

listzero = getFileList(pathzero)
listone = getFileList(pathone)

for(j=0; j<listexp.length; j++){
    open(pathzero+listzero[j]);
    open(pathone+listone[j]);
    run("Concatenate...", "all_open title=temp-stack");
    saveAs("Tiff", pathcat+"well"+j+1);
    //run("Close All");
```

```
    File.makeDirectory(pathcat+"well"+j+1);
    pathsaveseq = pathcat+"well"+j+1+"/";
    run("Image Sequence... ", "format=TIFF name=sequence start=0 digits=4 save=
↪ pathsaveseq");
    input =pathsaveseq;
    listseq= getFileList(pathsaveseq);
    print(listseq.length);
    run("Close All");
    for (k = 0; k < listseq.length; k++) {
        action(input, listseq[k]);
        function action(input, filename) {
        open(input + filename);
        //makeRectangle(473, 155, 106, 110);
        run("Measure");
        close();
        }
    }
    //saveAs("Results", pathcat+"well"+j+1+".csv");
    //run("Clear Results");
    run("Close All");
}
```

CODE C.2: measure.ijm

```
clear
filename = 'results.txt';
delimiterIn = '\t';
headerlinesIn = 1;
A = importdata(filename,delimiterIn,headerlinesIn);
intensities = A.data(:, 3);
M = size(intensities,1)/24;
wells = reshape(intensities,M,24);
%csvwrite('wells.csv',wells)
number_of_calibration_points = 5;
exposures_per_calibration = 5;
calibration_exposures = wells(1:[number_of_calibration_points*
    ↪ exposures_per_calibration],:);
calibration = zeros(number_of_calibration_points,24);
start = 1;
last = exposures_per_calibration;


for n = 1:number_of_calibration_points
   m = calibration_exposures(start:last,:);
   calibration(n,:) = mean(m);
   start = last+1;
   last = last+exposures_per_calibration;
end
```

```matlab
csvwrite('calibration-intensities.csv',calibration)
exp = wells(number_of_calibration_points*exposures_per_calibration+1:length(wells
    ↪ ),:);
csvwrite('characterization-intensities.csv',exp)
%%% Stern-Volmer
calibration_tanks = [0, 1, 7.5, 15, 21];
I1 = calibration(1,:);
I2 = calibration(number_of_calibration_points,:);
X1 = calibration_tanks(1);
X2 = calibration_tanks(number_of_calibration_points);
kt = (I2-I1)./((X1*I1)-(X2*I2)); % calculation for Ktau
Io = I1;
x1 = [0:1:25]'; % makes x values for plot of stern-volmer
%stern_volmer_plot = x1*kt+1; % plots I0/I Vs oxygen
%intensity_plot = I0./(1+kt*x1); % plots intensity(I) Vs oxygen


for i = 1:24
    oxygen_percent(:,i) = ((Io(i)./exp(:,i))-1)/kt(i);
end


%%% Two-Site Stern-Volmer fitting
Q = calibration_tanks';
for i = 1:24
    I = calibration(:,i);
    I0 = I1(i);
    % (f1/(1+ksv1*Q))+(1-f1/(1+ksv2*Q))== I/I0 ; f1+f2=1, f1=1-f2 f2=1-f1
    g = fittype('I0*((f1/(1+ksv1*Q))+((1-f1)/(1+ksv2*Q)))',...
            'independent',{'Q'},'dependent','I','problem','I0');
    myfit = fit(Q,I,g,'problem',I0,'lower',[0 0 0],'upper',[1 inf inf],'Start
    ↪ ',[0, 0, 0]);
    coeff_twosite(:,i) = coeffvalues(myfit)';
    %hold on
    %plot(myfit,Q,I)
end

for i = 1:24
    coeff=coeff_twosite(:,i);
    f1 = coeff(1);
    f2 = 1-f1;
    ksv1 = coeff(2);
    ksv2 = coeff(3);
    I0 = I1(i);
    I = exp(:,i);
    a =(I0^2*f1^2*ksv2^2 + 2*I0^2*f1*f2*ksv1*ksv2 + I0^2*f2^2*ksv1^2 + 2*I0*I*f1*
    ↪ ksv1*ksv2 - 2*I0*I*f1*ksv2^2 - 2*I0*I*f2*ksv1^2 + 2*I0*I*f2*ksv1*ksv2 + I
    ↪ .^2*ksv1^2 - 2*I.^2*ksv1*ksv2 + I.^2*ksv2^2);
    b = -I*ksv2 - I*ksv1 + I0*f1*ksv2 + I0*f2*ksv1;
    c = (2*I*ksv1*ksv2);
```

```
    oxygen_percent_twosite(:,i) = ((a.^(1/2))+b)./c;
end
%figure
plot(oxygen_percent_twosite,'b-')
%hold on
%plot(oxygen_percent,'r--')
csvwrite('analyzed-oxygen-values-150807.csv',oxygen_percent_twosite)
```

CODE C.3: sternvolmer.m

Appendix D

Re-Use Permissions

Chapter/section 1.1.1 to 1.1.5 of this thesis is adapted from my previous publication [10] with permission from The Royal Society of Chemistry.

Chapter/section 1.1.6, 2.1, 3.1 and 4.1 of this thesis is adapted from my previous publication [123]. PLOS applies the Creative Commons Attribution (CC BY) license to works published. Under this license, authors retain ownership of the copyright for their content, but they allow anyone to download, reuse, reprint, modify, distribute and/or copy the content as long as the original authors and source are cited.

Chapter/section 1.2, 2.2, 3.2 and 4.2 of this thesis is adapted from my previous publication [181]. This work, published in BioRxiv is licensed under a Creative Commons Attribution-NonCommercial 4.0 International License.

Bibliography

[1] Shawn C Oppegard, Alexander J Blake, Justin C Williams, and David T Eddington. Precise control over the oxygen conditions within the Boyden chamber using a microfabricated insert. *Lab on a chip*, 10(18):2366–2373, sep 2010. ISSN 1473-0197. doi: 10.1039/c004856a. URL http://www.ncbi.nlm.nih.gov/pubmed/20689862.

[2] Bethany C Gross, Jayda L Erkal, Sarah Y Lockwood, Chengpeng Chen, and Dana M Spence. Evaluation of 3D Printing and Its Potential Impact on Biotechnology and the Chemical Sciences. *Analytical Chemistry*, 86(7):3240–3253, apr 2014. ISSN 0003-2700. doi: 10.1021/ac403397r. URL http://pubs.acs.org/doi/abs/10.1021/ac403397r.

[3] Bas Wijnen, Emily J Hunt, Gerald C Anzalone, and Joshua M Pearce. Open-Source Syringe Pump Library. *PLoS ONE*, 9(9):e107216, 2014. ISSN 1932-6203. doi: 10.1371/journal.pone.0107216. URL http://dx.plos.org/10.1371/journal.pone.0107216.

[4] Tom Baden. Biropette: customisable, high precision pipette., 2014. URL http://www.thingiverse.com/thing:255519.

[5] S a Lacks. Cloning and Expression of Pneumococcal Genes in Streptococcus pneumoniae. *Microbial drug resistance*, 3(4):327–337, 1997. ISSN 1076-6294.

[6] Pingan Zhu and Liqiu Wang. Passive and active droplet generation with microfluidics: a review. *Lab on a Chip*, 17(online):34–75, 2017. ISSN 1473-0197. doi: 10.1039/C6LC01018K. URL http://pubs.rsc.org/en/Content/ArticleLanding/2016/LC/C6LC01018K{%}7B{%}25{%}7D5Cnhttp://dx.doi.org/10.1039/C6LC01018K.

[7] Wolfgang K R Barnikol and Harald Pötzschke. A novel, non-invasive diagnostic clinical procedure for the determination of an oxygenation status of chronic lower leg ulcers using peri-ulceral transcutaneous oxygen partial pressure measurements: results of its application in chronic venous insufficien. *German medical science : GMS e-journal*, 10:Doc11, jan 2012. ISSN 1612-3174. doi: 10.3205/000162. URL http://www.pubmedcentral.nih.gov/articlerender.fcgi?artid=3380238{%}7B{&}{%}7Dtool=pmcentrez{%}7B{&}{%}7Drendertype=abstract.

[8] Gianluca D'Ippolito, Sylma Diabira, Guy a Howard, Bernard a Roos, and Paul C Schiller. Low oxygen tension inhibits osteogenic differentiation and enhances stemness of human MIAMI cells. *Bone*, 39(3):513–522, sep 2006. ISSN 8756-3282. doi: 10.1016/j.bone.2006.02.061. URL http://www.ncbi.nlm.nih.gov/pubmed/16616713.

[9] Zoran Ivanovic. Hypoxia or in situ normoxia: The stem cell paradigm. *Journal of cellular physiology*, 219(2):271–5, may 2009. ISSN 1097-4652. doi: 10.1002/jcp.21690. URL http://www.ncbi.nlm.nih.gov/pubmed/19160417.

[10] Martin D Brennan, Megan L Rexius-Hall, Laura Jane Elgass, and David T Eddington. Oxygen control with microfluidics. *Lab Chip*, 14(22):4305–4318, 2014. ISSN 1473-0197. doi: 10.1039/C4LC00853G. URL http://xlink.rsc.org/?DOI=C4LC00853G.

[11] Vinit Kumar and Dmitry I Gabrilovich. Hypoxia-inducible factors in regulation of immune responses in tumour microenvironment. *Immunology*, 143(4):512–519, 2014. ISSN 00192805. doi: 10.1111/imm.12380. URL http://doi.wiley.com/10.1111/imm.12380.

[12] Peter Vaupel and Louis Harrison. Tumor hypoxia: causative factors, compensatory mechanisms, and cellular response. *The oncologist*, 9 Suppl 5 (Supplement 5):4–9, jan 2004. ISSN 1083-7159. doi: 10.1634/theoncologist.9-90005-4. URL http://theoncologist.alphamedpress.org/content/9/suppl{%}7B_}{%}7D5/4.full.

[13] Peter Vaupel and Arnulf Mayer. Hypoxia in cancer: significance and impact on clinical outcome. *Cancer metastasis reviews*, 26(2):225–39, jun 2007. ISSN 0167-7659. doi: 10.1007/s10555-007-9055-1. URL http://www.ncbi.nlm.nih.gov/pubmed/17440684.

[14] Daniele M Gilkes, Gregg L Semenza, and Denis Wirtz. Hypoxia and the extracellular matrix: drivers of tumour metastasis. *Nature reviews. Cancer*, 14 (6):430–9, jun 2014. ISSN 1474-1768. doi: 10.1038/nrc3726. URL http://dx.doi.org/10.1038/nrc3726.

[15] Qingdong Ke and Max Costa. Hypoxia-inducible factor-1 (HIF-1). *Molecular pharmacology*, 70(5):1469–80, nov 2006. ISSN 0026-895X. doi: 10.1124/mol.106.027029. URL http://molpharm.aspetjournals.org/content/70/5/1469.short.

[16] G L Semenza. Regulation of mammalian O2 homeostasis by hypoxia-inducible factor 1. *Annual review of cell and developmental biology*, 15:551–78, jan 1999. ISSN 1081-0706. doi: 10.1146/annurev.cellbio.15.1.551. URL http://www.annualreviews.org/doi/abs/10.1146/annurev.cellbio.15.1.551.

[17] Gregg Semenza. Signal transduction to hypoxia-inducible factor 1. *Biochemical pharmacology*, 64(5-6):993–8, sep 2002. ISSN 0006-2952. URL http://www.ncbi.nlm.nih.gov/pubmed/12213597.

[18] S. G. Charati and S. A. Stern. Diffusion of Gases in Silicone Polymers: Molecular Dynamics Simulations. *Macromolecules*, 31(16):5529–5535, aug 1998. ISSN 0024-9297. doi: 10.1021/ma980387e. URL http://dx.doi.org/10.1021/ma980387e.

[19] Min-Cheol Kim, Raymond H. W. Lam, Todd Thorsen, and H. Harry Asada. Mathematical analysis of oxygen transfer through polydimethylsiloxane membrane between double layers of cell culture channel and gas chamber in microfluidic oxygenator. *Microfluidics and Nanofluidics*, 15(3):285–296, feb 2013. ISSN 1613-4982. doi: 10.1007/s10404-013-1142-8. URL http://link.springer.com/10.1007/s10404-013-1142-8.

[20] Mark Polinkovsky, Edgar Gutierrez, Andre Levchenko, and Alex Groisman. Fine temporal control of the medium gas content and acidity and on-chip generation of series of oxygen concentrations for cell cultures. *Lab on a chip*, 9(8):1073–84, apr

2009. ISSN 1473-0197. doi: 10.1039/b816191g. URL http://pubs.rsc.org/en/Content/ArticleHTML/2009/LC/B816191G.

[21] Ludwig Wilhelm Winkler. Die Bestimmung des im Wasser gelösten Sauerstoffes. *Berichte der deutschen chemischen Gesellschaft*, 21(2):2843–2854, jul 1888. ISSN 03659496. doi: 10.1002/cber.188802102122. URL http://doi.wiley.com/10.1002/cber.188802102122.

[22] J R Clark Leland C., Richard Wolf, Donald Granger, and Zena Taylor. Continuous Recording of Blood Oxygen Tensions by Polarography. *J Appl Physiol*, 6(3):189–193, sep 1953. URL http://jap.physiology.org/content/6/3/189.

[23] Raymond H W Lam, Min-Cheol Kim, and Todd Thorsen. Culturing aerobic and anaerobic bacteria and mammalian cells with a microfluidic differential oxygenator. *Analytical chemistry*, 81(14):5918–5924, jul 2009. ISSN 1520-6882. doi: 10.1021/ac9006864. URL http://www.pubmedcentral.nih.gov/articlerender.fcgi?artid=2710860{%}7B{&}{%}7Dtool=pmcentrez{%}7B{&}{%}7Drendertype=abstract.

[24] Joseph R. Lakowicz. *Principles of Fluorescence Spectroscopy Principles of Fluorescence Spectroscopy*. 2006. ISBN 978-0-387-31278-1 (Print) 978-0-387-46312-4 (Online). doi: 10.1007/978-0-387-46312-4.

[25] Dhruv Sud, Geeta Mehta, Khamir Mehta, Jennifer Linderman, Shuichi Takayama, and Mary-Ann Mycek. Optical imaging in microfluidic bioreactors enables oxygen monitoring for continuous cell culture. *Journal of biomedical optics*, 11(5):50504, jan 2006. ISSN 1083-3668. doi: 10.1117/1.2355665. URL http://biomedicaloptics.spiedigitallibrary.org/article.aspx?articleid=1102282.

[26] Geeta Mehta, Khamir Mehta, Dhruv Sud, Jonathan W Song, Tommaso Bersano-Begey, Nobuyuki Futai, Yun Seok Heo, Mary-Ann Mycek, Jennifer J Linderman, and Shuichi Takayama. Quantitative measurement and control of oxygen levels in microfluidic poly(dimethylsiloxane) bioreactors during cell culture. *Biomedical microdevices*, 9(2):123–34, apr 2007. ISSN 1387-2176. doi: 10.1007/s10544-006-9005-7. URL http://www.ncbi.nlm.nih.gov/pubmed/17160707.

[27] Elly Sinkala and David T Eddington. Oxygen sensitive microwells. *Lab on a chip*, 10(23):3291–5, dec 2010. ISSN 1473-0197. doi: 10.1039/c0lc00244e. URL http://pubs.rsc.org/en/Content/ArticleHTML/2010/LC/C0LC00244E.

[28] Adam P Vollmer, Ronald F Probstein, Richard Gilbert, and Todd Thorsen. Development of an integrated microfluidic platform for dynamic oxygen sensing and delivery in a flowing medium. *Lab on a chip*, 5(10):1059–66, oct 2005. ISSN 1473-0197. doi: 10.1039/b508097e. URL http://pubs.rsc.org/en/Content/ArticleHTML/2005/LC/B508097E.

[29] Edwin J. Park, Kendra R. Reid, Wei Tang, Robert T. Kennedy, and Raoul Kopelman. Ratiometric fiber optic sensors for the detection of inter- and intra-cellular dissolved oxygen. *Journal of Materials Chemistry*, 15(27-28):2913, jul 2005. ISSN 0959-9428. doi: 10.1039/b502981c. URL http://pubs.rsc.org/en/Content/ArticleHTML/2005/JM/B502981C.

[30] Vasantha Kumar Bhaskara, Indra Mohanam, Jasti S Rao, and Sanjeeva Mohanam. Intermittent hypoxia regulates stem-like characteristics and differentiation of neuroblastoma cells. *PloS one*, 7(2):e30905, jan 2012. ISSN 1932-6203. doi: 10.1371/journal.pone.0030905. URL http://www.plosone.org/article/info:doi/10.1371/journal.pone.0030905{%}7B{#}{%}7Dpone-0030905-g006.

[31] Mingli Han, Yimeng Wang, Manran Liu, Xiaokai Bi, Junjie Bao, Ni Zeng, Zhikun Zhu, Zhiqiang Mo, Chengyi Wu, and Xin Chen. MiR-21 regulates epithelial-mesenchymal transition phenotype and hypoxia-inducible factor-1α expression in third-sphere forming breast cancer stem cell-like cells. *Cancer science*, 103(6): 1058–64, jun 2012. ISSN 1349-7006. doi: 10.1111/j.1349-7006.2012.02281.x. URL http://www.ncbi.nlm.nih.gov/pubmed/22435731.

[32] Lynn A Dudash, Faina Kligman, Samantha M Sarett, Kandice Kottke-Marchant, and Roger E Marchant. Endothelial cell attachment and shear response on biomimetic polymer-coated vascular grafts. *Journal of biomedical materials research. Part A*, 100(8):2204–2210, aug 2012. ISSN 1552-4965. doi: 10.1002/jbm.a.34119. URL http://www.pubmedcentral.nih.gov/articlerender.fcgi?artid=3381056{%}7B{&}{%}7Dtool=pmcentrez{%}7B{&}{%}7Drendertype=abstract.

[33] Chih-Wen Ni, Haiwei Qiu, and Hanjoong Jo. MicroRNA-663 upregulated by oscillatory shear stress plays a role in inflammatory response of endothelial cells. *American journal of physiology. Heart and circulatory physiology*, 300(5): H1762–9, may 2011. ISSN 1522-1539. doi: 10.1152/ajpheart.00829.2010. URL http://classic.ajpheart.physiology.org/content/300/5/H1762.full.

[34] Syotaro Obi, Kimiko Yamamoto, Joji Ando, Haruchika Masuda, and Takayuki Asahara. Differentiation of circulating endothelial progenitor cells induced by shear stress. In *2012 International Symposium on Micro-NanoMechatronics and Human Science (MHS)*, pages 54–58. IEEE, apr 2012. ISBN 978-1-4673-4813-3. doi: 10.1109/MHS.2012.6492452. URL http://ieeexplore.ieee.org/lpdocs/epic03/wrapper.htm?arnumber=6492452.

[35] C Holleyman, D Larson, and K Hunter. Simulation of ischemic reperfusion in endothelial cell culture increases apoptosis. *The Journal of extra-corporeal technology*, 33(3):175–80, sep 2001. ISSN 0022-1058. URL http://europepmc.org/abstract/MED/11680731.

[36] L Wyld, M W Reed, and N J Brown. The influence of hypoxia and pH on aminolaevulinic acid-induced photodynamic therapy in bladder cancer cells in vitro. *British journal of cancer*, 77(10):1621–1627, may 1998. ISSN 0007-0920. URL http://www.pubmedcentral.nih.gov/articlerender.fcgi?artid=2150064{%}7B{&}{%}7Dtool=pmcentrez{%}7B{&}{%}7Drendertype=abstract.

[37] Samantha Grist, Linfen Yu, Lukas Chrostowski, and Karen C. Cheung. Microfluidic cell culture systems with integrated sensors for drug screening. In Holger Becker and Bonnie L. Gray, editors, *SPIE MOEMS-MEMS*, page 825103. International Society for Optics and Photonics, feb 2012. doi: 10.1117/12.911427. URL http://proceedings.spiedigitallibrary.org/proceeding.aspx?articleid=1278967.

[38] Eric Leclerc, Yasuyuki Sakai, and Teruo Fujii. Microfluidic PDMS (polydimethylsiloxane) bioreactor for large-scale culture of hepatocytes. *Biotechnology progress*, 20(3):750–5. ISSN 8756-7938. doi: 10.1021/bp0300568. URL http://www.ncbi.nlm.nih.gov/pubmed/15176878.

[39] Micha Adler, Mark Polinkovsky, Edgar Gutierrez, and Alex Groisman. Generation of oxygen gradients with arbitrary shapes in a microfluidic device. *Lab on a chip*, 10(3):388–391, feb 2010. ISSN 1473-0197. doi: 10.1039/b920401f. URL http://www.pubmedcentral.nih.gov/articlerender.fcgi?artid=2887752{%}7B{&}{%}7Dtool=pmcentrez{%}7B{&}{%}7Drendertype=abstract.

[40] Shawn C Oppegard, Ki Hwan Nam, Janai R Carr, Stacey C Skaalure, and David T Eddington. Modulating temporal and spatial oxygenation over adherent cellular cultures. *PLoS ONE*, 4(9), 2009. ISSN 19326203. doi: 10.1371/journal.pone.0006891.

[41] Hasan E Abaci, Raghavendra Devendra, Rohan Soman, German Drazer, and Sharon Gerecht. Microbioreactors to manipulate oxygen tension and shear stress in the microenvironment of vascular stem and progenitor cells. *Biotechnology and applied biochemistry*, 59(2):97–105, 2012. ISSN 1470-8744. doi: 10.1002/bab.1010. URL http://www.ncbi.nlm.nih.gov/pubmed/23586790.

[42] Kenichi Funamoto, Ioannis K Zervantonakis, Yuchun Liu, Christopher J Ochs, Choong Kim, and Roger D Kamm. A novel microfluidic platform for high-resolution imaging of a three-dimensional cell culture under a controlled hypoxic environment. *Lab on a chip*, 12(22):4855–4863, nov 2012. ISSN 1473-0189. doi: 10.1039/c2lc40306d. URL http://www.ncbi.nlm.nih.gov/pubmed/23023115.

[43] J M Higgins, D T Eddington, S N Bhatia, and L Mahadevan. Sickle cell vasoocclusion and rescue in a microfluidic device. *Proceedings of the National Academy of Sciences of the United States of America*, 104(51):20496–20500, dec 2007. ISSN 1091-6490. doi: 10.1073/pnas.0707122105. URL http://www.pubmedcentral.nih.gov/articlerender.fcgi?artid=2154459{%}7B{&}{%}7Dtool=pmcentrez{%}7B{&}{%}7Drendertype=abstract.

[44] Joe F Lo, Martin Brennan, Zameer Merchant, Lin Chen, Shujuan Guo, David T Eddington, and Luisa a DiPietro. Microfluidic wound bandage: localized oxygen modulation of collagen maturation. *Wound repair and regeneration : official publication of the Wound Healing Society [and] the European Tissue Repair Society*, 21(2):226–234, 2013. ISSN 1524-475X. doi: 10.1111/wrr.12021. URL http://www.ncbi.nlm.nih.gov/pubmed/23438079.

[45] Gerardo Mauleon, Christopher P Fall, and David T Eddington. Precise spatial and temporal control of oxygen within in vitro brain slices via microfluidic gas channels. *PloS one*, 7(8):e43309, jan 2012. ISSN 1932-6203. doi: 10.1371/journal.pone.0043309. URL http://www.pubmedcentral.nih.gov/articlerender.fcgi?artid=3419219{%}7B{&}{%}7Dtool=pmcentrez{%}7B{&}{%}7Drendertype=abstract.

[46] Gerardo Mauleon, Joe F Lo, Bethany L Peterson, Christopher P Fall, and David T Eddington. Enhanced loading of Fura-2/AM calcium indicator dye in adult rodent brain slices via a microfluidic oxygenator. *Journal of neuroscience methods*, 216 (2):110–117, jun 2013. ISSN 1872-678X. doi: 10.1016/j.jneumeth.2013.04.007. URL http://www.ncbi.nlm.nih.gov/pubmed/23608309.

[47] Micha Adler, Michael Erickstad, Edgar Gutierrez, and Alex Groisman. Studies of bacterial aerotaxis in a microfluidic device. *Lab on a chip*, 12(22):4835–4847, nov 2012. ISSN 1473-0189. doi: 10.1039/c2lc21006a. URL http://www.pubmedcentral.nih.gov/articlerender.fcgi?artid=3520485{%}7B{&}{%}7Dtool=pmcentrez{%}7B{&}{%}7Drendertype=abstract.

[48] Joe F Lo, Elly Sinkala, and David T Eddington. Oxygen gradients for open well cellular cultures via microfluidic substrates. *Lab on a chip*, 10(18):2394–2401, sep 2010. ISSN 1473-0197. doi: 10.1039/c004660d. URL http://pubs.rsc.org/en/content/articlehtml/2010/lc/c004660d.

[49] David K Wood, Alicia Soriano, L Mahadevan, John M Higgins, and Sangeeta N Bhatia. A biophysical indicator of vaso-occlusive risk in sickle cell disease. *Science translational medicine*, 4(123):123ra26, feb 2012. ISSN 1946-6242. doi: 10.1126/scitranslmed.3002738. URL /pmc/articles/PMC3633235/?report=abstract.

[50] Xin Cui, Hon Ming Yip, Qian Zhu, Chengpeng Yang, and Raymond H. W. Lam. Microfluidic long-term differential oxygenation for bacterial growth characteristics analyses. *RSC Advances*, 4(32):16662, apr 2014. ISSN 2046-2069. doi: 10.1039/c4ra01577k. URL http://pubs.rsc.org/en/content/articlehtml/2014/ra/c4ra01577k.

[51] Jared W Allen and Sangeeta N Bhatia. Formation of steady-state oxygen gradients in vitro: application to liver zonation. *Biotechnology and bioengineering*, 82(3):

253–62, may 2003. ISSN 0006-3592. doi: 10.1002/bit.10569. URL http://www.ncbi.nlm.nih.gov/pubmed/12599251.

[52] Jared W Allen, Salman R Khetani, and Sangeeta N Bhatia. In vitro zonation and toxicity in a hepatocyte bioreactor. *Toxicological sciences : an official journal of the Society of Toxicology*, 84(1):110–9, mar 2005. ISSN 1096-6080. doi: 10.1093/toxsci/kfi052. URL http://toxsci.oxfordjournals.org/content/84/1/110.short.

[53] Maciej Skolimowski, Martin Weiss Nielsen, Jenny Emnéus, Søren Molin, Rafael Taboryski, Claus Sternberg, Martin Dufva, and Oliver Geschke. Microfluidic dissolved oxygen gradient generator biochip as a useful tool in bacterial biofilm studies. *Lab on a chip*, 10(16):2162–9, aug 2010. ISSN 1473-0197. doi: 10.1039/c003558k. URL http://pubs.rsc.org/en/Content/ArticleHTML/2010/LC/C003558K.

[54] Yung-Ann Chen, Andrew D King, Hsiu-Chen Shih, Chien-Chung Peng, Chueh-Yu Wu, Wei-Hao Liao, and Yi-Chung Tung. Generation of oxygen gradients in microfluidic devices for cell culture using spatially confined chemical reactions. *Lab on a chip*, 11(21):3626–33, nov 2011. ISSN 1473-0189. doi: 10.1039/c1lc20325h. URL http://www.ncbi.nlm.nih.gov/pubmed/21915399.

[55] Lei Wang, Wenming Liu, Yaolei Wang, Jian-chun Wang, Qin Tu, Rui Liu, and Jinyi Wang. Construction of oxygen and chemical concentration gradients in a single microfluidic device for studying tumor cell-drug interactions in a dynamic hypoxia microenvironment. *Lab on a chip*, 13(4):695–705, feb 2013. ISSN 1473-0189. doi: 10.1039/c2lc40661f. URL http://www.ncbi.nlm.nih.gov/pubmed/23254684.

[56] Marco Rasponi, Tania Ullah, Richard J Gilbert, Gianfranco B Fiore, and Todd A Thorsen. Realization and efficiency evaluation of a micro-photocatalytic cell prototype for real-time blood oxygenation. *Medical engineering {&} physics*, 33(7):887–892, sep 2011. ISSN 1873-4030. doi: 10.1016/j.medengphy.2010.10.008. URL http://www.sciencedirect.com/science/article/pii/S1350453310002390.

[57] Pieter Edmond Oomen, Maciej Skolimowski, and Sabeth Verpoorte. Implementing Oxygen Control in Chip-Based Cell and Tissue Culture Systems. *Lab on a Chip*,

16:3394–3414, 2016. ISSN 1473-0197. doi: 10.1039/C6LC00772D. URL http://pubs.rsc.org/en/Content/ArticleLanding/2016/LC/C6LC00772D.

[58] Ansgar Waldbaur, Holger Rapp, Kerstin Länge, and Bastian E Rapp. Let there be chip—towards rapid prototyping of microfluidic devices: one-step manufacturing processes. *Analytical Methods*, 3(12):2681, 2011. ISSN 1759-9660. doi: 10.1039/c1ay05253e. URL http://xlink.rsc.org/?DOI=c1ay05253e.

[59] Anthony K Au, Wonjae Lee, and Albert Folch. Mail-order microfluidics: evaluation of stereolithography for the production of microfluidic devices. *Lab on a chip*, 14 (7):1294–301, mar 2014. ISSN 1473-0189. doi: 10.1039/c3lc51360b. URL http://www.ncbi.nlm.nih.gov/pubmed/24510161.

[60] Germán Comina, Anke Suska, and Daniel Filippini. Low cost lab-on-a-chip prototyping with a consumer grade 3D printer. *Lab on a chip*, 14:2978–2982, 2014. ISSN 1473-0189. doi: 10.1039/c4lc00394b. URL http://www.ncbi.nlm.nih.gov/pubmed/24931176.

[61] Chengpeng Chen, Yimeng Wang, Sarah Y Lockwood, and Dana M Spence. 3D-printed fluidic devices enable quantitative evaluation of blood components in modified storage solutions for use in transfusion medicine. *The Analyst*, 139 (13):3219–26, jun 2014. ISSN 1364-5528. doi: 10.1039/c3an02357e. URL http://pubs.rsc.org/en/content/articlehtml/2014/an/c3an02357e.

[62] Aliaa I Shallan, Petr Smejkal, Monika Corban, Rosanne M Guijt, and Michael C Breadmore. Cost-effective three-dimensional printing of visibly transparent microchips within minutes. *Analytical Chemistry*, 86:3124–3130, 2014. ISSN 15206882. doi: 10.1021/ac4041857.

[63] Krisna C Bhargava, Bryant Thompson, and Noah Malmstadt. Discrete elements for 3D microfluidics. *Proceedings of the National Academy of Sciences*, 111(42): 15013–15018, 2014. ISSN 0027-8424. doi: 10.1073/pnas.1414764111. URL http://www.pnas.org/lookup/doi/10.1073/pnas.1414764111.

[64] Po Ki Yuen. SmartBuild-a truly plug-n-play modular microfluidic system. *Lab on a chip*, 8(8):1374–1378, 2008. ISSN 1473-0197. doi: 10.1039/b805086d.

[65] Kyoung G Lee, Kyun Joo Park, Seunghwan Seok, Sujeong Shin, Do Hyun Kim, Jung Youn Park, Yun Seok Heo, Seok-Jae Lee, and Tae Jae Lee. 3D printed

modules for integrated microfluidic devices. *RSC Advances*, pages 32876–32880, 2014. ISSN 2046-2069. doi: 10.1039/C4RA05072J. URL http://pubs.rsc.org/en/content/articlehtml/2014/ra/c4ra05072j.

[66] Peter Tek, Terry C Chiganos, Javeed Shaikh Mohammed, David T Eddington, Christopher P Fall, Peter Ifft, and Patrick J Rousche. Rapid prototyping for neuroscience and neural engineering. *Journal of Neuroscience Methods*, 172:263–269, 2008. ISSN 01650270. doi: 10.1016/j.jneumeth.2008.03.011.

[67] Philip J Kitson, Mali H Rosnes, Victor Sans, Vincenza Dragone, and Leroy Cronin. Configurable 3D-Printed millifluidic and microfluidic 'lab on a chip' reactionware devices. *Lab on a Chip*, 12(18):3267, 2012. ISSN 1473-0197. doi: 10.1039/c2lc40761b.

[68] M D Symes, P J Kitson, J Yan, C Richmond, G J T Cooper, R W Bowman, T Vilbrandt, and L Cronin. Integrated 3D-printed reactionware for chemical synthesis and analysis. *Nature Chemistry*, 4(5):349–354, 2012. ISSN 1755-4330. doi: 10.1038/nchem.1313. URL http://eprints.gla.ac.uk/68744/.

[69] Philip J Kitson, Mark D Symes, Vincenza Dragone, and Leroy Cronin. Combining 3D printing and liquid handling to produce user-friendly reactionware for chemical synthesis and purification. *Chemical Science*, 4:3099–3103, 2013. ISSN 20416520. doi: 10.1039/c3sc51253c. URL http://dx.doi.org/10.1039/c3sc51253c.

[70] Philip J Kitson, Ross J Marshall, Deliang Long, Ross S Forgan, and Leroy Cronin. 3D Printed high-throughput hydrothermal reactionware for discovery, optimization, and scale-up. *Angewandte Chemie - International Edition*, pages 1–7, 2014. ISSN 14337851. doi: 10.1002/anie.201402654.

[71] Wolfgang Busch, Brad T Moore, Bradley Martsberger, Daniel L Mace, Richard W Twigg, Jee Jung, Iulian Pruteanu-Malinici, Scott J Kennedy, Gregory K Fricke, Robert L Clark, Uwe Ohler, and Philip N Benfey. A microfluidic device and computational platform for high-throughput live imaging of gene expression. *Nature Methods*, 9(11), 2012. ISSN 1548-7091. doi: 10.1038/nmeth.2185.

[72] Jayda L Erkal, Asmira Selimovic, Bethany C Gross, Sarah Y Lockwood, Eric L Walton, Stephen McNamara, R Scott Martin, and Dana M Spence. 3D printed microfluidic devices with integrated versatile and reusable electrodes. *Lab on a*

chip, 14:2023–2032, 2014. ISSN 1473-0189. doi: 10.1039/c4lc00171k. URL http://www.ncbi.nlm.nih.gov/pubmed/24763966.

[73] Wonjae Lee, Donghoon Kwon, Boram Chung, Gyoo Yeol Jung, Anthony Au, Albert Folch, and Sangmin Jeon. Ultrarapid detection of pathogenic bacteria using a 3D immunomagnetic flow assay. *Analytical Chemistry*, 86(13):6683–6688, 2014. ISSN 15206882. doi: 10.1021/ac501436d.

[74] Wonjae Lee, Donghoon Kwon, Woong Choi, Gyoo Yeol Jung, and Sangmin Jeon. 3D-Printed Microfluidic Device for the Detection of Pathogenic Bacteria Using Size-based Separation in Helical Channel with Trapezoid Cross-Section. *Scientific Reports*, 5:7717, 2015. ISSN 2045-2322. doi: 10.1038/srep07717. URL http://www.nature.com/doifinder/10.1038/srep07717.

[75] Anthony K Au, Nirveek Bhattacharjee, Lisa F Horowitz, Tim C Chang, and Albert Folch. 3D-Printed Microfluidic Automation. *Lab Chip*, pages 1–8, 2015. ISSN 1473-0197. doi: 10.1039/C5LC00126A. URL http://pubs.rsc.org/en/Content/ArticleLanding/2015/LC/C5LC00126A.

[76] Alexandre Causier, Guillaume Carret, Céline Boutin, Thomas Berthelot, and Patrick Berthault. 3D-printed system optimizing dissolution of hyperpolarized gaseous species for micro-sized NMR. *Lab Chip*, 2015. ISSN 1473-0197. doi: 10.1039/C5LC00193E. URL http://pubs.rsc.org/en/Content/ArticleLanding/2015/LC/C5LC00193E.

[77] Albert Chi, Sebastian Curi, Kevin Clayton, David Luciano, Kameron Klauber, Alfredo Alexander-Katz, Sebastian D'hers, and Noel M Elman. Rapid Reconstitution Packages (RRPs) implemented by integration of computational fluid dynamics (CFD) and 3D printed microfluidics. *Drug Delivery and Translational Research*, 4(4):320–333, 2014. ISSN 2190-393X. doi: 10.1007/s13346-014-0198-7. URL http://link.springer.com/10.1007/s13346-014-0198-7.

[78] Greig Chisholm, Philip J Kitson, Niall D Kirkaldy, Leanne G Bloor, and Leroy Cronin. 3D printed flow plates for the electrolysis of water. *Energy {&} Environmental Science*, 7(iii):3026–3032, 2014. ISSN 1754-5692. doi: 10.1039/c4ee01426j. URL http://dx.doi.org/10.1039/C4EE01426J.

[79] J Cooper Mcdonald, Michael L Chabinyc, Steven J Metallo, Janelle R Anderson, Abraham D Stroock, and George M Whitesides. Prototyping of Microfluidic Devices in Poly (dimethylsiloxane) Using Solid-Object Printing the fabrication of microfluidic devices in poly (dimethyl-. *Analytical chemistry*, 74(7):1537–1545, 2002. ISSN 0003-2700. doi: 10.1021/ac010938q.

[80] Clint Gregory and Michael Veeman. 3D-printed microwell arrays for Ciona microinjection and timelapse imaging. *PLoS ONE*, 8(12):8–13, 2013. ISSN 19326203. doi: 10.1371/journal.pone.0082307.

[81] Philip H King, Gareth Jones, Hywel Morgan, Maurits R R de Planque, and Klaus-Peter Zauner. Interdroplet bilayer arrays in millifluidic droplet traps from 3D-printed moulds. *Lab on a chip*, 14(4):722–729, 2014. ISSN 1473-0189. doi: 10. 1039/c3lc51072g. URL http://www.ncbi.nlm.nih.gov/pubmed/24336841.

[82] Germán Comina, Anke Suska, and Daniel Filippini. PDMS lab-on-a-chip fabrication using 3D printed templates. *Lab on a chip*, 14:424–430, 2014. ISSN 1473-0189. doi: 10.1039/c3lc50956g. URL http://www.ncbi.nlm.nih.gov/pubmed/24281262.

[83] Ken-ichiro Kamei, Yasumasa Mashimo, Yoshie Koyama, Christopher Fockenberg, Miyuki Nakashima, Minako Nakajima, Junjun Li, and Yong Chen. 3D printing of soft lithography mold for rapid production of polydimethylsiloxane-based microfluidic devices for cell stimulation with concentration gradients. *Biomedical Microdevices*, 17(2), 2015. ISSN 1387-2176. doi: 10.1007/s10544-015-9928-y. URL http://link.springer.com/10.1007/s10544-015-9928-y.

[84] Daniel Therriault, Scott R White, and Jennifer A Lewis. Chaotic mixing in three-dimensional microvascular networks fabricated by direct-write assembly. *Nature materials*, 2(4):265–71, apr 2003. ISSN 1476-1122. doi: 10.1038/nmat863. URL http://dx.doi.org/10.1038/nmat863.

[85] Jordan S Miller, Kelly R Stevens, Michael T Yang, Brendon M Baker, Duc-Huy T Nguyen, Daniel M Cohen, Esteban Toro, Alice a Chen, Peter a Galie, Xiang Yu, Ritika Chaturvedi, Sangeeta N Bhatia, and Christopher S Chen. Rapid casting of patterned vascular networks for perfusable engineered three-dimensional tissues. *Nature materials*,

11(9):768–774, sep 2012. ISSN 1476-1122. doi: 10.1038/nmat3357. URL http://www.pubmedcentral.nih.gov/articlerender.fcgi?artid= 3586565{%}7B{&}{%}7Dtool=pmcentrez{%}7B{&}{%}7Drendertype=abstract.

[86] Rohit Bhargava and Matthew K Gelber. Monolithic Multilayer Microfluidics via Sacrificial Molding of 3D-Printed Isomalt. *Lab Chip*, 15:1736–1741, 2015. ISSN 1473-0197. doi: 10.1039/C4LC01392A. URL http://pubs.rsc.org/en/ Content/ArticleLanding/2015/LC/C4LC01392A.

[87] T Femmer, a Kuehne, and M Wessling. Print your own membrane: Direct rapid prototyping of polydimethylsiloxane. *Lab on a Chip*, 14:2610–2613, 2014. ISSN 1473-0197. doi: 10.1039/c4lc00320a. URL http://pubs.rsc.org/en/content/ articlehtml/2014/lc/c4lc00320a.

[88] Samuel K Sia and George M Whitesides. Microfluidic devices fabricated in poly(dimethylsiloxane) for biological studies. *Electrophoresis*, 24(21):3563–3576, 2003. ISSN 01730835. doi: 10.1002/elps.200305584.

[89] T Baden, Andre Maia Chagas, Greg Gage, Timothy Marzullo, Lucia L. Prieto-Godino, and Thomas Euler. Open Labware: 3-D Printing Your Own Lab Equipment. *PLOS Biology*, 13(3):e1002086, 2015. ISSN 1545-7885. doi: 10.1371/journal. pbio.1002086. URL http://dx.plos.org/10.1371/journal.pbio.1002086.

[90] Joshua M. Pearce. *Open-source Lab*. 2013. ISBN 9780124104624.

[91] Makerbot Industries. Makerbot, 2017. URL https://www.makerbot.com/.

[92] RepRap Project. RepRap, 2017. URL reprap.org.

[93] James N Fullerton, George C M Frodsham, and Richard M Day. 3D printing for the many, not the few. *Nature Biotechnology*, 32(11):1086–1087, 2014. ISSN 1087-0156. doi: 10.1038/nbt.3056. URL http://www.nature.com/doifinder/ 10.1038/nbt.3056.

[94] B T Wittbrodt, A G Glover, J Laureto, G C Anzalone, D Oppliger, J L Irwin, and J M Pearce. Life-cycle economic analysis of distributed manufacturing with open-source 3-D printers. *Mechatronics*, 23(6):713–726, 2013. ISSN 09574158. doi: 10.1016/j.mechatronics.2013.06.002. URL http://linkinghub.elsevier. com/retrieve/pii/S0957415813001153.

[95] Marius Kintel. OpenSCAD, 2017. URL http://www.openscad.org/.

[96] Blender Foudation. Blender. 2017. URL www.blender.org.

[97] Trimble Inc. SketchUp, 2016. URL www.sketchup.com.

[98] Autodesk Inc. Autodesk 123D, 2017. URL www.123dapp.com.

[99] Makerbot Industries. Thingiverse, 2017. URL https://www.thingiverse.com/.

[100] National Institutes of Health. NIH 3D Print Exchange. 2017. URL http://3dprint.nih.gov/.

[101] Stratasys. GrabCAD. URL https://grabcad.com/.

[102] GitHub Inc. GitHub. 2017. URL https://github.com/.

[103] Timothy C Marzullo and Gregory J Gage. The SpikerBox: A Low Cost, Open-Source BioAmplifier for Increasing Public Participation in Neuroscience Inquiry. *PLoS ONE*, 7(3):e30837, 2012. ISSN 1932-6203. doi: 10.1371/journal.pone.0030837. URL http://dx.plos.org/10.1371/journal.pone.0030837.

[104] Trudie Lang. Advancing global health research through digital technology and sharing data. *Science (New York, N.Y.)*, 331(6018):714–717, 2011. ISSN 1095-9203. doi: 10.1126/science.1199349.

[105] Ryan Fobel, Christian Fobel, and Aaron R. Wheeler. DropBot: An open-source digital microfluidic control system with precise control of electrostatic driving force and instantaneous drop velocity measurement. *Applied Physics Letters*, 102(19):1–5, 2013. ISSN 00036951. doi: 10.1063/1.4807118.

[106] Ed Baker. Open source data logger for low-cost environmental monitoring. *Biodiversity Data Journal*, page e1059, 2014. ISSN 1314-2828. doi: 10.3897/BDJ.2.e1059. URL http://www.pubmedcentral.nih.gov/articlerender.fcgi?artid=4030251{&}tool=pmcentrez{&}rendertype=abstract.

[107] James S Cybulski, James Clements, and Manu Prakash. Foldscope: origami-based paper microscope. *PloS one*, 9(6):e98781, 2014. ISSN 1932-6203. doi: 10.1371/journal.pone.0098781. URL http://journals.plos.org/plosone/article?id=10.1371/journal.pone.0098781.

[108] M Saad Bhamla, Brandon Benson, Chew Chai, Georgios Katsikis, Aanchal Johri, and Manu Prakash. Hand-powered Ultralow-cost Paper Centrifuge. *Nature Biomedical Engineering*, 1(1):9, 2017. ISSN 2157-846X. doi: 10.1038/ s41551-016-0009. URL http://www.nature.com/articles/s41551-016-0009.

[109] J M Pearce. Building Research Equipment with Free, Open-Source Hardware. *Science*, 337(6100):1303–1304, sep 2012. ISSN 0036-8075. doi: 10.1126/science.1228183. URL citeulike-article-id: 11241059{%}7B{%}25{%}7D5Cnhttp://dx.doi.org/10.1126/science. 1226328http://www.ncbi.nlm.nih.gov/pubmed/22984060http://www. sciencemag.org/cgi/doi/10.1126/science.1228183.

[110] Timothy M Rankin, Nicholas A Giovinco, Daniel J Cucher, George Watts, Bonnie Hurwitz, and David G Armstrong. Three-dimensional printing surgical instruments: are we there yet? *Journal of Surgical Research*, 189(2):193–197, 2014. ISSN 00224804. doi: 10.1016/j.jss.2014.02.020. URL http://linkinghub.elsevier. com/retrieve/pii/S0022480414001644.

[111] M S Sulkin, E Widder, C Shao, K M Holzem, C Gloschat, S R Gutbrod, and I R Efimov. Three-dimensional printing physiology laboratory technology. *AJP: Heart and Circulatory Physiology*, 305(11):H1569—-H1573, 2013. ISSN 0363-6135. doi: 10.1152/ajpheart.00599.2013. URL http://ajpheart.physiology. org/cgi/doi/10.1152/ajpheart.00599.2013.

[112] Michael D M Dryden and Aaron R. Wheeler. DStat: A versatile, open-source potentiostat for electroanalysis and integration. *PLoS ONE*, 10(10):1–17, 2015. ISSN 19326203. doi: 10.1371/journal.pone.0140349. URL http://dx.doi.org/ 10.1371/journal.pone.0140349.

[113] Eric Tavares da Costa, Maria F Mora, Peter a. Willis, Claudimir L do Lago, Hong Jiao, and Carlos D Garcia. Getting started with open-hardware: Development and control of microfluidic devices. *Electrophoresis*, 35(16):2370–2377, 2014. ISSN 15222683. doi: 10.1002/elps.201400128.

[114] Chai Biotechnologies Inc. Open PCR, 2017. URL http://openpcr.org/.

[115] Jordan E Trachtenberg, Paschalia M Mountziaris, Jordan S Miller, Matthew Wettergreen, Fred K Kasper, and Antonios G Mikos. Open-source three-dimensional

printing of biodegradable polymer scaffolds for tissue engineering. *Journal of Biomedical Materials Research - Part A*, 102(12):4326–4335, 2014. ISSN 15524965. doi: 10.1002/jbm.a.35108.

[116] David G Rosenegger, Cam Ha T Tran, Jeffery LeDue, Ning Zhou, and Grant R Gordon. A High Performance, Cost-Effective, Open-Source Microscope for Scanning Two-Photon Microscopy that Is Modular and Readily Adaptable. *PLoS ONE*, 9(10):e110475, 2014. ISSN 1932-6203. doi: 10.1371/journal.pone.0110475. URL http://dx.plos.org/10.1371/journal.pone.0110475.

[117] Cathal Garvey. DremelFuge, 2009. URL https://www.thingiverse.com/thing:1483.

[118] Chenlong Zhang, Nicholas C Anzalone, Rodrigo P Faria, and Joshua M Pearce. Open-Source 3D-Printable Optics Equipment. *PLoS ONE*, 8(3), 2013. ISSN 19326203. doi: 10.1371/journal.pone.0059840.

[119] Tom Baden. Raspberry Pi Scope. 2014. URL http://3dprint.nih.gov/discover/3dpx-000609.

[120] Konrad Walus. A Fully Printable Microscope, 2014. URL http://3dprint.nih.gov/discover/3dpx-000304.

[121] William G. Patrick, Alec A K Nielsen, Steven J. Keating, Taylor J. Levy, Che Wei Wang, Jaime J. Rivera, Octavio Mondragón-Palomino, Peter A. Carr, Christopher A. Voigt, Neri Oxman, and David S. Kong. DNA assembly in 3D printed fluidics. *PLoS ONE*, 10(12):1–18, 2015. ISSN 19326203. doi: 10.1371/journal.pone.0143636.

[122] Jennifer S. Mathieson, Mali H. Rosnes, Victor Sans, Philip J. Kitson, and Leroy Cronin. Continuous parallel ESI-MS analysis of reactions carried out in a bespoke 3D printed device. *Beilstein Journal of Nanotechnology*, 4(1):285–291, 2013. ISSN 21904286. doi: 10.3762/bjnano.4.31.

[123] Martin D Brennan, Megan L Rexius-Hall, and David T Eddington. A 3D-Printed Oxygen Control Insert for a 24-Well Plate. *Plos One*, 10(9):e0137631, 2015. ISSN 1932-6203. doi: 10.1371/journal.pone.0137631. URL http://dx.plos.org/10.1371/journal.pone.0137631.

[124] Vincenza Dragone, Victor Sans, Mali H. Rosnes, Philip J. Kitson, and Leroy Cronin. 3D-printed devices for continuous-flow organic chemistry. *Beilstein Journal of Organic Chemistry*, 9:951–959, 2013. ISSN 18605397. doi: 10.3762/bjoc.9. 109.

[125] Plos Collections. Open Source Toolkit Hardware, 2017. URL http://collections.plos.org/open-source-toolkit-hardware.

[126] International Organization for Standardization. *ISO 8655-1:2002(en)*. 2002.

[127] Kensuke Takagishi and Shinjiro Umezu. Development of the Improving Process for the 3D Printed Structure. *Nature Publishing Group*, (November 2016):1–10, 2017. doi: 10.1038/srep39852. URL http://dx.doi.org/10.1038/srep39852.

[128] Fred Griffith. The Significance of Pneumococcal Types. *The Journal of hygiene*, 27(2):113–159, jan 1928. ISSN 0022-1724. doi: 10.1093/clinids/ 3.2.372. URL http://www.ncbi.nlm.nih.gov/pubmed/20474956http://www.pubmedcentral.nih.gov/articlerender.fcgi?artid=PMC2167760.

[129] O T Avery, C M Macleod, and M McCarty. STUDIES ON THE CHEMICAL NATURE OF THE SUBSTANCE INDUCING TRANSFORMATION OF PNEU- MOCOCCAL TYPES : INDUCTION OF TRANSFORMATION BY A DES- OXYRIBONUCLEIC ACID FRACTION ISOLATED FROM PNEUMOCOC- CUS TYPE III. *The Journal of experimental medicine*, 79(2):137–158, feb 1944. ISSN 0022-1007. URL http://www.ncbi.nlm.nih.gov/pubmed/19871359http://www.pubmedcentral.nih.gov/articlerender.fcgi?artid=PMC2135445.

[130] V J FREEMAN. Studies on the virulence of bacteriophage-infected strains of Corynebacterium diphtheriae. *Journal of bacteriology*, 61(6):675–688, 1951. ISSN 00219193.

[131] A D HERSHEY and M CHASE. Independent functions of viral pro- tein and nucleic acid in growth of bacteriophage. *The Journal of gen- eral physiology*, 36(1):39–56, may 1952. ISSN 0022-1295. URL http://www.ncbi.nlm.nih.gov/pubmed/12981234http://www.pubmedcentral.nih.gov/articlerender.fcgi?artid=PMC2147348.

[132] J D WATSON and F H C CRICK. Molecular Structure of Nucleic Acids: A Structure for Deoxyribose Nucleic Acid. *Nature*, 171(4356):

737–738, apr 1953. ISSN 0028-0836. doi: 10.1038/171737a0. URL http://www.nature.com/physics/looking-back/crick/{%}7B{%}25{%}7D5Cnhttp://www.ncbi.nlm.nih.gov/pubmed/13054692http://www.ncbi.nlm.nih.gov/pubmed/1943http://www.nature.com/doifinder/10.1038/171737a0.

[133] Eugene V Koonin. Horizontal gene transfer: essentiality and evolvability in prokaryotes, and roles in evolutionary transitions. *F1000Research*, 5(0):1805, 2016. ISSN 2046-1402. doi: 10.12688/f1000research.8737.1. URL http://f1000research.com/articles/5-1805/v1.

[134] J Peter Gogarten and Jeffrey P Townsend. Horizontal gene transfer, genome innovation and evolution. *Nat Rev Micro*, 3(9):679–687, sep 2005. ISSN 1740-1526. URL http://dx.doi.org/10.1038/nrmicro1204.

[135] Nicholas J Croucher, Simon R Harris, Christophe Fraser, Michael A Quail, J Burton, M van der Linden, L McGee, A von Gottberg, Jae Hoon Song, Kwan Soo Ko, Bruno Pichon, Stephen Baker, Christopher M Parry, L M Lambertsen, Dea Shahinas, Dylan R Pillai, Timothy J Mitchell, Gordon Dougan, Alexander Tomasz, Keith P Klugman, Julian Parkhill, William P Hanage, and Stephen D Bentley. Rapid Pneumococcal Evolution in Response to Clinical Interventions. *Science*, 331 (6016):430–434, jan 2011. ISSN 0036-8075. doi: 10.1126/science.1198545. URL http://www.sciencemag.org/cgi/doi/10.1126/science.1198545.

[136] Chrispin Chaguza, Jennifer E Cornick, and Dean B Everett. Mechanisms and impact of genetic recombination in the evolution of Streptococcus pneumoniae. *Computational and Structural Biotechnology Journal*, 13:241–247, 2015. ISSN 2001-0370. doi: 10.1016/j.csbj.2015.03.007. URL http://www.sciencedirect.com/science/article/pii/S2001037015000161.

[137] Calum Johnston, Nathalie Campo, Matthieu J Bergé, Patrice Polard, and Jean Pierre Claverys. Streptococcus pneumoniae, le transformiste. *Trends in Microbiology*, 22(3):113–119, 2014. ISSN 0966842X. doi: 10.1016/j.tim.2014.01.002.

[138] Inês Chen and David Dubnau. DNA Uptake during Bacterial Transformation. *Nature reviews. Microbiology*, 2(3):241–249, 2004. ISSN 1740-1526. doi: 10.1038/nrmicro844.

[139] Ola Johnsborg, Vegard Eldholm, and Leiv Sigve Håvarstein. Natural genetic transformation: prevalence, mechanisms and function. *Research in Microbiology*, 158 (10):767–778, 2007. ISSN 09232508. doi: 10.1016/j.resmic.2007.09.004.

[140] L S Håvarstein, G Coomaraswamy, and D A Morrison. An unmodified heptadecapeptide pheromone induces competence for genetic transformation in Streptococcus pneumoniae. *Proceedings of the National Academy of Sciences of the United States of America*, 92(24): 11140–11144, 1995. ISSN 0027-8424. doi: 10.1073/pnas.92.24.11140. URL http://www.pubmedcentral.nih.gov/articlerender.fcgi?artid=40587{%}7B{&}{%}7Dtool=pmcentrez{%}7B{&}{%}7Drendertype=abstract.

[141] Adrian M Whatmore, Victoria A Barcus, and Christopher G Dowson. Genetic diversity of the streptococcal competence (com) gene locus. *Journal of Bacteriology*, 181(10):3144–3154, 1999. ISSN 00219193.

[142] Adilia Dagkessamanskaia, Miriam Moscoso, Vincent Hénard, Sébastien Guiral, Karin Overweg, Mark Reuter, Bernard Martin, Jerry Wells, and Jean-pierre Claverys. Interconnection of competence, stress and CiaR regulons in Streptococcus pneumoniae : competence triggers stationary phase autolysis of ciaR mutant cells. *Molecular Microbiology*, 51(4):1071–1086, 2004. doi: 10.1046/j.1365-2958.2003. 03892.

[143] Hilde Steinmoen, Eivind Knutsen, and Leiv Sigve Håvarstein. Induction of natural competence in Streptococcus pneumoniae triggers lysis and DNA release from a subfraction of the cell population. *Proceedings of the National Academy of Sciences of the United States of America*, 99(11):7681–7686, 2002. ISSN 00278424. doi: 10.1073/pnas.112464599.

[144] Leiv Sigve Håvarstein, Bernard Martin, Ola Johnsborg, Chantal Granadel, and Jean Pierre Claverys. New insights into the pneumococcal fratricide: Relationship to clumping and identification of a novel immunity factor. *Molecular Microbiology*, 59(4):1297–1307, 2006. ISSN 0950382X. doi: 10.1111/j.1365-2958.2005.05021.x.

[145] Jean Pierre Claverys, Bernard Martin, and Leiv Sigve Håvarstein. Competence-induced fratricide in streptococci. *Molecular Microbiology*, 64(6):1423–1433, 2007. ISSN 0950382X. doi: 10.1111/j.1365-2958.2007.05757.x.

[146] Jean-Pierre Claverys and Leiv S Håvarstein. Cannibalism and fratricide: mechanisms and raisons d'{ê}tre. *Nature reviews. Microbiology*, 5(3):219–229, 2007. ISSN 1740-1526. doi: 10.1038/nrmicro1613.

[147] Miriam Moscoso, Ernesto García, and Rubens López. Biofilm formation by Streptococcus pneumoniae: Role of choline, extracellular DNA, and capsular polysaccharide in microbial accretion. *Journal of Bacteriology*, 188(22):7785–7795, 2006. ISSN 00219193. doi: 10.1128/JB.00673-06.

[148] Hua Wei and Leiv Sigve Håvarstein. Fratricide Is Essential for Efficient Gene Transfer between Pneumococci in Biofilms. *Applied and Environmental Microbiology*, 78(16):5897–5905, 2012. ISSN 00992240. doi: 10.1128/AEM.01343-12.

[149] Laura R Marks, Ryan M Reddinger, and P Anders. High Levels of Genetic Recombination during Nasopharyngeal Carriage and Biofilm Formation in Streptococcus pneumoniae. *mBio*, 3(5):e00200–12, 2012. ISSN 2150-7511. doi: 10.1128/mBio.00200-12.Editor.

[150] N Luisa Hiller, Azad Ahmed, Evan Powell, Darren P Martin, Rory Eutsey, Josh Earl, Benjamin Janto, Robert J Boissy, Justin Hogg, Karen Barbadora, Rangarajan Sampath, Shaun Lonergan, J Christopher Post, Fen Z Hu, and Garth D Ehrlich. Generation of Genic Diversity among Streptococcus pneumoniae Strains via Horizontal Gene Transfer during a Chronic Polyclonal Pediatric Infection. *PLoS pathogens*, 6(9):e1001108, 2010. ISSN 1553-7374. doi: 10.1371/journal.ppat. 1001108. URL http://www.pubmedcentral.nih.gov/articlerender.fcgi?artid=2940740{&}tool=pmcentrez{&}rendertype=abstract.

[151] Rafal Mostowy, Nicholas J Croucher, William P Hanage, Simon R Harris, Stephen Bentley, and Christophe Fraser. Heterogeneity in the frequency and characteristics of homologous recombination in pneumococcal evolution. *PLoS genetics*, 10(5):e1004300, 2014. ISSN 1553-7404. doi: 10.1371/journal. pgen.1004300. URL http://journals.plos.org/plosgenetics/article?id=10.1371/journal.pgen.1004300.

[152] Nicholas J Croucher, Simon R Harris, Lars Barquist, Julian Parkhill, and Stephen D Bentley. A High-Resolution View of Genome-Wide Pneumococcal Transformation. *PLoS Pathogens*, 8(6):e1002745, 2012. ISSN 1553-7374. doi:

10.1371/journal.ppat.1002745. URL http://dx.plos.org/10.1371/journal.ppat.1002745.

[153] Laura R Marks, Lauren Mashburn-Warren, Michael J Federle, and Anders P Hakansson. Streptococcus pyogenes biofilm growth in vitro and in vivo and its role in colonization, virulence, and genetic exchange. *The Journal of infectious diseases*, 210(1):25–34, 2014. ISSN 1537-6613. doi: 10.1093/infdis/jiu058. URL http://www.pubmedcentral.nih.gov/articlerender.fcgi?artid=4162002{%}7B{&}{%}7Dtool=pmcentrez{%}7B{&}{%}7Drendertype=abstract.

[154] Morten Kjos, Rieza Aprianto, Vitor E Fernandes, Peter W Andrew, Jos A G van Strijp, Reindert Nijland, and Jan-Willem Veening. Bright Fluorescent Streptococcus pneumoniae for Live-Cell Imaging of Host-Pathogen Interactions. *Journal of Bacteriology*, 197(5):807–818, 2015. ISSN 1098-5530 (Electronic). doi: 10.1128/JB.02221-14.

[155] Katherine L O'Brien, Lara J Wolfson, James P Watt, Emily Henkle, Maria Deloria-Knoll, Natalie McCall, Ellen Lee, Kim Mulholland, Orin S Levine, and Thomas Cherian. Burden of disease caused by Streptococcus pneumoniae in children younger than 5 years: global estimates. *The Lancet*, 374(9693):893–902, 2009. ISSN 01406736. doi: 10.1016/S0140-6736(09)61204-6. URL http://dx.doi.org/10.1016/S0140-6736(09)61204-6.

[156] Claire Chewapreecha, Simon R Harris, Nicholas J Croucher, Claudia Turner, Pekka Marttinen, Lu Cheng, Alberto Pessia, David M Aanensen, Alison E Mather, Andrew J Page, Susannah J Salter, David Harris, Francois Nosten, David Goldblatt, Jukka Corander, Julian Parkhill, Paul Turner, and Stephen D Bentley. Dense genomic sampling identifies highways of pneumococcal recombination. *Nature Genetics*, 46(3):305–309, 2014. ISSN 1061-4036. doi: 10.1038/ng.2895. URL http://www.nature.com/doifinder/10.1038/ng.2895.

[157] Angela B Brueggemann, Rekha Pai, Derrick W Crook, and Bernard Beall. Vaccine escape recombinants emerge after pneumococcal vaccination in the United States. *PLoS Pathogens*, 3(11):1628–1636, 2007. ISSN 15537366. doi: 10.1371/journal.ppat.0030168.

[158] Tanya Golubchik, Angela B Brueggemann, Teresa Street, Robert E Gertz, Chris C A Spencer, Thien Ho, Eleni Giannoulatou, Ruth Link-Gelles, Rosalind M Harding, Bernard Beall, Tim E A Peto, Matthew R Moore, Peter Donnelly, Derrick W Crook, and Rory Bowden. Pneumococcal genome sequencing tracks a vaccine escape variant formed through a multi-fragment recombination event. *Nature Genetics*, 44(3):352–355, 2012. ISSN 1061-4036. doi: 10.1038/ng.1072. URL http://www.nature.com/doifinder/10.1038/ng.1072.

[159] Daniel Weinbergera M, Richard Malley, and Marc Lipsitch. Serotype replacement in disease following pneumococcal vaccination: A discussion of the evidence. *Lancet*, 378(9807):1962–1973, 2012. doi: 10.1016/S0140-6736(10)62225-8. Serotype.

[160] Linas Mazutis, John Gilbert, W Lloyd Ung, David A Weitz, Andrew D Griffiths, and John A Heyman. Single-cell analysis and sorting using droplet-based microfluidics. *Nature Protocols*, 8(5):870–891, apr 2013. ISSN 1754-2189. doi: 10.1038/nprot.2013.046. URL http://www.nature.com/doifinder/10.1038/nprot.2013.046.

[161] Haakan N. Joensson and Helene Andersson Svahn. Droplet microfluidics-A tool for single-cell analysis. *Angewandte Chemie - International Edition*, 51(49):12176–12192, 2012. ISSN 14337851. doi: 10.1002/anie.201200460.

[162] Na Wen, Zhan Zhao, Beiyuan Fan, Deyong Chen, Dong Men, Junbo Wang, and Jian Chen. Development of droplet microfluidics enabling high-throughput single-cell analysis. *Molecules*, 21(7):1–13, 2016. ISSN 14203049. doi: 10.3390/molecules21070881.

[163] Weihua Guan, Liben Chen, Tushar D. Rane, and Tza-Huei Wang. Droplet Digital Enzyme-Linked Oligonucleotide Hybridization Assay for Absolute RNA Quantification. *Scientific Reports*, 5(April):13795, 2015. ISSN 2045-2322. doi: 10.1038/srep13795. URL http://www.nature.com/doifinder/10.1038/srep13795.

[164] X. Liu, R. E. Painter, K. Enesa, D. Holmes, G. Whyte, C. G. Garlisi, F. J. Monsma, M. Rehak, F. F. Craig, and C. A. Smith. High-throughput screening of antibiotic-resistant bacteria in picodroplets. *Lab Chip*, 16:1636–1643, 2016. ISSN 1473-0197. doi: 10.1039/C6LC00180G. URL http://xlink.rsc.org/?DOI=C6LC00180G.

[165] Stanislav S. Terekhov, Ivan V. Smirnov, Anastasiya V. Stepanova, Tatyana V. Bobik, Yuliana A. Mokrushina, Natalia A. Ponomarenko, Alexey A. Belogurov, Maria P. Rubtsova, Olga V. Kartseva, Marina O. Gomzikova, Alexey A. Moskovtsev, Anton S. Bukatin, Michael V. Dubina, Elena S. Kostryukova, Vladislav V. Babenko, Maria T. Vakhitova, Alexander I. Manolov, Maja V. Malakhova, Maria A. Kornienko, Alexander V. Tyakht, Anna A. Vanyushkina, Elena N. Ilina, Patrick Masson, Alexander G. Gabibov, and Sidney Altman. Microfluidic droplet platform for ultrahigh-throughput single-cell screening of biodiversity. *Proceedings of the National Academy of Sciences*, page 201621226, 2017. ISSN 0027-8424. doi: 10.1073/pnas.1621226114. URL http://www.pnas.org/lookup/doi/10.1073/pnas.1621226114.

[166] Libing Dong, Dong-Wei Chen, Shuang-Jiang Liu, and Wenbin Du. Automated Chemotactic Sorting and Single-cell Cultivation of Microbes using Droplet Microfluidics. *Scientific Reports*, 6(April):24192, 2016. ISSN 2045-2322. doi: 10.1038/srep24192. URL http://www.nature.com/articles/srep24192.

[167] David J Collins, Adrian Neild, Andrew DeMello, Ai-Qun Liu, and Ye Ai. The Poisson distribution and beyond: methods for microfluidic droplet production and single cell encapsulation. *Lab Chip*, 2015. ISSN 1473-0197. doi: 10.1039/C5LC00614G. URL http://xlink.rsc.org/?DOI=C5LC00614G.

[168] Jon F Edd, Dino Di Carlo, Katherine J Humphry, Sarah Köster, Daniel Irimia, David a Weitz, and Mehmet Toner. Controlled encapsulation of single-cells into monodisperse picolitre drops. *Lab on a chip*, 8(8):1262–1264, 2008. ISSN 1473-0197. doi: 10.1039/b805456h.

[169] N P Macdonald, F Zhu, C J Hall, J Reboud, P S Crosier, E E Patton, D Wlodkowic, and J M Cooper. Assessment of biocompatibility of 3D printed photopolymers using zebrafish embryo toxicity assays. *Lab on a Chip*, 16(2):291–297, 2016. ISSN 1473-0197. doi: 10.1039/C5LC01374G. URL www.rsc.org/loc{%}5Cnhttp://xlink.rsc.org/?DOI=C5LC01374Ghttp://xlink.rsc.org/?DOI=C5LC01374G.

[170] Megan L Rexius-Hall, Gerardo Mauleon, Asrar B Malik, Jalees Rehman, and David T Eddington. Microfluidic platform generates oxygen landscapes for localized hypoxic activation. *Lab on a chip*, 14(24):4688–95, dec 2014. ISSN 1473-0189. doi: 10.1039/c4lc01168f. URL http://www.ncbi.nlm.nih.gov/pubmed/

25315003.

[171] Ji-Won Lee, Seong-Hui Bae, Joo-Won Jeong, Se-Hee Kim, and Kyu-Won Kim. Hypoxia-inducible factor (HIF-1)alpha: its protein stability and biological functions. *Experimental & molecular medicine*, 36(1):1–12, feb 2004. ISSN 1226-3613. doi: 10.1038/emm.2004.1. URL http://www.ncbi.nlm.nih.gov/pubmed/15031665.

[172] Carla Rohrer Bley, Katrin Orlowski, Polina Furmanova, Paul M J McSheehy, and Martin Pruschy. Regulation of VEGF-expression by patupilone and ionizing radiation in lung adenocarcinoma cells. *Lung cancer (Amsterdam, Netherlands)*, 73 (3):294–301, sep 2011. ISSN 1872-8332. doi: 10.1016/j.lungcan.2011.01.010. URL http://www.sciencedirect.com/science/article/pii/S0169500211000468.

[173] Thomas J. Hinton, Andrew Hudson, Kira Pusch, Andrew Lee, and Adam W. Feinberg. 3D Printing PDMS Elastomer in a Hydrophilic Support Bath via Freeform Reversible Embedding. *ACS Biomaterials Science and Engineering*, 2(10):1781–1786, 2016. ISSN 23739878. doi: 10.1021/acsbiomaterials.6b00170.

[174] Yun-Ho Jang, Matthew J Hancock, Sang Bok Kim, Šeila Selimović, Woo Young Sim, Hojae Bae, and Ali Khademhosseini. An integrated microfluidic device for two-dimensional combinatorial dilution. *Lab on a chip*, 11(19):3277–86, oct 2011. ISSN 1473-0189. doi: 10.1039/c1lc20449a. URL http://www.ncbi.nlm.nih.gov/pubmed/21837312http://www.pubmedcentral.nih.gov/articlerender.fcgi?artid=PMC3357545.

[175] Eddington Lab. 3D-Printed Oxygen Control Insert, 2017. URL https://github.com/Biological-Microsystems-Laboratory/3d-printed-oxygen-control-insert.

[176] Eddington Lab. 3D Printable Micropipette, 2017. URL https://github.com/Biological-Microsystems-Laboratory/micropipette.

[177] Richard Stallman. GNU General Public License v2.0, 1991. URL https://www.gnu.org/licenses/old-licenses/gpl-2.0.en.html.

[178] Shoji Takeuchi, Piotr Garstecki, Douglas B. Weibel, and George M. Whitesides. An axisymmetric flow-focusing microfluidic device. *Advanced Materials*, 17(8):1067–1072, 2005. ISSN 09359648. doi: 10.1002/adma.200401738.

[179] Jian Zhou and Ian Papautsky. Fundamentals of inertial focusing in microchannels. *Lab on a chip*, 13(6):1121–1132, 2013. ISSN 1473-0189. doi: 10.1039/c2lc41248a. URL http://www.ncbi.nlm.nih.gov/pubmed/23353899.

[180] Todd P. Lagus and Jon F. Edd. High-throughput co-encapsulation of self-ordered cell trains: cell pair interactions in microdroplets. *RSC Advances*, 3:20512, 2013. ISSN 2046-2069. doi: 10.1039/c3ra43624a. URL http://xlink.rsc.org/?DOI=c3ra43624a.

[181] Martin Brennan, Fahad Bokhari, and David Eddington. Open Design 3D-Printable Adjustable Micropipette that meets ISO Standard for Accuracy. *bioRxiv*, 2017.

VITA

NAME:	Martin D. Brennan
EDUCATION:	B.S., Bioengineering, University of Illinois at Chicago, 2006
	PhD Bioengineering, University of Illinois At Chicago, 2017
AWARDS:	Tony B. Academic Travel Award to attend SLAS2017 Feb. 2017
	Provost Deiss Award for Graduate Research, 2016
	Provost Deiss Award for Graduate Research, 2014
PUBLICATIONS:	M. Brennan, M. L. Rexius-Hall, and D. T. Eddington. A 3D-Printed Oxygen Control Insert for a 24-Well Plate. Plos One, 10(9):e0137631, 2015
	M. Brennan, M. L. Rexius-Hall, L. J. Elgass, and D. T. Eddington. Oxygen control with microfluidics. Lab on a chip, 14(22):4305–18, 2014
	J. F. Lo, M. Brennan, Z. Merchant, L. Chen, S. Guo, D. T. Eddington, and L. a. DiPietro. Microfluidic wound bandage: localized oxygen modulation of collagen maturation. Wound repair and regeneration : official publication of the Wound Healing Society [and] the European Tissue Repair Society, 21(2):226–34, 2013
ABSTRACTS:	M. Brennan, F. Bokhari, and D. Eddington. Open Design 3D-Printable Adjustable Micropipette that meets ISO Standard for Accuracy. bioRxiv, 2017
	Brennan, M. et al. (2017, March). Femtoliter Droplet Confinement of Pneumococcus Pairs for Single Event Transformation Assay. Poster at Center for Advanced Design and Manufacturing of Integrated Microfluidics (CADMIM), University of California Irvine, Irvine, CA
	Brennan, M. et al. (2017, March). 3D-Printed Oxygen Control Insert for a 24-Well Plate. Poster at Center for Advanced Design and Manufacturing of Integrated Microfluidics (CADMIM), University of California Irvine, Irvine, California.

Brennan, M. et al. (2017, February). Femtoliter Droplet Confinement of Pneumococcus Pairs for Single Event Transformation Assay. Poster at Annual Society for Laboratory Automation and Screening (SLAS) Conference and Exhibition, Walter E. Washington Convention Center, Washington, DC.

Brennan, M. et al. (2016, December). Femtoliter Droplet Confinement of Pneumococcus Pairs for Single Event Transformation Assay. Poster at Conference on Micro and Nanotechnology in Medicine (MNM), Hilton Waikoloa Village, Waikoloa, HI.

Brennan, M. et al. (2016, October). Femtoliter Droplet Confinement of Pneumococcus Pairs for Single Event Transformation Assay. Poster at Biomedical Engineering Society (BMES) Annual Meeting, Minneapolis Convention Center, Minneapolis, MN.

Brennan, M. et al. (2015, October). 3D-Printed Oxygen Control Insert for a 24-Well Plate. Poster at Biomedical Engineering Society (BMES) Annual Meeting, Tampa Convention Center, Tampa, Florida.

Brennan, M. et al. (2014, October). 3D-Printed Microfluidic Devices for Oxygen Control in Cell Culture. Poster at Micro Total Analysis Systems (MicroTAS) Conference on Miniaturized Systems for Chemistry and Life Sciences, Henry B. Gonzalez Convention Center, San Antonio, TX.